Investigation of Electrocatalytic Oxidation Reactions

Insights From Electrochemical Mass Spectrometry

Yilmaz, Tugce

Publication date:
2023

Document Version
Publisher's PDF, also known as Version of record

Investigation of Electrocatalytic Oxidation Reactions: Insights From Electrochemical Mass Spectrometry

Tugce Yilmaz

Supervisor: Prof. Brian Seger
Co-supervisor: Prof. Ib Chorkendorff

Department of Physics
Section of Surface Physics and Catalysis
Technical University of Denmark

PhD Thesis

August 2023

Abstract

In recent years, we are witnessing the escalating impacts of climate change, including increasingly frequent heatwaves, flooding, and wildfires. These events emphasize the necessity of urgent actions to address global warming. One significant way of addressing this challenge is replacing fossil fuels with renewable energy sources. Notably, the chemical industry ranks among the leading contributors to CO_2 emissions. Therefore, electrification of the chemical industry emerges as a strategy to tackle the climate change.

However, to compete with the current industrial methods, electrochemical methods must become more economically feasible. This goal requires the design of highly active, selective, and stable catalysts for the electrochemical synthesis of substances. To design catalysts rationally, a fundamental understanding of the reaction mechanisms is a necessity. Therefore, gaining real-time insights into the reactions is critically valuable. In this regard, electrochemical mass spectrometry (EC-MS) is used for the investigation of two important reactions for the chemical industry in this study: electrochemical propylene epoxidation and chlorine evolution reaction.

In this study, EC-MS is applied for the detection of propylene oxide, and electrochemical propylene epoxidation is measured in real-time. The selectivity and activity trends are investigated on PtO_x and PdO_x catalysts to obtain insights into the mechanism of electrochemical propylene epoxidation. The results reveal that the selectivity for epoxidation peaks at 1.3 V vs. RHE on PdO_x, whereas it steadily increases on PtO_x up to 1.6 V vs. RHE. However, further anodic potentials could not be explored due to conductivity issues arising from bubble formation in the stagnant thin-layer cell in the EC-MS system. Furthermore, mass spectrometry-derived Tafel plots indicate a consistent rise in epoxidation activity without a change in slope on PtO_x as potentials become

more anodic. Conversely, a notable change in slope at 1.3 V vs. RHE on PdO_x suggests a shift in the reaction mechanism at this potential. This phenomenon aligns with a previously published theoretical study [1], which proposes a Langmuir-Hinselwood mechanism for PtO_2 and a transition from Langmuir-Hinselwood to Mars-Van Krevelen mechanism with the formation of oxygen vacancies on PdO. Moreover, EC-MS reveals the formation of CO_2 through surface oxide reduction, serving as an indicator of surface oxidation under the reaction conditions.

Furthermore, chlorine evolution reaction (CER) is explored with EC-MS during my three months of external stay in Spectro Inlets, ApS. EC-MS provided a great sensitivity for Cl_2, resulting in the lowest detection potentials for CER to the best of our knowledge. This finding raised questions regarding equilibrium potential definitions in the literature. Consequently, this thesis conducts a comprehensive review of equilibrium potential definitions in the literature. A method for the dynamic equilibrium potential determination by utilizing EC-MS is proposed and its limitations are described.

Moreover, CER activity evaluations are conducted for various catalysts including RuO_2, IrO_2, and Pt-based catalysts being Pt stub, Pt film on Ti substrate, and 2 nm TiO_2 on Pt film on glassy carbon substrate. The results revealed that the activity of Pt-based catalysts surpasses that of RuO_2 and IrO_2. It is suggested that the oxidation of Pt is retarded in the presence of Cl^- which leads to a reaction mechanism involving direct Pt-Cl intermediate with faster kinetics rather than Pt-OCl. This hypothesis is supported with the CO stripping experiments, conducted both with and without Cl^-. These experiments revealed a $\approx$600 mV shift in the CO oxidation potential towards more anodic values in the presence of Cl^-. This shift signifies the inhibition of oxygen species adsorption onto the catalyst surface due to competitive Cl^- adsorption.

Resume

De seneste år har vi været vidne til stadig større konsekvenser af klimaforandringerne, herunder hyppigere hedebølger, oversvømmelser og skovbrande. Disse begivenheder viser nødvendigheden af hurtig handling for at minimere konsekvenserne af den globale opvarmning. Det anses som essentielt at erstatte fossile brændstoffer med vedvarende energikilder, for at adressere denne udfordring. Den kemiske industri er blandt de største bidragsydere til CO_2-udledning. Derfor er elektrificering af den kemiske industri en strategi til at minimere konsekvenserne af klimaforandringerne.

Men for at konkurrere med de nuværende industrielle metoder, skal elektrokemiske metoder i højere grad blive økonomisk attraktive. Dette kræver design af aktive, selektive og stabile katalysatorer til elektrokemisk fremstilling af kemikalier. Men for at designe katalysatorer hensigtsmæssigt, er det nødvendigt med en grundlæggende forståelse af de involverede reaktionsmekanismerne. Derfor er det afgørende at få realtidsinformation om reaktionerne. I dette studie bruges der således elektrokemisk massespektrometri (EC-MS) til undersøgelse af to vigtige reaktioner for den kemiske industri: elektrokemisk propylenepoxidation og klorudviklingsreaktion.

I dette studie anvendes EC-MS til påvisning af propylenoxid, og måles elektrokemisk propylenepoxidation i realtid. Selektivitets- og aktivitetstendenserne undersøges på PtO_x- og PdO_x katalysatorer for at få indsigt i mekanismen for elektrokemisk propylenepoxidation. Resultaterne viser, at selektiviteten for epoxidation topper ved 1.3 V vs. RHE på PdO_x, hvorimod den er stigende på PtO_x op til 1.6 V vs. RHE. Yderligere anodiske potentialer kunne ikke undersøges, da der her var begrænset ledningsevnen grundet bobledannelse i cellens begrænsede volumen, samt den statiske elektrolyt i EC-MS-systemet. Endvidere indikerer Tafel-plots udledt fra massespektrometri en jævn stigning i epoxidationsaktiviteten uden en ændring i hældning på PtO_x, efterhånden som

potentialerne bliver mere anodiske. Omvendt tyder en markant ændring i hældning ved 1.3 V vs. RHE på PdO_x et skift i reaktionsmekanismen ved dette potentiale. Fænomenet stemmer overens med en tidligere publiceret teoretisk undersøgelse[1], som foreslår en Langmuir-Hinselwood-mekanisme for PtO_2 og en overgang fra Langmuir-Hinselwood til Mars-Van Krevelen-mekanisme med dannelsen af en oxygen vacancy på PdO. Desuden afslører EC-MS dannelsen af CO_2 gennem overfladeoxidreduktion, hvilket er en indikator for overfladeoxidation under reaktionsbetingelserne.

Endvidere udforskes klorudviklingsreaktion med EC-MS under mine tre måneders eksterne ophold i Spectro Inlets, ApS. EC-MS gav en betydelig målefølsomhed af Cl_2, hvilket resulterede i de lavest målte detektionspotentialer for klorudviklingsreaktionen efter vores bedste viden. Dette rejste spørgsmål vedrørende definitionen af ligevægtspotentialet i litteraturen. Dette studie foretager derfor en omfattende gennemgang af definitionen af ligevægtspotentialet i litteraturen. En metode til dynamisk ligevægtspotentialebestemmelse ved at anvende EC-MS foreslås, og dens begrænsninger beskrives.

Desuden udføres evalueringer af klorudviklingsaktivitet for forskellige katalysatorer, herunder RuO_2, IrO_2 og Pt-baserede katalysatorer. For Pt-baserede katalysatorer er der tale om en Pt-stub, Pt-film på Ti-substrat og 2 nm TiO_2 på Pt-film på glossy kulstofsubstrat. Resultaterne viste, at aktiviteten af Pt-baserede katalysatorer overgår aktiviteten af RuO_2 og IrO_2. Det foreslås, at oxidationen af Pt hæmmes i nærværet af Cl^-, hvilket fører til en reaktionsmekanisme, der involverer et direkte Pt-Cl-mellemprodukt med hurtigere kinetik, snarere end Pt-OCl. Denne hypotese understøttes af CO-stripping-eksperimenterne, udført både med og uden Cl^-. Disse eksperimenter viste et $\approx$600 mV skift i CO-oxidationspotentialet mod mere anodiske værdier, under tilstedeværelse af Cl^-. Dette skift betyder at oxygenarters adsorption på katalysatoroverfladen hæmmes på grund af den konkurrerende Cl-adsorption.

Preface

The work for this thesis was carried out at the Technical University of Denmark, Department of Physics, Section of Surface Physics and Catalysis (SurfCat) in the period between September 2020 and August 2023, including an external research stay at Spectro Inlets, ApS from February 2023 to April 2023.

My experimental work was carried out in close collaboration with other students. Throughout this thesis, I use the pronoun "I" to highlight the parts of the work carried out by myself, while "we" is used where no clear distinction between my work and ideas, and those of my colleagues can be made. The contributors to the work in the different parts of this thesis are stated in the respective chapters.

Tugce Yilmaz
August 2023

Acknowledgements

I acknowledge the Carlsberg Foundation for funding this research within the EHALIDE project. There are several people contributed invaluably to completion of this PhD thesis to whom I owe my deepest gratitude.

I begin by expressing my profound appreciation to my main supervisor, Prof. Brian Seger. His invaluable guidance, engaging discussions, and unwavering support have played a crucial role in shaping this thesis and enriching my academic journey. I am especially appreciative of his support, which extends beyond academic matters, allowing me the freedom to explore and his efforts in advancing my career beyond the scope of this PhD. I also wish to express my gratitude to my co-supervisor, Prof. Ib Chorkendorff, for his profound insights and continuous guidance, which have immensely enriched this research.

I would like to thank to my collaborators in the chlorine evolution project. Many thanks to Clara Bruun Jensen, Francesco Longhin and Sahil Garg for helping with the catalyst preparations, and to Yu Qiao for helping me extensively with the catalyst characterization and data analysis. Moreover, my sincere gratitude to everyone in Spectro Inlets for being incredibly welcoming and helpful to me during my external stay. Especially, Johannes Novak Hansen for hosting me, his insights and discussions. Also, I would like to thank to Kim Degn Jensen and Anna Winiwarter for the great discussions and suggestions. I must mention Anna's exceptional support, also in propylene oxidation, even though she left SurfCat before my arrival. Her approachability for questions and her guiding thesis were invaluable. Finally, I would like to thank to our theory collaborators Christina Susan Abraham and Prof. Jens K. Nørskov for their insights into electrochemical propylene epoxidation, as well as our enriching discussions and guidance.

I am grateful to the floor managers, Brian Peter Knudsen and Jakob Ejler Sørensen, for their assistance in keeping our labs operational and being supportive at any time needed. My special thanks to Jacqueline McAnulty, whose dedication goes beyond ensuring lab order and safety. Her constant positivity and unwavering support have been a bright presence throughout this demanding journey.

I extend my heartfelt gratitude to all my friends in SurfCat; it has been a privilege to embark on this PhD with such a group of kind-hearted and intelligent individuals. I would like to thank to members of the CO_2 group especially. Thank you to Wanyu, with her infectious happiness, she has lifted our entire group's spirits. Asger, for his friendship and assistance. I'm especially grateful for his help in mastering Python. Sahil and Qiucheng for not only being amazing friends but also hosting unforgettable dinner parties. Yu's support, especially during the thesis writing process, and our insightful discussions about EC-MS and XPS have been invaluable. Bjørt's positive energy and calmness, has been truly uplifting. I particularly cherish our memorable coffee shop writing sessions and her help in fixing my Python scripts. Francesco's wonderful personality made it almost impossible to be upset around him. He brought a lot of laughter to my days which has been really helpful during my PhD. Carlos has been a source of support, he's always been there when I've needed him. I am deeply thankful for his lifelong friendship. Clara, holds a special place in my heart with her unwavering support. PhD became much more enjoyable since we became office mates. Other than CO_2 group, I want to thank Katja for her amazing friendship, engaging interest in my research, our enjoyable times together. I appreciate Chao for our conversations, his support, and for our discussions about oxidation reactions, which he was the only person with whom I could delve into such discussions. Lastly, my heartfelt thanks to Sarah for the much-needed coffee breaks, constant support, and for providing strength, especially during the last months.

Lastly, I am immensely thankful to my friends, Beyza, Inci, and Damla, whose support over the past 14 years has been a constant source of strength and encouragement. I am also grateful to my grandmother and my aunt for their sacrifices for my education. And last, but certainly not least, I must express my deepest appreciation to my ever-supportive and loving parents whose encouragement has guided me throughout my entire life.

List of publications

Paper I

Direct Electrocatalytic Propylene Epoxidation on PdO_x **and** PtO_x

Tugce Yilmaz*, Christina Susan Abraham*, Hao Li, Megha Anand, Ib Chorkendorff, Jens K. Nørskov, and Brian Seger.

in preparation

* these authors contributed equally

Table of contents

Nomenclature

Roman Symbols

a	Chemical activity
D	Diffusion constant
E^0	Standard equilibrium potential
E_b	Binding energy
E	Equilibrium potential
E_k	Kinetic energy
f_i	Gas correction factor of gas i for ion gauge pressure sensor
FE	Faradaic efficiency
F	Faraday's constant = 96485 $Cmol^{-1}$
ΔG	Gibbs free energy
h	Planck's constant = $6.626 \cdot 10^{-34}$ Js
K_n^{pc} :	Henry's law constant for volatility
h_n	Mass transfer coefficient
i_0	Exchange current
i	Current

J	Current Density
k_B	Boltzmann's constant = $1.38 \times 10^{-23} J \cdot K^{-1}$
L	Diffusion length of the species from the electrode surface to membrane chip
$\bar{\dot{n}}$	Averaged Cl_2 molar flux to MS
m/z	Mass-to-charge ratio
$\dot{N}_0^v$	Total molecular flux to MS
n	Number of moles
P	Pressure
Q	Charge
R	Universal gas constant = $8.314\ J mol^{-1} K^{-1}$
$\bar{S_{MS}}$	Averaged MS signal
S	Turbomolecular pump speed
T	Temperature
t	Time
z	Number of electrons transferred

Greek Symbols

α	Transfer coefficient
ν	Exciting Radiation's Frequency
η	Overpotential
ϕ	Workfunction
σ_n	Standard deviation of the baseline signal of a species in MS

τ_n Characteristic time constant for EC-MS

θ Incident ion angle in ISS

Acronyms / Abbreviations

ALD Atomic Layer Deposition

BSE Back-Scattered Electrons

CA Chronoamperometry

CE Counter Electrode

CER Chlorine Evolution Reaction

CP Chronopotentiometry

CV Cyclic Voltammetry

DEMS Differential Electrochemical Mass Spectrometry

DFT Density Functional Theory

DSA Dimensionally Stable Anode

EC-MS Electrochemical Mass Spectrometry

ECSA Electrochemically Active Surface Area

EDX Energy Dispersive X-ray Detector

EI Electron Ionization

EIS Electrochemical Impedance Spectroscopy

ETD Everhart-Thornley Detector

GC Glassy Carbon

HPLC High Performance Liquid Chromatography

ICP-MS Inductively Coupled Plasma Mass Spectrometry

ISS Ion Scattering Spectroscopy

LOD Limit of Detection

MSCV Mass Spectrometry Cyclic Voltammetry

MS Mass Spectrometry

NMR Nuclear Magnetic Resonance

OER Oxygen Evolution Reaction

OLEMS On-line Electrochemical Mass Spectrometry

PINRR Potential Induced Non-Faradaic Redox Reaction

PO Propylene Oxide

QMS Quadrupole Mass Spectrometer

RE Reference Electrode

RHE Reversible Hydrogen Electrode

RRDE Rotating Ring-Disk Electrode

SECM Scanning Electrochemical Microscopy

SEM Scanning Electron Microscopy

SHE Standard Hydrogen Electrode

V-H Volmer-Heyrovsky

V-T Volmer-Tafel

WE Working Electrode

XAS X-ray Absorption Spectroscopy

XPS X-ray Photoelectron Spectroscopy

Chapter 1

Introduction

1.1 Electrification of the Chemical Industry

In 2015, to fight with the climate change, 195 countries signed the Paris Agreement in United Nations Climate Change Conference to limit the temperature rise to 2°C, but even pursue to limit it to 1.5°C. In the latest Conference of Parties meeting in 2022 (COP27), it is highlighted that greenhouse emissions should be reduced by 43% by 2030 to achieve this goal. However, with the current pledges from these countries by the end of the century the world is expected to be 2.5°C warmer [2].

CO_2 emissions from the industry have reached 28.9% of the total CO_2 emissions in 2022 [3]. In Figure1.1a, share of different industries to the CO_2 emissions shows that the biggest contributor is the chemical industry by 37% in 2019. Among various products it is shown that petrochemicals have significant global warming effect ranked third after iron and steel and cement (Figure 1.1b) [4].

Electrification of the chemical industry is proposed to reduce the greenhouse gas emissions by using renewable energy as a energy source. As a result of the increasing efforts to replace the fossil fuels with the renewable sources, share of renewable energy in total energy supply reached to 12.3% globally [5]. In Denmark, 41.8% of the total energy consumption is sourced from renewable energy in 2022 [6]. With the developments in the renewable energy contribution to the electricity, replacing the traditional methods for the production of chemicals with electrochemical methods is a

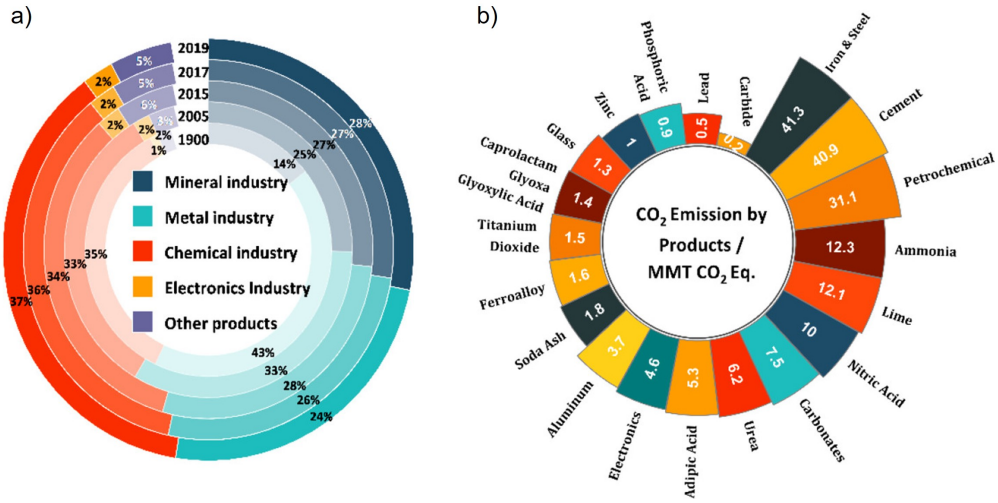

Figure 1.1 (a) CO_2 emission share of different industries. (b) Global warming effect of various products described with CO_2 equivalent. Reprinted from [4]. Copyright 2022 The Authors. Published by American Chemical Society. Licensed under CC-BY-NC-ND 4.0. Open Access

strategy for decarbonization.Electrochemical methods have other advantages over the thermal processes. Firstly, electrochemical approach enables decentralization of the processes due to the availability of small scale production stemmed from the modularity of electrochemical cells. Additionally, controlling potential is easier than controlling temperature and pressure therefore overall reaction control is higher. Furthermore, with electrochemical method excessive renewable energy can be stored as a chemical energy [4]. As it can be seen from Figure 1.2, the production rate of the renewable energy changes in a daily basis as it depends on the meteorological events such as wind and solar. Therefore, in the days where the produced electricity is higher than the consumption, it is important to store the energy for the days there is a supply deficit. The excessive energy can be stored by producing chemicals which is known as Power-to-X.

It is expected that decarbonization through electrochemical methods will play a significant role with the developments of renewable energy sources and fullfilling the climate targets Additionally, the advancements in the renewable energy methods accelerates electrification of the chemical industry, and vice versa.

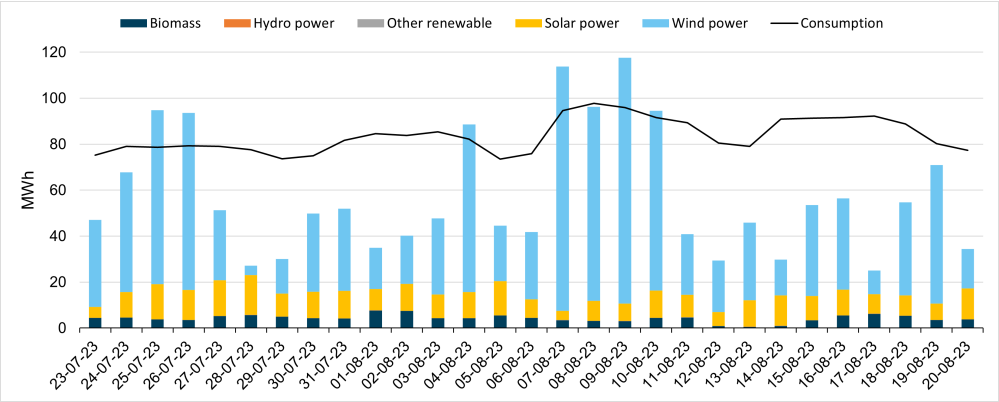

Figure 1.2 Daily renewable energy production and their shares, and the electricity consumption in Denmark between July 23 - August 20, 2023. Data is sourced from [7].

1.2 Electrocatalysis

The thermodynamic energy required for a reaction to happen is described as the difference in the Gibbs free energies of a reactant and a product. However, for reaction to proceed, the reactants need to reach to the transition state as a result of collision with the adjacent molecules which has higher energy than their initial state. The energy difference between the transition and initial state is called as the activation energy. A catalyst provides and alternative reaction route by creating intermediates with the reactants with more steps but with a lower activation energy, and decreases the overall energy requirement for the reaction. A catalyst does not involve to the reaction product. A catalytic reaction involves adsorption of the reactant to the catalyst and desorption of the product. This thesis is focused on heterogeneous catalysis in which the reactant and the catalyst are in different phases. Considering a reaction as following:

$$A + B \rightarrow AB \tag{1.1}$$

There are three main catalytic mechanisms in heterogeneous catalysis: (i) Langmuir-Hinselwood where reactant A and B adsorbs to the surface of the catalyst followed by the formation of AB as a result of their reaction on the surface. Finally, AB is desorbed from the surface. (ii) Eley-Rideal mechanism involves the adsorption of reactant A

to the catalyst surface and reacts with B directly without B adsorbing to the catalyst. Subsequently, the product AB is desorbed from the catalyst surface. (iii) Mars-Van Krevelen mechanism involves a reactant in the lattice of the catalyst. Reactant A adsorbs to the surface, reacts with the reactant B from the lattice of the catalyst and the reaction ends with the desorption of AB from the surface.

Paul Sabatier suggested that a good catalyst should bind the reactant strong enough to form the intermediate for the reaction to proceed, but weak enough for the desorption of the product. Therefore, optimal binding energy for a high catalytic activity is required and this phenomena is called as Sabatier's principle. As as a result, volcano curves obtained by plotting the catalytic activity versus the binding energy of the adsorbate showing the optimal binding energy (Figure 1.3) [8].

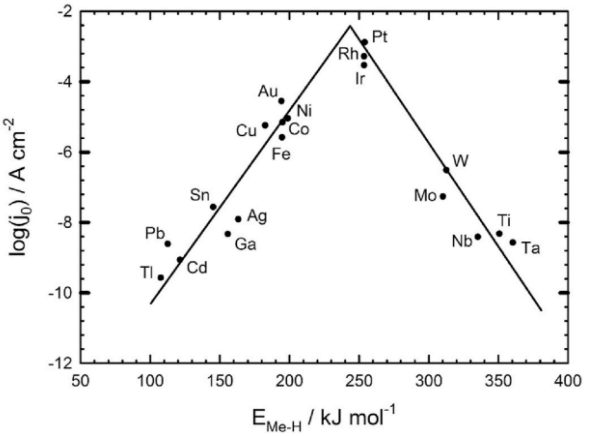

Figure 1.3 Volcano curve for hydrogen evolution reaction. Reprinted from [9] under the terms of the Creative Commons CC-BY license. Open Access

Electrocatalysis is a branch of catalysis where the difference in the electrical potential is used driving the reaction. The thermodynamic potential required to achieve the half-cell reaction is defined as the equilibrium potential and calculated with Nernst Equation derived from the Gibbs free energy. Assuming a reaction defined as following:

$$xO + ne^{-} \rightleftharpoons yR \tag{1.2}$$

where x, n, and y are stoichiometric coefficients.

The Gibbs free energy is:

$$\Delta G = \Delta G^0 + RTln\frac{aR^y}{aO^x} \tag{1.3}$$

where ΔG^0 is the Gibbs free energy under the standard conditions, R is the universal gas constant, T is the temperature, a is the activity of the species.

The relationship between the Gibbs free energy with the equilibrium potential of an electrochemical reaction (E) and standard equilibrium potential (E^0) is given in Equation 1.4 and 1.5, respectively. In these equations z stands for the number of electrons transferred and F stands for Faraday's constant.

$$\Delta G = -zFE \tag{1.4}$$

$$\Delta G^0 = -zFE^0 \tag{1.5}$$

With the combination of Equations 1.3, 1.4, and 1.5 Nernst equation is obtained defining the equilibrium potential of the electrochemical reaction:

$$E = E^0 + RTln\frac{aR^y}{aO^x} \tag{1.6}$$

While equilibrium potential describes the thermodynamic potential required for the reaction, actual potential required for the reaction to proceed is higher due to kinetic limitations. The difference between the actual potential to drive the reaction (E_{ac}) and the equilibrium potential is defined as overpotential (η), and it is a significant descriptor for the activity of a electrocatalyst.

$$\eta = E_{ac} - E \tag{1.7}$$

Additionally, the relationship between the current and the overpotential is described with Butler-Volmer equation:

$$i = i_0[e^{\frac{-\alpha\eta F}{RT}} - e^{\frac{(1-\alpha)\eta F}{RT}}] \tag{1.8}$$

where i is current and i_0 is exchange current which equals to the anodic and cathodic current at the equilibrium where the net current is zero.

Butler-Volmer equation is simplified to two different equations at the low overpotential regime and the high overpotential regime. At the low overpotentials where a linear relationship between the current and potential is observed the following equation becomes valid:

$$i = i_0 \frac{\eta F}{RT} \tag{1.9}$$

On the other hand, at the high overpotential regime where an exponential relationship between current and potential exists, Butler-Volmer equation simplifies to the Tafel equation described below [10]:

$$\eta = \frac{RT}{\alpha F} ln\, i_0 - \frac{RT}{\alpha F} ln\, i \quad \text{simplified to} \quad \eta = a + b\, log\, i \tag{1.10}$$

Evaluation of the Electrocatalyst Performance

The performance of a electrocatalyst is determined according to its selectivity, activity, and stability. The selectivity is derived from the Faraday's law:

$$n = \frac{Q}{zF} \tag{1.11}$$

where n is the number of moles, Q is the charge, z is the number of electrons required for the reaction. From Faraday's law, the selectivity is derived and called as Faradaic efficiency in Equation 1.12.

$$FE_i = \frac{n_i z F}{Q} \tag{1.12}$$

A descriptor for the activity of an electrocatalyst is the partial current density defined in Equation 1.13 where J_i is the partial current density for product i, J_{tot} is the total current density, ECSA is the electrochemically active surface area, t is the reaction time.

$$J_i = J_{tot}\, FE_i \quad or \quad J_i = \frac{n_i z F}{ECSA\, t} \tag{1.13}$$

During an electrochemical experiment, two half reactions take place. The half reaction of interest happens on the working electrode (WE), and the other reaction happens on the counter electrode. As the there are chemical changes on or near both of these electrodes to measure the absolute potential of working electrode, one needs to use have a reference point that stays constant throughout the experiment. For this purpose reference electrode consist of a stable redox couple and it is used to define a fixed potential as its composition remains constant during the experiment. Therefore, the absolute potential of the WE can be determined against the reference electrode. Standard hydrogen electrode (SHE) is described by defining the equilibrium potential of $2H^+ + 2e^- \rightleftharpoons H_2$ on Pt as zero under the standard conditions(1 atm H_2 and activity of H^+ being 1). As SHE varies at different pH electrolytes, reversible hydrogen electrode (RHE) is defined to compare reactions proceeding in electrolytes with different pH values. The relationship between SHE and RHE is given in Equation 1.14 [10].

$$E_{SHE} = E_{RHE} + 0.059pH \tag{1.14}$$

Due to the impracticality of using SHE as the electrolyte needs to have 1 atm H_2 and chemical activity of H^+ needs to be one, in the experiments alternative reference electrodes are used such as Hg/Hg_2SO_4, Ag/AgCl, Hg/HgO, etc. [11]

1.3 Outline of This Thesis

In this section, first I will provide the background story of this PhD project. Subsequently, I will provide a guide for each chapter to enhance the reading experience.

In this thesis, electrochemical propylene oxidation and chlorine evolution reactions are investigated with electrochemical mass spectrometry (EC-MS) offering real-time insights into these reactions. The selection of these reactions arises from the initial objective of my PhD, which was the halogenation of hydrocarbons. Preliminary experiments were conducted involving the chlorination of ethylene and propylene on Pd and Pt catalysts, revealing significant challenges. Notably, the Pd catalyst is fully dissolved under the reaction conditions, primarily due to heightened dissolution in the presence of chloride ions. Similarly, the Pt catalyst exhibits exceptionally high dissolution rates. Furthermore, the halogenation of alkenes yields a multitude of potential products, mak-

ing the product analysis profoundly difficult. This reaction can yield various alkene oxidation products, all of which are detailed in this thesis, in addition to numerous chlorinated compounds. Many of these organic compounds display instability, necessitating advanced techniques for accurate product analysis. I dedicated nearly a year to calibrate high-performance liquid chromatography, gas chromatography, and head-space gas chromatography. However, reproducible calibrations could not be achieved due to the instability of the reaction products. Consequently, conducting experiments in alkene halogenation proves to be an highly complex process. Moreover, the existing lack of knowledge in the literature about electrochemical propylene oxidation reaction enhances the challenge as it would be a side reaction of electrochemical halogenation reaction. Lastly, as propylene oxide is one of the most important derivatives of propylene, I found it valuable to work on understanding to mechanism towards electrochemical propylene oxidation to propylene oxide.

In conclusion, due to high complexity of electrochemical propylene halogenation reaction in terms of catalyst stability, product analysis, unclear reaction mechanisms for the side reactions I used an alternative approach. I have investigated electrochemical propylene oxidation and chlorine evolution reactions to simplify the system's complexity, facilitating a more comprehensive understanding of the underlying mechanisms. Although my original intent was to combine these reactions during my PhD, time constraints prevented its realization.

The content of each chapter in this thesis is briefly described below:

- **Chapter 1:** This chapter explains the motivation of this PhD study by addressing the importance of the electrification of chemical industry for the targets towards the tackling climate change. Additionally, electrocatalysis is briefly described and relevant fundamentals are given required to comprehend the work represented in this thesis.

- **Chapter 2:** Literature review on two electrocatalytic oxidation reactions: first propylene oxidation, then chlorine evolution reaction is given. This chapter includes the market value of the target products, industrial production methods, and recent advances in the field.

- **Chapter 3:** Experimental methods used in this thesis are explained including the instruments and their working principles.
- **Chapter 4:** Challenges for propylene oxide detection is addressed, followed by how EC-MS is utilized for *in-situ* propylene oxide detection.
- **Chapter 5:** The selectivity and activity trends for propylene oxidation to propylene oxide on PtO_x and PdO_x are given, and related to this the reaction mechanisms are discussed. Additionally, formation of CO_2 during the surface oxide reduction is used as an indicator for *in-situ* surface oxide detection.
- **Chapter 6:** Chlorine evolution study conducted in my external stay in Spectro Inlets, ApS is given. This study includes testing the activity for chlorine evolution on various catalysts with EC-MS by taking advantage of its high sensitivity towards gaseous products. Moreover, definition of overpotential in the field is discussed and real-time equilibrium potential calculation method is proposed.
- **Chapter 7:** The most important conclusions from this PhD study is given. Subsequently, an outlook is provided for the future studies.

Chapter 2

Overview of Electrocatalytic Oxidation Reactions in This Thesis

In this chapter, overview of the reactions investigated in the scope of this thesis is given. The review involves the importance of the target chemicals propylene oxide (PO) and Cl_2, the current industrial methods for their production, literature review with the recent advances in the field, and research gaps. First part of the chapter is dedicated to electrochemical propylene oxidation and the second part to chlorine evolution reaction (CER).

2.1 Electrochemical Propylene Oxidation

2.1.1 Market and Industrial Methods

This thesis is focused on the production of PO via electrochemical propylene oxidation as it is one of the most economically valuable derivative of C_3H_6. PO is an highly reactive organic belonging to epoxide class. It is a significant precursor for the chemical industry with 10 million tons per year production capacity [12]. In Europe, 14% of the propylene is used for PO production which is the second largest consumption area after polypropylene [13]. PO demand is continuously growing due to the need for PO derivatives mainly as polyetherpolyol with ≈70%, propylene glycol, and propylene glycol ether [14].

Current industrial methods for PO production can be classified in 5 groups [14, 15]:

(1) **Chlorohydrin Process:** This approach involves two consecutive steps. Initially, propylene undergoes a reaction with Cl_2 gas in an aqueous medium, resulting in the production of propylene chlorohydrin. Subsequently, the epoxidation occurs through the reaction between propylene chlorohydrin and either $Ca(OH)_2$ or NaOH. This leads to the formation of PO along with brine waste containing $CaCl_2$ or NaCl. However, a significant drawback of this method lies in the challenge of waste disposal. The process generates a substantial amount of brine waste ($\approx$ 40 times that of PO), which is contaminated with propylene glycol and a byproduct, 1,2-dichloropropane, constituting up to 10% of the waste. These byproducts are non-valuable and require proper disposal, rendering the process less favorable in the industry.

(2) **Organic Hydorperoxide Process:** In this method, alkyl-hydroperoxides are used for epoxidation of propylene. The main disadvantage of this process is by-products exceeding the yield of PO, so demand for their derivatives dominates the supply of PO. The most used alkyl-hydroperoxides are tert-butyl hydroperoxide, ethyl-benzene hydroperoxide, and cumene hydroperoxide and corresponding derivatives methyl tert-butyl ether, styrene, and α-methyl styrene, respectively.

(3) **Hydrogen Peroxide Process:** This reaction is based on the oxidation of propylene to PO via H_2O_2 in a methanol solution by using titanium silicate catalyst. Advantages of this process is that H_2O_2 production and propylene oxidation sites are located in the same plant helps avoiding H_2O_2 transport. With this method, the waste water is reduced 70-80%, and energy consumption is reduced 35% compared to chlorohydrin process. First plant for this process is started in 2006 by BASF and The Dow Chemical Company.

(4) **Direct oxidation:** Direct gas phase oxidation of propylene inspired by ethylene with Ag catalyst is tried to be developed by the researchers. While this method provides over 90% selectivity for ethylene epoxidation, the selectivity is less than 10% for propylene epoxidation due to the hydrogenation of the allyl carbon in propylene. Despite efforts, this approach has not yet achieved commercial viability.

(5) **Hydro Oxidation Process:** This process C_3H_6 undergoes a one-step reaction with H_2, and O_2 in a solvent. The catalyst employed is a noble metal impregnated titanium silicate. Reported selectivity for PO falls within the range of 68-97%. The choice of solvent influences the formation of by-products, including glycols or glycol ethers.

In addition to these methods, attempts for developing a electrocatalytic PO production method is continuing due to the environmental benefits by utilizing renewable energy as an electricity source. In the following section, I will summarize the developments in electrochemical propylene oxidation area, as well as some other electrocatalytic epoxidation studies.

2.1.2 Literature Review

Propylene is an alkene consist of a double-bond and a single bond as illustrated in Figure 2.1. Double-bonded carbon atoms are named as vinylic carbon, and the single-bonded carbon atom as allylic carbon.

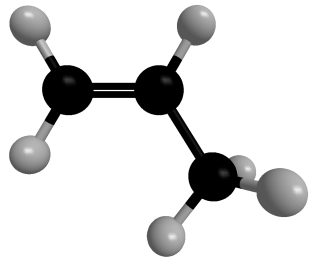

Figure 2.1 Illustration of a propylene molecule.

There are many possible reaction products that can form as a result of the electrochemical propylene oxidation reaction. The possible reactions and corresponding reversible potential for formations are given in Table 2.1 [16]. The existence of numerous possible products naturally emerges a selectivity problem for this reaction.

Table 2.1 The possible propylene oxidation products, their formation reactions and the corresponding reversible formation potentials [16].

Product	Reaction	E_{rev} $[V_{RHE}]$
Propylene Oxide	$CH_2CHCH_3 + H_2O \rightarrow CH_2CHOCH_3 + 2\ H^+ + 2\ e^-$	0.66
Propylene Glycol	$CH_2CHCH_3 + 2\ H_2O \rightarrow CH_2OHCHOH + 2\ H^+ + 2\ e^-$	0.41
Allyl Alcohol	$CH_2CHCH_3 + H_2O \rightarrow CH_2CHCH_2OH + 2\ H^+ + 2\ e^-$	0.25
Acrolein	$CH_2CHCH_3 + H_2O \rightarrow CH_2CHCHO + 4\ H^+ + 4\ e^-$	0.25
Acrylic Acid	$CH_2CHCH_3 + 2\ H_2O \rightarrow CH_2CHCOOH + 6\ H^+ + 6\ e^-$	0.19
Propanal	$CH_2CHCH_3 + H_2O \rightarrow CH_3CH_2CHO + 2\ H^+ + 2\ e^-$	0.15
Acetone	$CH_2CHCH_3 + H_2O \rightarrow CH_3COCH_3 + 2\ H^+ + 2\ e^-$	0.00
CO_2	$CH_2CHCH_3 + 6\ H_2O \rightarrow 3\ CO_2 + 18\ H^+ + 18\ e^-$	0.10

The first electrochemical propylene oxidation study is published in 1965 by Bockris et al. on a platinized platinum electrode in an acidic electrolyte. The only reaction product detected as a result of this study was CO_2 [17]. After this, in 1975 Wise & Holbrook, oxidize C_3H_6 as well as ethylene on Ag electrochemically in NaOH, and as a result reported PO for the first time. Under the reaction conditions, they found that electrode is oxidized and Ag_2O, AgO, and Ag_2O_3 species are found. As this study focused mainly on ethylene epoxidation, information regarding C_3H_6 epoxidation was not thoroughly explored [18]. Chou et al. investigated electrochemical propylene oxidation on stainless steel electrode in 1 M KOH, and reported propylene oxide, propylene glycol, and CO_2 [19]. After this, another study on stainless steel also reported formation of PO and propylene glycol [20]. The electrochemical oxidation of C_3H_6 is investigated on Pd for the first time by Stafford et al. in H_3PO_4 with a flow cell setup and as a result acrolein, acrylic acid, CO_2, and acetone which later on indicated in the paper might be formed due to the homogeneous Wacker-type oxidation reaction of Pd^{2+}, C_3H_6, H_2O [21]. In another study, it is shown that addition on Cl^- to electrolyte resulted in great enhancement in acetone production due to the dissolution

of Pd electrode and consequent Wacker-type oxidation [22]. Otsuka et al. reported an increase in PO and acetone production at above 1.1 V vs. NHE, and the formation of by-products CO_2, acetic acid, and propionic acid is increased above 1.5 V vs. NHE as a result of C_3H_6 oxidation in a fuel cell setup in H_3PO_4. Furthermore, they have noticed that the epoxidation activity increased with the calcination of Pt black, and it is suggested that PtO_2 facilitate active oxygen species' formation. For the epoxidation reaction, Langmuir-Hinselwood mechanism is proposed [23].

After 2003, the first study about electrochemical propylene oxidation is made by Winiwarter et al. on Pd catalyst in 2019. The mechanistic study is performed in the potential range of 0.7 - 1.2 V vs. RHE and revealed the importance of steric effect of C_3H_6 adsorption on the reaction products with the combination of experimental and theoretical work. It is proposed that through the allylic adsorption reaction favors to allylic oxidation products, i.e. mainly acrolein and therefore a catalyst design based on the avoidance of vinylic adsorption would enhance the activity towards allylic oxidation products. On the other hand, vinylic coordination might enable the production of PO and propylene glycol. Even though the PO formation is suggested it could not be detected in this study. Another significant outcome of the study is that Langmuir-Hinselwood mechanism is proposed for the reaction and it is found the the reaction is limited by the adsorption of oxygen species to the surface due to the surface poisoning caused by high carbophilicity of Pd catalyst in this potential range [16].

In the following study, the binding strength of carbon species are tuned by alloying Pd with Au, latter being less carbophilic. As a result, the activity towards allylic oxidation products are increased [24]. Additionally, Koroidov et al. investigated the effect of the oxidation state of the Pd on C_3H_6 oxidation mechanism with X-ray absorption spectroscopy. It is proposed that the allylic oxidation happens on the metallic Pd up to 1.0 V vs. RHE, and with the further increase in the potential to 1.1 - 1.3 V vs. RHE, Pd is oxidized. At these potential range it is proposed that PO forms via vinylic oxidation of C_3H_6. Subsequently, hydrolysis of PO to propylene glycol occurs. It is also shown that presence of C_3H_6 retards the Pd oxidation from 0.8 V to 1.1 V vs. RHE [25].

Following this, Liu et al. investigated the effect of surface oxidation of Pd catalyst on C_3H_6 oxidation by comparing Pd and thermally oxidized PdO. It is reported that

selectivity towards propylene glycol is higher on PdO than on Pd. However, given the fact that dissolution of Pd was higher in the case of Pd electrode than on PdO, the possibility of Wacker-type acetone formation facilitation on Pd due to lower stability is not clarified. Based on the *in-situ* ATR-FTIR (Attenuated Total Reflectance Fourier Transformed Infrared Spectroscopy) experiments on Pd and PdO catalysts at 1.4 V, it is proposed that the C_3H_6 mechanism on metallic Pd is Langmuir-Hinselwood, and on PdO is Mars-Van Krevelen mechanism which is supported with isotope-labelling of oxygen [26]. However, while proposing the reaction mechanism, it is neglected that at 1.4 V vs. RHE Pd should be oxidized. Pd is assumed to be metallic in this study, which is shown to be oxidized at this potential previously by Koroidov [25]. Finally, a direct C_3H_6 oxidation to propylene glycol is proposed without considering PO formation. Moreover, Jong et al. studied electrochemical propylene oxidation on Pd functionalized Ti hollow fibre electrodes and they realized that propylene glycol formation is enhanced at potentials more anodic than 1.2 V vs. RHE, while below this potential acrolein and allyl alcohol dominated the product distribution [27].

In the recent years, in addition to studies on Pd-based catalysts, C_3H_6 epoxidation on PtO_x studied with a solid-polymer-electrolyte electrolysis cell consist of a membrane electrode assembly inserted in a divided glass cell filled with CH_2Cl_2. The electrodes are prepared by partially reducing PtO_2 with N_2H_4 to obtain ($PtO_x(N_2H_2)$), and partially oxidizing Pt black with O_2 to obtain ($PtO_x(O_2)$). As a result, a 10-fold increase in PO production rate is observed in ($PtO_x(O_2)$) showing the importance of the oxidized Pt species on PO formation [28].

On the other hand, Ke et al. utilized Ag_3PO_4 cubes for direct electrochemical C_3H_6 epoxidation and revealed the reaction dependency to facet. The Ag_3PO_4 cubes, mainly exposing (100) facets, outperformed Ag_3PO_4 rhombic dodecahedra (110) and Ag_3PO_4 tetrahedra (111) by 1.6 and 2.5 times in Faradaic efficiency for PO, respectively at 2.4 V vs. RHE.

In addition to the direct electrochemical C_3H_6 oxidation routes, there are also studies enabling indirect oxidation by utilizing halide oxidation, and using halogens as a reactive gas inspired by traditional chlorohydrin process. This concept is first established by Leduc et al. in 1966 [29]. Leow et al, achieved 1 $A\,cm^{-2}$ current density for propylene and ethylene epoxidation with this method [12]. However, as this method

is basically the application of chlorohydrin method in a single electrochemical cell, and does not provide mechanistic insights for the electrocatalytic C_3H_6 epoxidation, it is out of scope of this thesis.

Even though, there are very limited number of studies performed with *in-situ* mass spectrometry methods, Schmidt et al. performed propylene oxidation on Au electrode by using differential electrochemical mass spectrometry (DEMS) in 1996 [30]. Jirkovsky et al. studied electrochemical epoxidation of ethylene on RuO_2 electrodes by enabling Cl^- mediation with DEMS. However, different from the indirect route, it is shown that the ethylene oxide formation starts before the Cl_2 formation. In this study, it is shown that Cl^- prevents the CO_2 formation and promotes ethylene oxide formation. Density functional theory (DFT) calculations proposed two different ethylene adsorbates: (i) parallel binding of ethylene to a surface oxygen atom and named as epoxide-like adsorbate (ii) parallel binding of ethylene to two surface oxygen atoms from each carbon named as diol-like adsorbate. Where epoxide-like adsorbate promotes ethylene oxide formation, diol-like adsorbate promotes CO_2. Addition of Cl^- to electrolyte, provides a blocking effect for some surface sites and prevents diol-like adsorbate formation as it requires more free active sites, therefore enhances epoxide formation activity [31].

Li et al. conducted a significant theoretical investigation into the electrocatalytic epoxidation of C_3H_6 across a range of catalysts. Langmuir-Hinselwood mechanism is proposed for Au, TiO_2, and PtO_2, and Mars-Van-Krevelen mechanism for PdO_2 starting from 1.23 V vs. RHE with the formation of oxygen vacancies. As a result, main competing process with the epoxidation is determined as the initial dehydrogenation of the C_3H_6 which then result in products such as acrolein, allyl alcohol, acrylic acid, and CO_2 [1].

As there are limited number of studies on electrochemical C_3H_6 epoxidation and most of these studies are performed in before 2000, there is a lack of systematic study investigating the electrocatalytic PO synthesis mechanism. Early studies performed in many different electrochemical cells with different type of electrolytes known with their electrode interactions such as phosphoric acid, at varying temperatures and pressures which makes it hard to isolate effects of distinct parameters. Moreover, most of the

studies performed galvanostatically, where potential is not controlled prevents the precise understanding of the reaction mechanism [18–20, 32].

Additionally, in the recent study on the electrochemical C_3H_6 oxidation it is seen that changes in the oxidation state of the Pd under the reaction conditions and unstable reaction products are neglected [26]. Therefore, I believe for this relatively "new" research area establishing careful investigation criteria becomes crucial. Given the significance of oxide formation on the catalyst surface for epoxidation, continuous consideration of the electrode's oxidation state is essential. Moreover, researchers should account for unstable electrochemical C_3H_6 oxidation products, recognize limitations in post-experiment product analysis methods, and take necessary precautions.

2.2 Chlorine Evolution Reaction

2.2.1 Market and Industrial Methods

Chlorine is a significant chemical for many industries due to its wide applications. It serves as a raw material for producing polymers, disinfectants, pharmaceuticals, and organic compounds. Additionally, it finds extensive use in sectors such as wastewater treatment and metallurgy [33, 34]. 88 million tons of Cl_2 is produced every year [33]. According to the report of World Chlorine Council, chlor-alkali is the main production method for Cl_2 with more than 97%. Chlor-alkali process is used for the production of Cl_2 and NaOH with the following reaction [35]:

$$2NaCl + 2H_2O \rightarrow Cl_2 + H_2 + 2NaOH \tag{2.1}$$

In 2020, the technologies regarding to chlor-alkali process was 83% membrane cells, 12.5% diaphragm cells 2.1% mercury cells, and 2.1% others [33]. Commercially, dimensionally stable anodes (DSA) are used for chlor-alkali process. DSA is invented by Beer and it consists of a mixture of RuO_2 and TiO_2 coated on Ti substrate. DSA led to a breakthrough in the chlor-alkali industry by reducing the energy consumption and with an increased stability. Currently, DSA is further developed by the addition of other components into the mixture such as IrO_2, PtO_2, etc [35]. However, with the increasing demand to Cl_2 further development of the catalyst for reaction is getting more and more

important as even small improvements have a great impact due to the size of the market.

2.2.2 Literature Review

CER involves a $2e^-$ transfer process with a standard equilibrium potential of 1.358 V vs. SHE, as presented in Equation 2.2. The competing reaction, oxygen evolution reaction (OER), has a standard equilibrium potential of 1.229 V vs. SHE, as shown in Equation 2.3. While OER is thermodynamically favored, the relatively slow kinetics due to its $4e^-$ transfer, combined with the rapid kinetics of CER results in both reactions occurring over a wide potential range, creating challenges in achieving selectivity [36].

$$2\,Cl^- \rightleftharpoons Cl_2 + 2\,e^- \qquad (1.358\,V\,vs.\,SHE) \tag{2.2}$$

$$2\,H_2O \rightleftharpoons O_2 + 4\,H^+ + 4\,e^- \qquad (1.229\,V\,vs.\,RHE) \tag{2.3}$$

Given that CER occurs in an aqueous environment, it is important to take into account potential reactions between Cl_2 and H_2O when studying the process. Main species form due to Cl_2 hydrolysis are hypochlorous acid (HOCl), hypochlorite (ClO^-), and chlorate ($ClO_3{}^-$). The formation reactions for chlorine species are given below:

$$Cl_2 + H_2O \rightleftharpoons H^+ + HOCl + Cl^- \tag{2.4}$$

$$HOCl + H_2O \rightleftharpoons ClO^- + H_3O^+ \tag{2.5}$$

$$2\,HOCl + ClO^- \rightleftharpoons ClO_3{}^- + 2\,H^+ + 2\,Cl^- \tag{2.6}$$

The concentration of chlorine species varies with pH, as depicted in Figure 2.2. At low pH levels, Cl_2 concentration is high. In the pH range of 1-7.5, HOCl predominates, while at higher pH levels, ClO^- becomes the dominant species.

Even though CER is a simple $2e^-$ transfer reaction, the mechanism is not fully understood yet. Three different mechanisms for CER is proposed in the literature with an active site (*) which can be surface oxygen atom or metal atom:

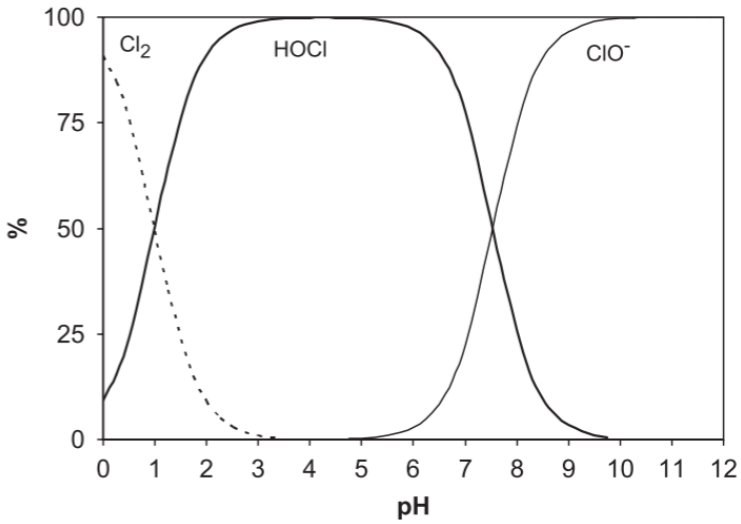

Figure 2.2 Ratios of chlorine species in water as a function of pH at 25°C and 5×10^{-3} M Cl^- concentration. Reprinted from [37] with permission. Copyright 2008 Elsevier.

(1) **Volmer-Tafel (V-T):**

$$2\,\mathrm{Cl}^- + 2^* \rightarrow 2\,Cl^* + 2\,e^- \tag{2.7}$$

$$Cl^* + Cl^* \rightarrow 2^* + \mathrm{Cl}_2 \tag{2.8}$$

(2) **Volmer-Heyrovsky (V-H):**

$$2\,\mathrm{Cl}^- + * \rightarrow Cl^* + e^- + \mathrm{Cl}^- \tag{2.9}$$

$$Cl^* + \mathrm{Cl}^- \rightarrow * + \mathrm{Cl}_2 + e^- \tag{2.10}$$

(3) **Krishatalik:**

$$2\,\mathrm{Cl}^- + * \rightarrow Cl^* + e^- + \mathrm{Cl}^- \tag{2.11}$$

$$Cl^* + \mathrm{Cl}^- \rightarrow Cl^{*+} + e^- + \mathrm{Cl}^- \tag{2.12}$$

$$Cl^{*+} + \mathrm{Cl}^- \rightarrow * + \mathrm{Cl}_2 \tag{2.13}$$

All three mechanisms initiate with the adsorption of Cl^-. In the V-T mechanism, two adsorbed Cl atoms combine to form Cl_2. In the V-H mechanism, adsorbed Cl combines with Cl^- from the electrolyte, resulting in the desorption of Cl_2. In contrast, the Krishatalik mechanism involves the formation of an adsorbed chloronium ion after the combination of adsorbed Cl and Cl^-. Subsequently, the chloronium ion reacts with Cl^- to produce Cl_2 [33].

Theoretical studies focused on understanding the CER reaction mechanism, especially the active sites [38–43]. A foundation of this studies is started by Hansen et al. where the active sites and reaction intermediates are investigated based on DFT calculations and surface Pourbaix diagrams on rutile oxide (110) surfaces. Rutile oxides contains two types of oxygen sites, bridge and cus (coordination unsaturated site). For example in RuO_2 bridge oxygen (O^b) connects two Ru atoms and cus oxygen (O^c) is connected to only one Ru atom. It is found that O^b blocked with oxygen, therefore could not show catalytic activity for OER and CER. Therefore, the active site for both reactions is O^c. $\Delta E(O^c$ is determined as the descriptor as it is linearly related to adsorption energies of chlorine intermediates such as $Cl(O^c)_2$ and $Cl(O^c)$. As the lowest $\Delta E(O^c)$ is determined for $Cl(O^c)$, it is determined as the CER intermediate on IrO_2 and RuO_2, and the reaction mechanism is predicted as V-H [38].

Furthermore, experimental studies are conducted to evaluate the CER performance on different catalysts and to achieve a fundamental understanding of the reaction mechanism to enable rational catalyst design. Activity assessment of electrodes is made by the comparison of the overpotentials. However this becomes cumbersome due to the changes in the equilibrium potential as the Cl_2 fugacity changes over the course of the experiment. This problem is explained and more literature is provided in the Chapter 6. For the observation of Cl_2 different methods are employed: analysis of dissolved Cl_2 with N,N-diethyl-p-phenylenediamine colorimetry [44] and iodometry [45], DEMS [46–49] and on-line electrochemical mass spectrometry(OLEMS) [50], and rotating ring-disk electrode (RRDE) [48, 51–53].

Recently, there are numerous studies on a catalyst design improving the CER performance including but not limited to the development of single atom [54–58], precious-metal free [45, 59], and organo-catalysts [60]. As it is not directly related to the aim of this thesis, I will introduce the studies that facilitates the understanding of

this study in this section mainly being the high activity of Pt-based catalysts and tuning the catalytic activity with top layer coating.

Although theoretical studies have examined the catalytic activity of PtO_2 in CER due to its stability under the reaction conditions according to Pourbaix analysis [38], experimental evidence indicates that the presence of metallic Pt leads to enhanced CER activity [58, 61]. Lim et al. utilized atomically dispersed Pt-N_4 catalysts, revealing improved selectivity and faster kinetics compared to Pt nanoparticles and DSA. In contrast to PtO_2, *in-situ* electrochemical x-ray absorption spectroscopy (XAS) and DFT calculations unveiled direct Cl adsorption onto Pt atoms instead of oxygen atoms, enhancing selectivity by distinguishing the active site for CER from OER [58]. Scanning electrochemical microscopy (SECM) highlighted the significance of Pt^0 in CER activity, with sluggish kinetics observed on PtO_x surfaces. The Pt^0 sites ratio was found to determine Cl_2 selectivity, pointing to a CER mechanism based on Pt-Cl rather than Pt-OCl formation [61]. Overall, Pt's oxidation state under reaction conditions significantly influences CER activity and selectivity. Various studies have demonstrated that Cl^- retards Pt oxidation, emphasizing the need to carefully consider Pt's oxidation state, particularly Cl^- concentration in the electrolyte, based on experimental conditions [48, 62–64].

Furthermore, Exner et al. employed DFT calculations and proposed enhancing CER selectivity while maintaining high activity by introducing a single layer of $TiO_2(110)$ on $RuO_2(110)$, which reduces $\Delta G^0(O_{ot})$ by 1.5 eV [39]. Subsequently, Finke et al. utilized atomic layer deposition (ALD) to deposit thin TiO_2 layers on IrO_2, RuO_2, and Fluorine Doped Tin Oxide (FTO) catalysts to adjust their surface charge density and catalytic activity for CER and OER. This led to a 30 mV decrease in CER overpotential for IrO_2 coated with 3 cycles of TiO_2 and a 100 mV decrease for FTO coated with 10 cycles of TiO_2. The number of TiO_2 cycles versus the CER overpotential curve resulted in volcano shape consistent with the Sabatier principle. However, applying TiO_2 to RuO_2 reduced CER activity. This alteration in catalytic activity is ascribed to changes in the surface electron density of TiO_2 when deposited as a thin layer on the catalyst surface [65].

As described in this section, there are many developments regarding the catalyst design which makes the comparability between different studies critical. The difficulties

in comparability pointed out due to the changing chemical activity of Cl_2 during the reaction conditions and varying experimental conditions having convoluted effects such as electrolyte concentrations. Additionally, the great potential of theoretical studies for predicting enhanced catalysts cannot be neglected. Therefore, it is critical to ensure the precision of the parameters via experiments under the reaction conditions such as the surface oxidation state to guide better theoretical models.

Chapter 3

Experimental Methods

In this chapter, I will introduce the experimental techniques used to study electrochemical propylene oxidation and chlorine evolution reactions. Firstly, I describe the working principle of each technique then explain it's relevancy to this PhD study. In this chapter, I describe catalyst preparation, catalyst characterization, electrochemical mass spectrometry methods.

3.1 Electrode Preparation

For the electrochemical propylene oxidation project, the main goal while preparing the catalysts was obtaining high surface area to compensate low activity. Therefore, I would be able to achieve sufficient concentrations to detect products. As a result, I choose electrode preparation methods that was providing high surface area: hydrogen bubble template and drop-casting methods. For the primary H-cell experiments, I used the hydrogen bubble template method on titanium mesh as a substrate. I tried to use glassy carbon(GC) foam, GC plate, and Pd foil as a substrate too but the mechanical stability and availability of the titanium mesh was superior to others. For the EC−MS experiments, standard 5 mm diameter GC stubs are used as a substrate. Initially, I tried to use hydrogen bubble template method however the binding of the coating on the surface was not strong, and the coating was mechanically falling off. Therefore, I

started using drop casting method and obtain high surface area with a better mechanical stability.

Differently, for the CER project, the aim was preparing different catalysts for the catalyst screening fast and with similar surface roughness. For this reason, I choose magnetron sputtering for the preparation of CER catalysts. In this study, the CER catalysts are prepared with magnetron sputtering by Clara Bruun Jensen, Francesco Longhin and Sahil Garg.

3.1.1 Hydrogen Bubble Template

The catalysts for the electrochemical propylene oxidation reaction are prepared with hydrogen bubble template method to increase the surface area, therefore increase the production rate. This is very important to obtain sufficient concentrations of products for the product analysis.

For this purpose, I have used hydrogen bubble template method as it was also previously used in Anna Winiwarter's thesis for the same reaction [66]. Hydrogen bubble template is an electrodeposition method to obtain high surface area coatings. For the catalysts with high HER activity, when highly cathodic potential is applied to the working electrode H_2 bubble formation and the catalyst deposition simultaneously take place [67]. Formed H_2 bubbles creates a porous film, therefore increased surface area.

For the electrodeposition I used a glass beaker described in Figure 3.1. The counter electrode was 2 Pt mesh electrodes rolled like a ball and located on both sides of the working electrode with an equal distance. The electrolyte was 2 mM $PdCl_2$ in 2 M H_2SO_4. For the H-cell experiments, as the working electrode, I tried different materials. Pd foil, GC plate, GC foam, and Ti mesh. As Pd absorbs hydrogen and production of multiple samples with Pd foil is cumbersome due to the scarcity of available Pd foils in the laboratory, I have eliminated this option. I have obtain satisfactory adhesion of the Pd coating to the substrate with GC plate and the foam. The GC foam has a higher surface area than the plate, but it is very brittle so handling it during the experiments was cumbersome. Therefore, I started using another inert substrate for this reaction, Ti mesh, with a high surface area and sufficient mechanical stability and adhesion.For the EC-MS experiments, GC stubs are used as a substrate. I conducted the deposition

by applying -1 V for 60 seconds to obtain an adhesion layer, and -4 V for 3 minutes. During the deposition, the solution is stirred to elude sticked H_2 bubbles avoiding Pd deposition.

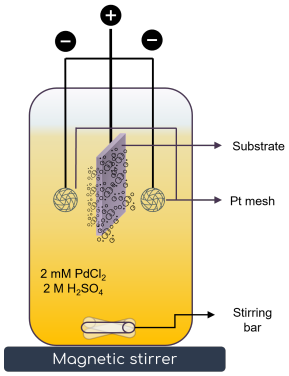

Figure 3.1 A schematic for preparation of electrodes with hydrogen bubble template method consist of an one compartment glass cell.

3.1.2 Drop-Casting

While doing EC-MS experiments with hydrogen bubble template catalyst, I realized that the coating is not mechanically stable enough as it was falling off while mounting the cell. Additionally, with the setup that is described previously, it was hard to reproduce the same experimental conditions such as distance between the counter and working electrodes with the GC stubs due to their shapes. I started using drop-casting method as it was a less complicated and easier to reproduce.

For the preparation of catalyst inks, 20 mg Pt black or Pd black is mixed with 2 mL ultra pure water, 80 µl perflourinated resin solution containing 5 wt.% Nafion. The ink is sonicated for at least 30 minutes and then dropped onto the GC stubs. As the electrochemically active surface area is determined for the all samples with CO stripping the loading of the catalyst is not monitored.

3.1.3 Magnetron Sputtering

Magnetron sputtering is a physical vapor deposition technique conducted in vacuum chamber. I used this method for the CER project to produce thin films for different catalyst materials on GC or Ti stub substrates for the EC-MS experiments.

The technique is based on the ionization of a gas typically Ar by applying potential between the target and the substrate. Then, the positively ionized gas is accelerated towards the target and by the momentum transfer target surface atoms are ejected from the surface which eventually deposited on the substrate. Target is the cathode as it is polarized negatively and substrate is the anode as it is polarized positively [68]. With this technique, one can add a reactive gas flow for example O_2 to form metal oxides. In this thesis, IrO_2 and RuO_2 catalysts are prepared with the addition of O_2 to the sputter chamber.

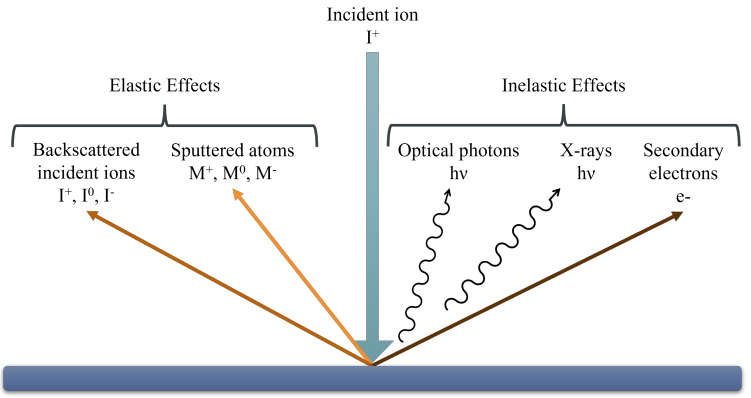

Figure 3.2 Incident ion and target interactions during the sputtering process.

3.2 Characterization Methods

3.2.1 Scanning Electron Microscopy (SEM)

Scanning electron microscopy (SEM) is an imaging technique. The working principle is based on the interactions between electrons and sample. The electrons are emitted from the cathode and accelerated by the application of voltage (typically 0.5 - 30 kV)

between the anode and cathode. The accelerated electron beam is focused on the sample by a lens system consist of condenser and objective lenses to obtain smaller spot size as given in Figure 3.3a.

In Figure 3.3b it is seen that as a result of electron-sample interactions electrons and X-rays are generated and different information about the sample can be obtained by the detection of the different species that are generated.

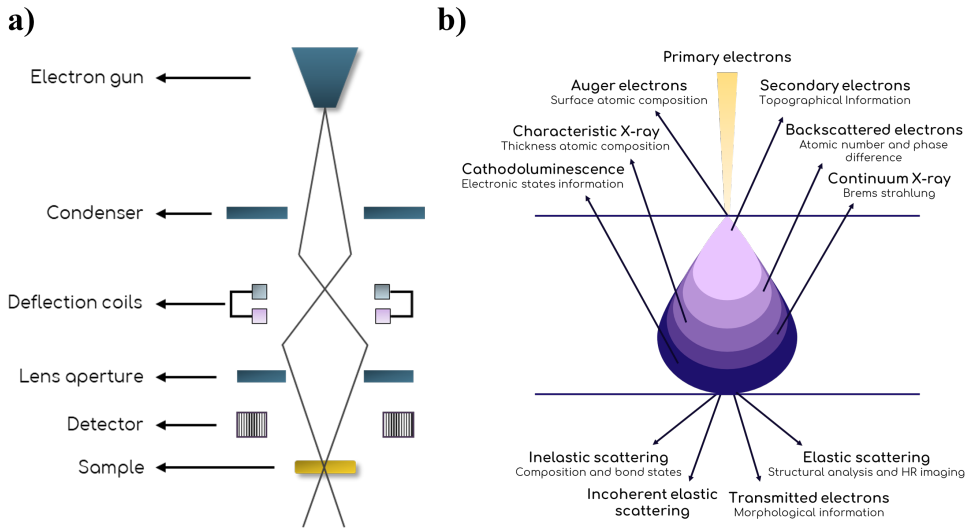

Figure 3.3 (a) Schematic of a SEM with an electron gun, condenser, electromagnetic condensers and deflection coils, and detectors. (b) Electron-sample interactions as a result of electron bombardment in SEM. Adapted from [69]. Copyright 2019, Springer Nature Switzerland AG.

Everhart-Thornley detector (ETD) is used for gathering information from the secondary electrons (SE) or back-scattered electrons (BSE). SE are inelastically scattered and BSE are elastically scattered. Therefore to detect SE the collector grid is positively biased and to detect BSE it is negatively biased by <-50 V which prevents to collection of SE due to their lower energy. The elemental composition data can be obtained from the characteristic X-rays via the energy dispersive X-ray detector (EDX). With the ejection of electrons from the sample, many electron vacancies are formed in atoms' inner shells which creates instability. Thus, electrons from the outer shells fills these places and emits the excessive kinetic energy as X-rays [69].

In this thesis, SEM is used to analyze the surface morphology and coating distribution on the surface for the Pd and Pt catalysts prepared for the electrochemical propylene oxidation project.

3.2.2 X-ray Photoelectron Spectroscopy (XPS)

X-ray photoelectron spectroscopy (XPS) is a surface sensitive technique used for the investigation of the chemical composition and the oxidation state analysis of the surface with the photoelectric effect shown in Figure 3.4. Photoelectric effect is the ejection of the core or valance electron with a binding energy (E_b) from the surface due to the energy of X-rays (photons), indicated as $h\nu$ where h is the Planck's constant and ν is the exciting radiation's frequency. As a result, the kinetic energy of the electrons (E_k) is measured as well as the corresponding photoelectron intensities. From the E_k, the characteristic binding energies (E_b) are found according to the 3.1 where ϕ is the work function of the spectrometer.

$$E_k = h\nu - E_b - \phi \tag{3.1}$$

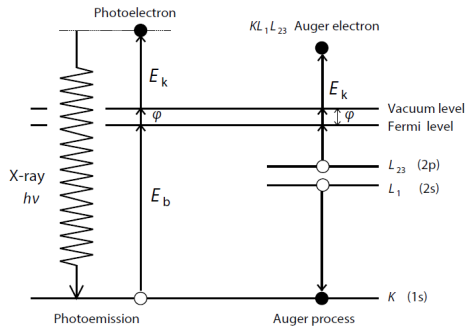

Figure 3.4 Photoelectric effect and Auger described in this schematic. Reprinted from [8] with permission. Copyright 2003 Wiley-VCH Verlag GmbH & Co. KGaA.

The photoelectrons have typically have 0-1 keV kinetic energy and thanks to these low energies XPS is a surface sensitive method providing information from the outermost layer of the surface with less than 2 nm mean free path of electrons. Additionally, due to the low energy of the electrons, XPS requires ultra high vacuum

(UHV) to facilitate the travel of the electrons without interruption. In this study, XPS is used for checking the if there is contamination on the surface [8]. In addition, it is used determination of the oxidation state of the catalyst prepared for the CER project.

3.2.3 Ion Scattering Spectroscopy (ISS)

Ion scattering spectroscopy (ISS) is a technique used for the characterization of surface with the sensitivity of only topmost atomic layers. It is also known as low-energy ion scattering (LEIS). This method involves a bombardment of noble gas ions to the surface of the sample with a certain angle (θ) and a certain kinetic energy (E_0) which is usually 500 eV to 5 keV. As a result of the elastic collision the incident ion scatters from the surface and its kinetic energy (E) is measured. As the process is the binary collusion the following equation is described from the conservation of momentum and energy:

$$\frac{E}{E_0} = \frac{1}{(1+\frac{M_2}{M_1})^2}\left[cos\theta \pm \sqrt{\left(\frac{M_2}{M_1}\right)^2 - sin^2\theta}\right] \tag{3.2}$$

where M_1 is the mass of the projectile and M_2 is the mass of the surface atom. As the θ, E_0, M_1 are set parameters by the user and E is measured, the only unknown M_2 is calculated with the Equation 3.2. Therefore, in the energy spectrum elements giving a peak are identified according to their atomic mass [70]. In this study, ISS is used for detection of the thin TiO_2 on top of Pt coating in the CER project before and after the experiment.

3.3 Electrochemistry

In this section, I will introduce the electrochemical methods I have used for this thesis as well as the electrochemical cell types and the cleaning procedures. All the experiments are conducted with 3-electrode setups using a potentiostat.

3.3.1 Three Electrode Setup

For the fundamental studies it is very important to use three electrode setups instead of two electrode setups. Three electrode setup consists of working electrode (WE), counter electrode (CE), and reference electrode (RE).

Anode is defined as the electrode where the oxidation reaction takes place, and cathode is where the reduction reaction takes place. One should be careful while describing the electrodes as positive and negative as in the electrolytic cells, anode is positively charged and cathode is negatively charged on the other hand in the galvanic cells anode is negatively, cathode is positively charged [10].

Throughout this study, saturated mercury/mercurous sulfate (Hg/H_2SO_4) RE is used. It is calibrated against the reversible hydrogen electrode (Gaskatel GmbH) in the electrolyte. For the CER study, pH of the electrolyte is measured with electronic pH meter and RHE is converted to SHE, according to the Equation 1.14.

3.3.2 Stagnant Thin Layer Cell

The schematic of the stagnant thin layer cell for EC-MS is given in Figure 3.5. In this cell, WE is mounted to the cell with a U-cup assembly well known in rotating disk electrode experiments. The RE and the CE are connected with glass luers on top of the cell. The material of the cell is polychlorotrifluoroethylene (PCTFE). For this study, one disadvantage of the stagnant thin layer cell was the conductivity loss due to bubble formation due to excessive gas formation at high currents.

3.3.3 Cleaning

The glassware and the electrochemical cells are cleaned thoroughly to avoid organic and metal contamination. To clean organics piranha solution made by mixing H_2O_2 and H_2SO_4 at 1:3 ratio is used for overnight. After this, the objects rinsed with ultra pure water. Then, they are immersed in *aqua regia* solution made by mixing HNO_3 and HCl at 1:3 ratio again for overnight and afterwards rinsed with ultra pure water. Finally, all of the objects are boiled in ultra pure water for at least 2 hours prior to experiments.

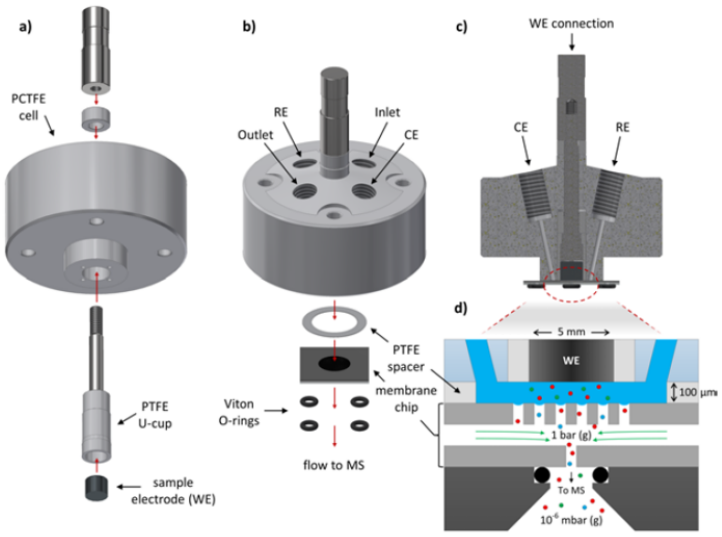

Figure 3.5 (a) Schematic of stagnant thin layer cell used in EC-MS showing the WE assembly with a u-cup. (b) Schematic showing the inlets and outlets of the cell together with positioning on top of the membrane chip separating the cell and MS. (c) Visual of the cell's cross section showing the connection of WE, RE, and CE with the sampling volume located on top of the membrane chip. (d) Detailed illustration of cell, membrane chip, and MS during an experiment. Reprinted from [71] with permission. Copyright 2018 Elsevier Ltd. All rights reserved.

3.3.4 Electrochemical Techniques

The most significant conclusions in this thesis drawn from the results of electrochemical tests. Therefore, it is very important understand different methods to conduct them properly. In this section, I will describe the electrochemical methods and their specific purposes in this thesis.

Electrochemical Impedance Spectroscopy (EIS)

Electrochemical impedance spectroscopy (EIS) is a technique in which small perturbations by an alternating source on the potential or current is applied to the electrochemical system. As the perturbation is small, the system remains at steady state and the non-linearity caused by the electron transfer at large perturbations are avoided. This eases

the application of mathematical models to obtain information about the electrochemical system [10, 72].

EIS is based on the measurement of the impedance according to frequency. Impedance ($Z(\omega)$) is defined as:

$$Z(\omega) = Z_{Re} - jZ_{Im} \tag{3.3}$$

Z_{Re} represents the real, Z_{Im} the imaginary part of the impedance. By plotting Z_{Im} as a function of Z_{Re} one can obtain a Nyquist plot, 3.6. Corresponding cell model for the plot in Figure 3.6a is called as Randles cell given in Figure 3.6b. This cell consists of a solution resistance (R_s), a double-layer capacitor (C_{dl}), a charge transfer resistance (R_{ct}) and a Warburg impedance related to diffusion(W) [73]. I used this technique to determine the solution resistance so that I can compensate as described in the following section.

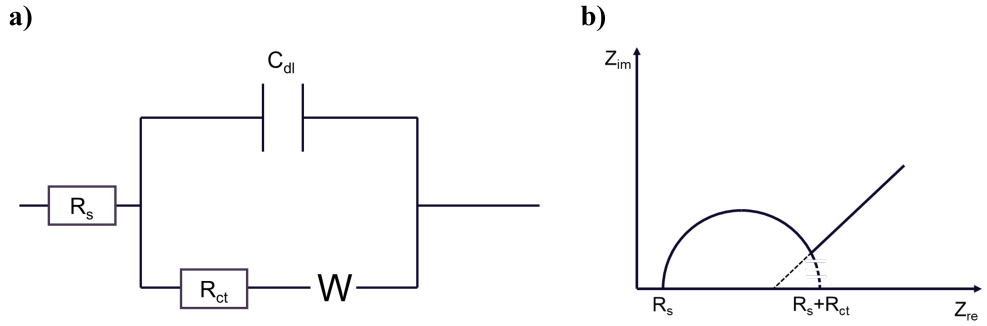

Figure 3.6 (a) Representation of Randles cell model involving solution resistance (R_s), a double-layer capacitor (C_{dl}, a charge transfer resistance (R_{ct}), and a Warburg impedance (W)). (b) Nyquist plot of the model Randles cell.

Ohmic Drop Compensation

While determining the absolute potential of the WE, one should consider that there is a resistance between the WE and the RE due to the electrolyte. Therefore, compensating the ohmic resistance is a necessary practice. The actual potential at the WE (E_{WE}) is

deviated from the applied potential (E_{ap}) as the iR amount due to the solution resistance as given in 3.4 where I is current and R is the resistance [10].

$$E_{appl} = E_{actual} - iR \tag{3.4}$$

In this study, for all the experiments EIS is applied to find the solution resistance. Afterwards, the ohmic resistance compensated manually by 85%. As the resistances were not exceeding 20Ω, the remaining 15% is neglected.

Cyclic Coltammetry (CV)

Cyclic Voltammetry (CV) is a widely used electrochemical technique that can give many useful information. It is based on the potential sweep of the WE with a certain scan rate and recording the current response as a result.

As given in 3.7, potential is sweeped towards a direction, in this case initially towards more anodic potentials, so this sweep is called as oxidative or anodic scan. When, the potential reaches to the most anodic potential defined in the method by user, potential starts going into the cathodic direction and this scan is called as reductive or cathodic scan. One can observe the oxidation reactions during the anodic scan and reduction reactions during the cathodic scan as the current starts increasing at these potentials. If the reaction appears as a peak this means that after the peak current reaction becomes mass transfer limited current starts decreasing [74].

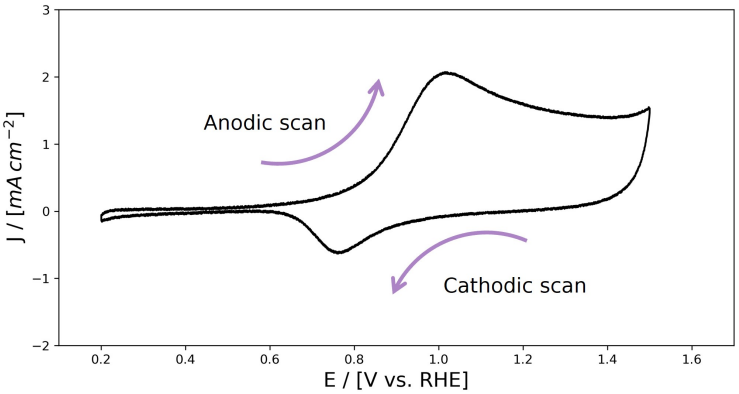

Figure 3.7 An example cyclic voltammetry with potential scan in between 0.2 - 1.5 V vs. RHE.

CV is used in this study for two purposes: (i) to estimate the surface area explained in electrochemically active surface area section, and (ii) to monitor overall reactions happening in a large range of potentials together with mass spectrometry. Even though, CV is a fast and very informative for seeing the overall reactions, I considered the limitations of CV for the mass spectrometry application. First of all, as there is a mass transport delay for species to reach to the mass spectrometer there is a delay between the ion current signals and the electrochemical current. Thus, to asses the catalytic activity at a certain potential I used constant potential experiments. Secondly, as the surface coverage depends on the overpotential, driving conclusions for activity with CV could be misleading so again constant potential experiments are more precise for this purpose [75].

Chronoamperometry (CA)

Chronoamperometry (CA) is a method where a constant potential is applied to the working electrode typically with respect to the RE, and the current response is recorded. It is a commonly used method for evaluating the activity of the catalysts depending on the potential by obtaining the partial current densities [10]. In this thesis, I used this method to evaluate both electrochemical propylene oxidation catalysts and CER catalysts. When a potential applied to the WE suddenly, it is normal to observe an initial high current due to the capacitive charging, to minimize this one can sweep to potential to the target potential slowly.

Chronopotentiometry (CP)

In Chronopotentiometry (CP), the user sets a constant current and the potentiostat applies the required potential to achieve the set current [10]. This is not an ideal method to assess the catalytic activity as the overpotential is the changing parameter. In this thesis, this method is only used for the calibration of Cl_2 in EC-MS which described in Chapter 6.

Electrochemically Active Surface Area (ECSA) Determination

As the real surface area of the electrodes differ from the geometric surface area it is important to assess the real surface area to compare the catalytic activities. The real surface area of the electrodes are named as electrochemcially active surface area (ECSA) and there are different methods to measure this for different materials. A good review about the calculation of ECSA for different materials can be found in [76].

Most importantly for the high surface area electrodes made of Pd and Pt the determination of ECSA is crucial. For these two metal CO stripping is a common method to measure ECSA. CO stripping method is based on the adsorption of one monolayer CO molecules to the surface and with the anodic sweep of the CV oxidation of all the CO to CO_2 with 100% Faradaic efficiency. In Figure 3.8 experimental protocol is given. As a result, one can calculate the charge spent for this reaction with the integration of the oxidation peak, and therefore the amount of CO adsorbed on the surface (a representative CV can be seen in Figure 3.9).

Step 1	Step 2	Step 3	Step 4	Step 5
Get rid of all the residual gases in the electrolyte	Get the baseline CV	CO adsorption to the surface	Purge out all the CO in the electrolyte	Oxidize all CO to CO_2
Ar purge	Ar purge	CO purge	Ar purge	Ar purge
Double-layer potential	Cyclic Voltammetry	Double-layer potential	Double-layer potential	Cyclic voltammetry (Start with the anodic scan)

Figure 3.8 Protocol for the CO stripping experiment to determine the ECSA involving five steps.

In this thesis, for Pt and Pd 410 μC cm^{-2} is assumed to strip one monolayer of CO [76].

3.4 Electrochemical Mass Spectrometry (EC-MS)

The main instrument used in this thesis is electrochemical mass spectrometry (EC-MS). EC-MS is an instrument enabling the real-time detection of the electrochemical reaction products with a mass spectrometer. It consists of an electrochemical cell in ambient

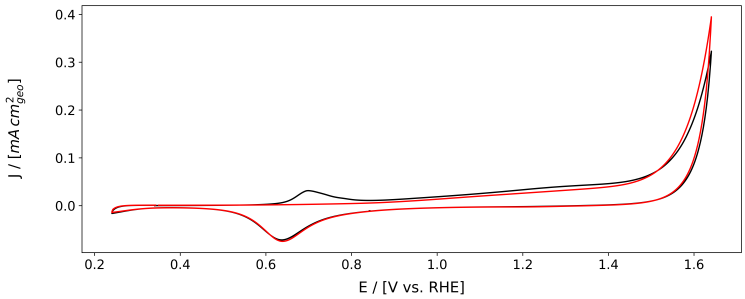

Figure 3.9 An example for a CO stripping experiment to determine ECSA. CV without CO adsorption (black) and CV with CO adsorption (red) is plotted together. The CO oxidation peak appears at $\approx$ 0.7 V vs. RHE when the CO is adsorbed on the surface (black), and it is absent when the electrolyte is purged only with an inert gas but no CO (red).

conditions and a vacuum chamber housing the mass spectrometer. A membrane chip with a 100% collection efficiency is used for the separation of these two different pressures as well as the liquid-gas interface [77].

3.4.1 Mass Spectrometry (MS)

It is important to understand the working principle of MS to utilize the full potential of EC-MS. MS is used for the detection of to mass-to-charge ratios of the ionized molecules. There are different kinds of mass spectrometers and ionization methods available but as in EC-MS quadrupole mass spectrometer (QMS) and electron ionization (EI) is used so this section will focus on that.

QMS consists of 3 main elements: (*i*) Ionization source, (*ii*) QMS, (*iii*) ion detector as given in Figure 3.11.

Ionization source The initial step in MS is the ionization of the analyte molecules at the ionization source. Here, electrons are generated by thermoionic emission by a resistively heated filament and when the molecules entered to the ionization chamber they ionized with the bombardment of the electrons generated in the filament. Later on they are directed to the mass analyzer with the repeller (an electrode with a low voltage applied on to direct the generated ions). For the most molecules, the ionization cross-section, definition, is at it's maximum at around

70 eV. Even though I conducted the experiments at 70 eV, I have also tried lower ionization energies to avoid the formation of HCl^+ which was unsuccessful.

Quadrupole Mass Filter (QMS) QMS (Figure 3.11) is used for filtering ions with different mass-to-charge ratios (m/z) and it consists of 4 parallel rods and the opposite rods have the same potential consists of direct current (DC) and alternating current (AC) parts given in Equation 3.5 and the other pair has the opposite polarity.

$$\Phi_0 = U + V cos\omega t \tag{3.5}$$

The voltage can be adjusted to a field that would allow only a certain m/z ions to pass and the smaller or larger m/z ratios would be expelled out of the poles due to the unstable motion. The ions that can reach to the detector is called as resonant ions, the rest of the ions that cannot react to the detector are called as non-resonant ions. As the electrical field in the QMS changes over time the ions with different m/z would be filtered and reach to the detector over time.

Detector In the end, the ions with varying m/z values are directed towards the detector. In EC-MS, there are two options for a detector: the Faraday cup or the secondary electron multiplier. In this study, I consistently used the secondary electron multiplier due to its superior sensitivity, so I will focus on explaining its functionality.

The secondary electron multiplier (Figure 3.10) comprises a series of cup-shaped dynodes. The ions enter a tunnel formed by these dynodes, and upon collision with the dynode surfaces, secondary electrons are emitted. These secondary electrons are then accelerated towards a positively charged electrode located at the end of the multiplier, leading to the emission of additional electrons. As a result, even a small number of ions reaching the first dynode can generate a signal within the range of 10^{-12} A. The secondary electron multiplier effectively amplifies the signal with a gain ranging from 10^6 to 10^8 times.

As the secondary electron multiplier ages over time, to obtain the same performance it's potential should be tuned periodically. In this study, the secondary electron multiplier potential is tuned before every experiment to obtain N_2 signal from air at 10^{-7} A [78].

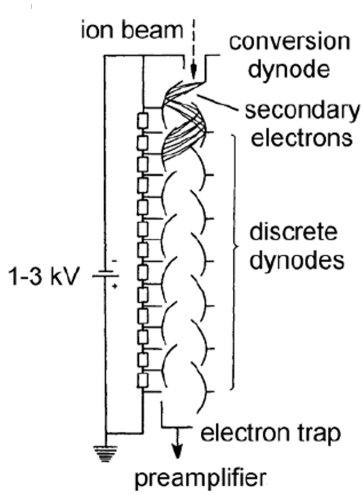

Figure 3.10 Schematic of secondary electron multiplier. Reprinted from [78] with permission. Springer International Publishing AG 2017.

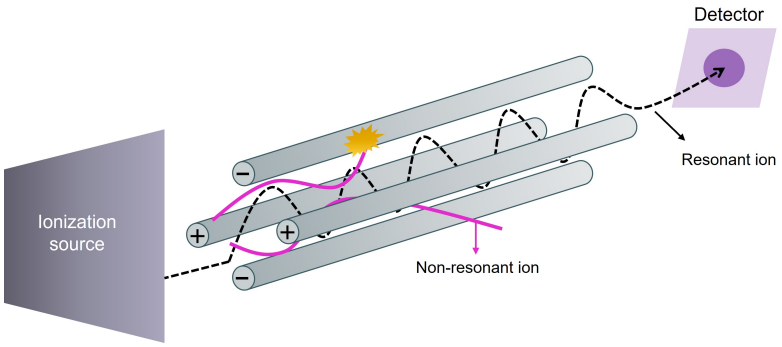

Figure 3.11 Schematic of quadrupole mass spectrometer (QMS) consist of an ionization source, a QMS filter, and a detector.

3.4.2 Membrane Chip

In this section, I will describe the membrane chip and how I utilized it's properties for the specific applications of propylene oxidation and CER. The detailed description about the membrane chip design could be found in Daniel Trimarco's PhD thesis [77]. The functions of the membrane chip are:

(i) Separation of the liquid and gas phase with the hydrophobic coating

(ii) Reducing the ambient pressure to approximately 10^{-6} mbar with a capillary while keeping the same partial pressure of the analyte.

The membrane chip is made of an hydrophobic coating on top with micro pores to allow volatile species and a sampling volume below with a carrier gas to keep the pressure at 1 bar. Finally, the sampling volume is connected to the mass spectrometer with a micro capillary which allows the passage of finely defined number of molecules. The the hydrophobic coating on the membrane chip prevents aqueous electrolytes transport to the sampling volume and only vapors can pass through it based on the Henry's law of volatility given in Equation 3.6:

$$K_n^{pc} = \frac{p_n}{C_n} \tag{3.6}$$

where K_n^{pc} : Henry's law constant for volatility, p_n : partial pressure of the analyte, and C_n : concentration of the analyte.

By this way, the partial pressure of the analyte above the membrane and in the sampling volume remains the same. After all the volatile species equilibrated in the sampling volume at 1 bar, a well defined portion of this mixture is transferred to the MS through the micro capillary. Important note here is that, the partial pressure of the individual species going to the MS remains the same above the membrane chip, in the sampling volume, and in the MS chamber which enables the calculation of real-time equilibrium potential of CER explained in Chapter 6.

As I described above the total flux of molecules going to MS are well defined with the Equation 3.7:

$$\dot{N}_0^v = \frac{1}{k_B T} \times S \times P_{MS} \tag{3.7}$$

where $\dot{N}_0^v$: total molecular flux, k_B: Boltzmann's constant, T: temperature, S: turbo-molecular pump speed, P_{MS}: pressure in the MS chamber.

The EC-MS system has remarkable 100% collection efficiency for gases, however it should be recognized that compounds with slow evaporation rates will always have lower concentrations leading to reduced sensitivity. In cases the volatility is low enough, the analyte cannot be detected with MS due to very low concentrations which makes the base for the detection of PO with EC-MS described in Chapter 4.

3.4.3 Mass Transport in EC-MS

In the EC-MS system, it is known that there is a delay in the MS signal compared to the electrochemistry signal due to the fact that species produced as a result of Faradaic reactions needs to be transported from the electrode surface through electrolyte via diffusion, then pass through the membrane chip, and finally travel in the vacuum to arrive to the mass spectrometer for the detection [71]. The membrane transport depends on the volatility of the species heavily with the following equation:

$$h_n = K_n^{pc} \frac{1}{p} \frac{1}{A} \dot{N}_0 \tag{3.8}$$

where h_n: mass transfer coefficient, p: pressure (1 bar), A: membrane chip area, and $\dot{N}_0$: molecular flux across the membrane chip.

Then, the characteristic time constant of the species in the stagnant thin layer cell is defined with the following equation:

$$\tau_n = \frac{L^2}{2D_n} + \frac{L}{h_n} \tag{3.9}$$

where τ_n is the characteristic time constant, L is the diffusion length, D_n is the diffusion constant. According to Equation 3.8 and 3.9 the characteristic time constants for some relevant species are calculated in Table3.1.

Table 3.1 The characteristic time constants for the relevant species in the EC-MS system. Diffusion constants are gathered from [79] for PO and from [80] for the rest fo the species. Henry's law constants are gathered from [81].

n	K_n^{pc} $[Pa\,m^3\,mol^{-1}]$	D_n $[m^2\,s^{-1}]$	τ_n [s]
H_2	1.3×10^5	4.5×10^{-9}	1.7
O_2	8.3×10^4	2.1×10^{-9}	3.3
CO_2	3×10^3	1.9×10^{-9}	27
PO	19.28	1.2×10^{-9}	3757
Acetone	3.41	1.3×10^{-9}	21658
Cl_2	1077	1.25×10^{-9}	72

3.4.4 Ion Gauge Pressure Sensor

In EC-MS, an ion gauge is employed to measure the pressure within the MS chamber. Understanding the working principle of ion gauge is important to be able to calculate the total molecular flux to MS which is relevant in Chapter 6 for the calculation of real-time CER equilibrium potential. Ion gauges are utilized for pressure measurements in high vacuum conditions. Illustrated in Figure 3.12, the ion gauge comprises a heated filament that emits electrons. These emitted electrons are accelerated towards an anode, and their high energy leads to the ionization of gas molecules upon collision. The resultant positively charged ionized gases collide with a collector wire, generating a measurable current. This current, derived from the collector wire, directly correlates with the particle density [82, 83].

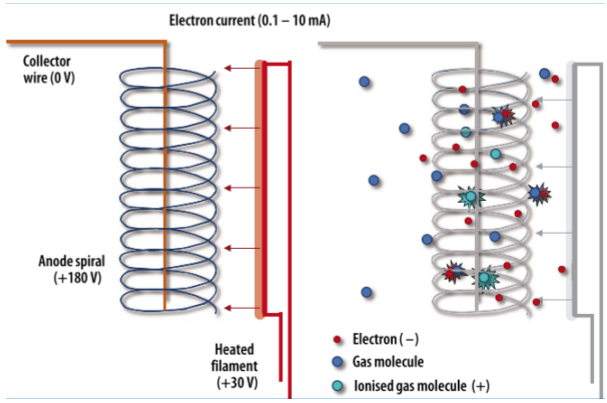

Figure 3.12 Schematic of an ion gauge. Reprinted with permission from [82]. Copyright 2017 WILEY-VCH Verlag GmbH & Co. KGaA, Weinheim.

Thereby, with an ion gauge, one measures the particle density but not the true pressure. Sensitivity of the ion gauge depends on the ionization probability of the gas. Manufacturers usually calibrate the ion gauge for N_2 and user should convert the pressure for the gas that is used in the specific experiment with the following equation [83]:

$$P_i = \frac{P}{f_i} \tag{3.10}$$

where, P_i is the pressure of gas i, P is the pressure read by ion gauge which is calibrated for N_2, and f_i is the gas correction factor. Relevant gas correction factors for this thesis are 0.18 for He and 0.68 for Cl_2 [84].

Chapter 4

Detection of Propylene Oxide via EC-MS

To facilitate the investigation of electrocatalytic reactions, the crucial initial task for researchers is to detect the resulting product. In this study, the focus was on detecting PO, which is not only the most economically valuable product but also one of the most technically challenging to produce through the traditional industrial methods. However, the detection of PO proves to be a complex process due to its distinctive physical and chemical properties. Additionally, the sluggish reaction rates of propylene oxidation result in low concentrations, further complicating the detection process of PO.

4.1 Challenges in Propylene Oxide Detection

In this section, I will describe the roots of the detection difficulty of PO. First of all, it is important to acknowledge that the concentration of PO resulting from propylene oxidation is inherently low due to the sluggish reaction kinetics. Consequently, the limited quantity of PO poses a challenge for its detection using various product analysis methods. The low concentration hinders the application of many analytical techniques, making the accurate detection of PO a difficult task.

Furthermore, it is crucial to consider the reactivity of PO. Particularly in aqueous solutions, PO hydrolysis to propylene glycol can occur which is catalyzed with acids

and bases:

$$CH_3CHCH_2O \xrightarrow{H_3O^+ \, or \, OH^-} CH_3CH(OH)CH_2OH$$

This well-established reaction also known as ring opening reaction poses a challenge for post-experiment analysis methods, as the PO present during the reaction may potentially transform into propylene glycol. This situation can lead to erroneous detection or inaccurate quantification of PO. Moreover, the misinterpretation of the reaction mechanism can arise since some researchers solely rely on *ex-situ* product analysis methods, consequently overlooking the presence of PO and proposing direct oxidation of propylene to propylene glycol [26].

When it comes to detecting PO, an additional important aspect to consider is its highly volatile nature. PO exhibits a relatively low boiling point of 34°C and possesses a Henry's law volatility constant of 19.28 $Pam^{3\,-1}$. At a standard temperature of 25°C, it exerts a substantial vapor pressure of 538 mmHg. These characteristics contribute to the propensity of PO to readily evaporate.

The high volatility of PO presents a significant challenge in detection of the compound using *ex-situ* liquid analysis techniques, such as HPLC (High-Performance Liquid Chromatography) or NMR (Nuclear Magnetic Resonance). During the process of conducting *ex-situ* liquid analysis, a considerable portion of PO may have already evaporated, making its detection and quantification more challenging. For instance, Ko et al. demonstrated that when producing PO through a photo-electro-heterogeneous catalysis method, more than 95% of the PO was evaporated within a span of five hours [85]. This finding underscores the limitations of relying solely on *ex-situ* liquid analysis methods for PO detection. The loss of PO due to evaporation greatly diminishes the effectiveness of these methods, as only the remaining fraction that has not evaporated and has not undergone hydrolysis in the electrolyte can be sampled and analyzed. Moreover, the use of elevated temperatures within the HPLC column, employed to enhance separation and detection, can inadvertently accelerate the hydrolysis reaction rates of PO. As a consequence, the chances of successful detection of PO using *ex-situ* liquid analysis methods are further reduced.

Therefore, due to the compound's high volatility and the associated challenges posed by its evaporation and hydrolysis, alternative approaches or modifications to

ex-situ liquid analysis methods are often necessary to ensure accurate and reliable detection of PO in electrochemical systems. On the contrary, the utilization of *ex-situ* gas analysis methods, such as gas chromatography, presents an alternative approach. However, it is important to note that in this scenario, the already low quantity of PO may be further diluted due to its mixing with a carrier gas. As a consequence, the detection of PO becomes challenging and may result in its failure to be detected using this method. During my PhD, I have attempted to detect PO with HPLC and gas chromatography by preparing PO containing standard solutions, however I could not detect PO with both methods.

4.2 *In-situ* Detection via EC-MS

I decided to use EC-MS to detect PO the following reasons:

1. **Low reaction rates:** EC-MS enables the detection of very small quantities thanks to the large surface area to electrolyte ratio, resulting in concentrated analyte. Furthermore, the complete collection efficiency of 100% ensures that all analyte is directed to the MS.

2. **Low stability of PO:** As PO undergoes a hydrolysis reaction in the aqueous solution, employing real-time product analysis method is beneficial to avoid waiting time in the electrolyte.

3. **High volatility of PO:** The sensitivity of MS towards an analyte is enhanced with increasing volatility, as elucidated in Chapter 3. Consequently, the notable volatility of PO provides an advantageous opportunity for its detection, as its vapors are detectable in the MS.

4. **Safety:** As PO is highly carcinogenic and explosive, production of high amounts of PO in the laboratory environment requires additional precautions. However, with EC-MS one can detect very small quantities, therefore the harms from PO is minimized.

However, the detection of PO using EC-MS is not without its inherent challenges. The electrochemical propylene oxidation reaction is known for its complexity, involving

multiple potential reaction products listed in Chapter2. When it comes to the separation and detection of these organic compounds using EC-MS, the task becomes cumbersome. This is primarily due to the possibility of these compounds possessing the same mass-to-charge ratio (m/z), which complicates the detection process.

PO, with a molecular weight of 58.08 $g\,mol^{-1}$, displays a mass spectrum given in Figure4.1 when subjected to ionization energy of 70 eV in mass spectrometry. At this ionization energy, the peak with the highest relative intensity is observed at m/z = 28. The relative intensity in the mass spectra indicates the quantity of ions produced relative to the most abundant m/z value. However, it is important to consider that at m/z = 28, fragments derived from CO, CO_2, but most importantly C_3H_6 can be detected. Considering that C_3H_6 is employed as a carrier gas, the effects of its fragments become dominant within the mass spectrum. Consequently, the contribution of other signals becomes indistinguishable or obscured, making it challenging to differentiate and accurately quantify these individual signals.

In mass spectrometry, the probability of signal overlap among different species increases as the m/z decreases, primarily due to the fragmentation of these species. Consequently, to minimize signal overlap and ensure reliable detection, it is advisable to concentrate on higher m/z values.

In the case of PO detection, the second-highest signal observed at m/z = 58 holds particular interest. This specific m/z value is chosen because it not only represents PO but also exhibits a significantly high intensity, as depicted in the corresponding Figure4.1. By focusing on the m/z = 58 signal, it becomes more feasible to accurately detect and quantify PO, while reducing the potential for signal interference or overlap from other species.

While the likelihood of signal overlap is reduced at m/z = 58, it is important to acknowledge that certain compounds can still exhibit similar signals, potentially overlapping with PO. Among the possible propylene oxidation products, propanal, acetone, and allyl alcohol are known to generate a signal at m/z = 58. Consequently, it becomes crucial to differentiate between these molecules in order to validate that the observed signal at m/z = 58 indeed originates from PO.

The Table 4.1presents the Henry's law constants for volatility and the relative intensities at m/z = 58 for PO, acetone, propanal, and allyl alcohol. Notably, PO

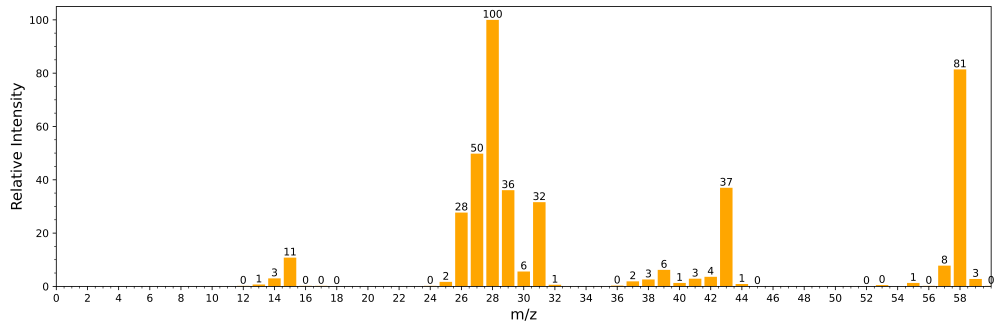

Figure 4.1 Mass spectrum of PO at 70 eV ionization energy. Data retrieved from NIST [86].

exhibits significantly higher volatility compared to the other compounds. This enhanced volatility facilitates the detection of PO using EC-MS, as indicated by the equation 3.6.

Moreover, examining the relative intensities at m/z = 58 provides further insights. Acetone and allyl alcohol demonstrate relative intensities of 25 and 23, respectively, implying that only 25% and 23% of the highest signal would appear at m/z = 58 for these compounds. This observation suggests that the detection of acetone and allyl alcohol at m/z = 58 may be hindered due to their relatively lower intensities compared to the highest signal.

Conversely, propanal exhibits a relative intensity of 100 at m/z = 58, indicating that the entire highest signal would be observed at this m/z value for propanal. However, it is important to note that the likelihood of propanal production via electrochemical propylene oxidation on Pd and Pt catalysts is exceedingly low as it is not reported previously.

Table 4.1 Species that can give a signal at m/z = 58 and their Henry's law constant for volatility obtained from [81], and relative intensity at m/z = 58 [86].

Species	K_n^{pc} $[Pa\,m^3\,mol^{-1}]$	Relative intensity at m/z = 58
Propylene oxide	19.28	81
Acetone	3.41	25
Propanal	7.87	100
Allyl alcohol	0.57	23

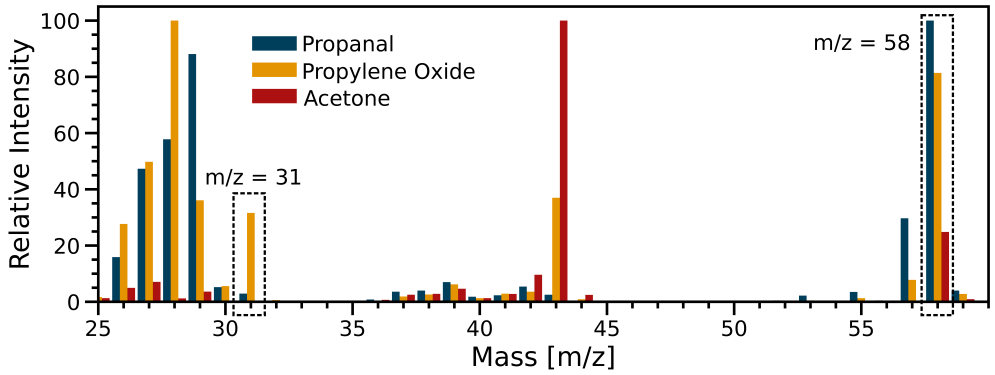

Figure 4.2 Mass spectrum of acetone, propanal, and PO from m/z = 25 to 60 at 70 eV ionization energy. Data retrieved from NIST [86].

In order to assess the detectability of other species using EC-MS, a calculation was performed to determine their expected concentrations based on the 30 minute experiments conducted at constant potential in between 1.0 to 1.6 V vs. RHE while purging C_3H_6on PtO_x and PdO_x catalysts. Standard solutions with the relevant concentrations were then introduced to the EC-MS system to evaluate their detectability within the experimental conditions employed in this study. The results and details about the 30 minutes constant potential experiments are presented in the following chapter. This chapter only focuses on the assignment of m/z = 58 signal to PO.

Firstly, the amount of charge consumed during each 30-minute experiment was calculated given in 4.3. Afterwards, the amount of the specific compound of interest was determined by assuming a Faradaic efficiency based on Equation 1.12. For acetone a Faradaic efficiency of 60% is assumed as in the literature maximum Faradaic efficiency for acetone is reported is 47% on PtO_x catalyst [28] and $\approx$ 25% is reported on Pd catalyst [16]. For propanal, a Faradaic efficiency of 10% is assumed, based on the fact that there are no studies in the literature reporting propanal formation as a result of electrochemical propylene oxidation on Pt or Pd catalysts. It is important to note that the charge calculated represents the accumulation of the analyte over the 30-minute experimental duration, however the MS signal is observed in real time under constant evaporation. Therefore, these concentrations reflect the most extreme scenario at their

maximum values. In reality, as the analyte is continuously transported to the mass spectrometer through evaporation, it is not expected to accumulate to such an extent.

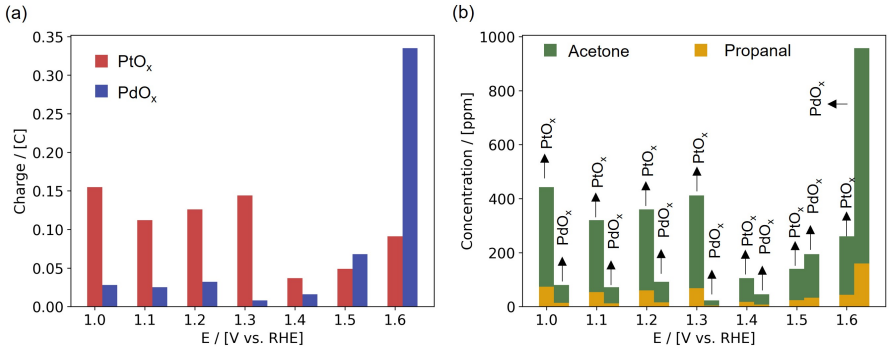

Figure 4.3 (a) Cumulative charge consumed during the 30 minutes experiments at each potential given for PtO_x (red bars) and PdO_x (blue bars). (b) The maximum expected concentrations of acetone (green bar) and propanal (yellow bar) calculated by the assumption of Faradaic efficiencies mentioned in the text given for each potential PtO_x (left bars) and PdO_x (right bars). Details about the calculations and assumptions are given in the text.

In this phase, a series of distinct concentrations of both acetone and propanal were prepared. Subsequently, these samples were introduced to the EC-MS system for analysis. The experimental setup involved mounting the electrochemical cell on top of the membrane chip, followed by the careful introduction of the prepared samples using a syringe.

Once the samples were successfully introduced into the electrochemical cell, a mass spectra was recorded, encompassing the entire range of m/z ratios from 0 to 60. The main objective of this experimental procedure was to monitor and analyze the changes in signal intensities and profiles exhibited by acetone and propanal throughout the entire m/z range. The recorded full mass spectra, as depicted in Figure 4.4, facilitated a thorough examination of the signal behavior and characteristics.

In Figure 4.4 the results indicate that at m/z = 58, acetone concentrations of 100 ppm and 500 ppm are not detectable. However, at 1000 ppm acetone, a detectable signal with an $\approx 10^{-12}$ A is observed. Similarly, at 1000 ppm propanal, a signal of $\approx 2 \times 10^{-12}$ A is detected, whereas propanal concentrations of 100 ppm and 500 ppm are not detectable. Due to the substantially lower volatility of allyl alcohol compared to these compounds, as well as its low relative intensity at m/z = 58 given in Table 4.1, it

is not considered worthwhile to introduce it for detection purposes since it cannot be detected. Therefore, m/z = 58 is assigned for PO.

PO with known concentrations could not be introduced to EC-MS for detection limit determination due to several reasons. First of all, I was not able to eject a precise amount of PO from the chemical bottle that is sealed with a septum to prevent air exposure which would cause an explosion. I have used an analytical syringe with high precision to take PO from the bottle. However, due to high volatility of PO, it immediately starts dripping. Additionally, during the real experiments, PO is produced and immediately measured with EC-MS. However, while preparing a standard solution, fast evaporation of PO from the standard solution and hydrolysis to propylene glycol until the introduction to EC-MS is unavoidable.

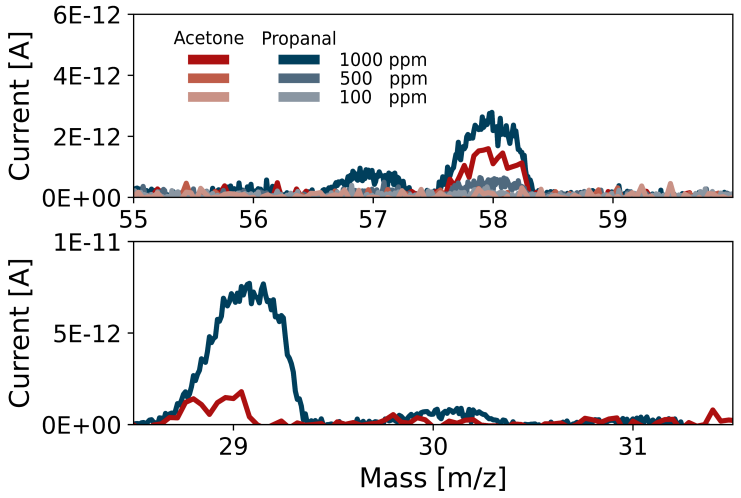

Figure 4.4 Mass spectrum of propanal and acetone introduced to EC-MS. From m/z = 55 to 60 in the upper panel, and from 28.5 to 31.5 in the bottom panel, showing that there is not increment at m/z = 31 for both species.

An additional remark is that, in Figure 4.4, it is evident that neither acetone nor propanal produces a signal at m/z = 31, even at concentrations of 1000 ppm, which aligns with their respective mass spectra provided in Figure 4.2. Additionally, when I introduce PO to the EC-MS, it is seen that the signal at m/z = 31 increases given in Figure4.5. Hence, m/z = 31 holds potential for serving as a PO indicator. Despite the simultaneous increase in m/z = 31 and m/z = 58, indicating the production of PO

at anodic potentials above 1.0 V vs. RHE, I refrained from utilizing m/z = 31 for selectivity and activity calculations. This decision was based on the compromised resolution of the mass spectrometer when the OER initiates above 1.4 V vs. RHE. Consequently, the signal at m/z = 32 leads to an increase in the adjacent m/z values, including m/z = 31 as seen in 4.6. As a result, m/z = 31 is not a reliable indicator in the presence of simultaneous OER progression.

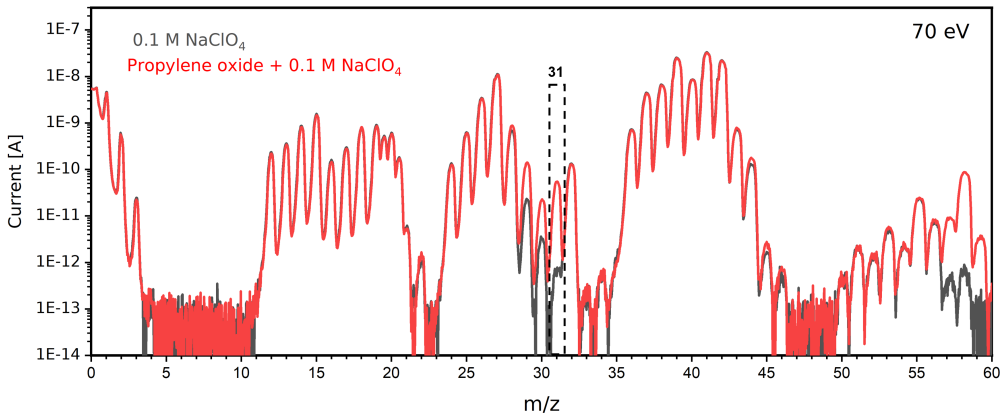

Figure 4.5 Mass spectra of 0.1 M $NaClO_4$ (black) and 0.1 M $NaClO_4$ + PO (red) introduced to EC-MS at 70 eV.

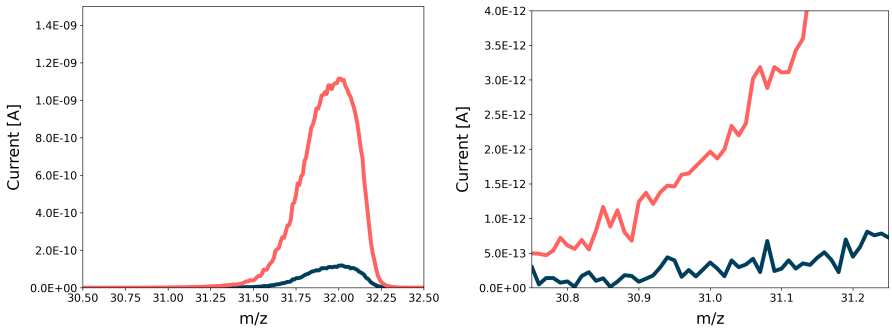

(a) Mass spectra obtained with OER (red) and without OER (blue) at 70 eV showing the increase at m/z = 31.

(b) Closer look to the same mass spectra at the m/z = 31 region showing that the increment in O_2 results in increment in m/z = 31 as well.

Figure 4.6 Mass spectra in the presence and absence of O_2 showing the effect of O_2 on m/z = 31.

4.3 Summary

In summary, detecting PO proves to be a challenging process, despite its significance in understanding the reaction mechanism of electrochemical propylene oxidation. *Ex-situ* product analysis methods, such as HPLC, face various limitations, such as analyte evaporation due to its high volatility, PO hydrolysis leading to propylene glycol formation, and the need for high PO concentrations for reliable detection. To overcome these limitations, I utilized EC-MS, which offered advantages in terms of sensitivity and selectivity.

However, the separation of species with overlapping m/z values in the mass spectra posed a difficulty. Nonetheless, as the experimental conditions rendered acetone and propanal undetectable, I could assign m/z = 58 to PO. Furthermore, the presence of m/z = 31 during the experiments provided supporting evidence for the presence of PO. Despite this, I decided not to include m/z = 31 in the calculations due to potential interference from O_2 and complications above 1.4 V vs. RHE.

Chapter 5

Electrochemical Propylene Epoxidation on PtO_x and PdO_x

In this chapter, I investigated the electrochemical propylene epoxidation reaction on PtO_x and PdO_x electrodes. It is important to note that the catalysts prepared through the drop casting method initially exist in a metallic state. However, as they undergo oxidation during the reaction conditions, and their exact oxidation state becomes unknown, thus they are referred to as PtO_x and PdO_x.

To begin, I employed mass spectrometry cyclic voltammetry to determine the reactivity and identify the relevant potential interval for further study. This approach allowed me to observe not only the oxidation conditions but also the reactions occurring at reductive potentials, providing valuable *in-situ* insights into the surface oxide formation, as mentioned in Section 5.4.

Next, I provided clear definitions of MS-derived selectivity and activity in Section 5.2, aiming to enhance the understanding of interpreting MS data.

Subsequently, I presented the selectivity and activity trends for the electrochemical propylene epoxidation reaction on PtO_x and PdO_x catalysts in Section 5.3. These trends offered valuable insights into the reaction mechanisms, which were further supported by theoretical studies.

Lastly, in Section 5.4, I observed an intriguing phenomenon during the reduction of surface oxide, where the formation of CO_2 served as a useful tool for *in-situ* determina-

tion of the presence of surface oxide with EC-MS. This finding contributes significantly to the field, as previous studies assuming a metallic surface under the same conditions may have led to inaccurate predictions of the reaction mechanisms.

For all the experiments in this chapter, the following experimental conditions were applied:

1 **RE:** Hg/Hg_2SO_4

2 **CE:** Pt wire

3 **Electrolyte:** 0.1 M $HClO_4$

4 **WE:** Pd or Pt drop-casted on a GC substrate

5.1 Determination of the Surface Reactions

In this study, I employed the mass spectrometry cyclic voltammetry (MSCV) method to investigate the reactions occurring on Pt and Pd catalysts over a wide range of potentials during the purging of propylene. The electrodes were polarized within the range of 0.2 - 1.5 V vs. RHE with a scan rate of 5 mVs^{-1}, and I simultaneously observed the MS signals corresponding to C_3H_6, CO_2, O_2, and PO. These signals were represented by mass ion currents denoted as i_{41}, i_{44}, i_{32}, and i_{58}, respectively.

In Figure 5.1a, the cyclic voltammetry results for the Pt catalyst are presented. During the anodic scan, we observe a decrease in the C_3H_6 signal (i_{41}) at $\approx$ 0.7 V vs. RHE, indicating the consumption of C_3H_6 through its oxidation to other species. As the potential is further increased above 1.1 V vs. RHE, the C_3H_6 signal returns to the baseline due to the reduced reaction rate and continuous purging of C_3H_6. Additionally, there is an observed increase in CO_2 (i_{44}) as C_3H_6 undergoes total oxidation to CO_2 at $\approx$ 0.7 V vs. RHE. The rate of CO_2 formation begins to decline in parallel with the decreasing rate of C_3H_6 oxidation. Furthermore, the appearance of O_2 (i_{32}) is observed at approximately 1.45 V vs. RHE due to OER.

On the other hand, Figure 5.1b presents the MSCV data for the Pd electrode. At $\approx$ 0.75 V vs. RHE the C_3H_6 signal starts decreasing, showing C_3H_6 oxidation. Subsequently, O_2 starts increasing at $\approx$ 1.45 V vs. RHE due to the OER. Additionally,

an increase in CO_2 is noticeable starting at ≈ 0.85 V vs. RHE, indicating the complete oxidation of propylene.

Notably, Both Pt and Pd undergo oxidation at potentials above 1.0 V and experience reduction during the cathodic cycles, with PtO_x at 0.7 – 0.9 V vs. RHE and PdO_x at 0.6 – 0.7 V vs. RHE. Interestingly, both for Pt and Pd catalysts, during surface oxide reduction CO_2 formation is observed. This is initially a bit odd, as these potentials are reductive and CO_2 is a complete oxidation product, showing that formation of CO_2 is not due to a Faradaic reaction. Our current understanding suggests that a Potential Induced Non-Faradaic Redox Reaction (PINRR) takes place near the metal oxide/metal redox potentials of Pd and Pt. In this reaction, propylene is oxidized while the metal oxide is reduced. It has been previously observed that PtO_x can be reduced by propylene, wherein it is oxidized to CO_2 using the lattice oxygen, which supports the hypothesis of PINRR in our study [87]. Additionally, Scott et al. have demonstrated a PINRR involving CO and PtO_x, leading to the formation of CO_2 and Pt with EC-MS [88]. Hence, our findings contribute to the broader understanding of this phenomenon.

Based on the PINNR mechanism the following reactions can be described during the surface oxide reductions:

$$PtO_x + C_3H_6 \longrightarrow Pt + 3\,CO_2 + 3\,H_2O \tag{5.1}$$

$$PdO_x + C_3H_6 \longrightarrow Pt + 3\,CO_2 + 3\,H_2O \tag{5.2}$$

As I explained in 3, when using EC-MS, there is a noticeable time delay between the MS signal and the electrochemistry signal due to the mass transport of reaction products.This delay becomes more pronounced when the potential is scanned rather than kept constant. The time response of the species is primarily influenced by their volatility and the diffusion length, as described by Equations 3.8 and 3.9.

The Henry's law constant for volatility for PO, C_3H_6, CO_2, and O_2 are are 20, 21000, 3000, and 83000 $Pam^3\,mol^{-1}$ respectively. Notably, PO exhibits the lowest volatility among these species, which results in a more significant mass transport delay. Therefore, I plotted PO signal during the potential sweep as a function of time to visualize the delay in Figure5.2.

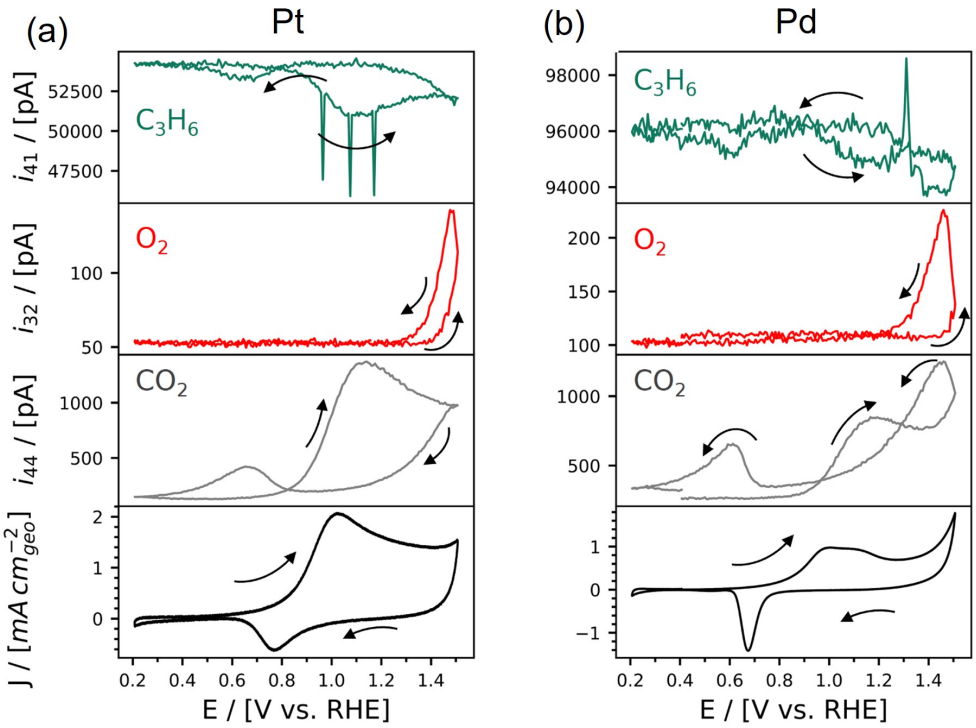

Figure 5.1 MSCV for C_3H_6, O_2, and CO_2 during continuous C_3H_6 purge in 0.1 M $HClO_4$ on (a) Pt and (b) Pd catalysts. CV measurements are conducted by scanning the potential in between 0.2 – 1.5 V vs. RHE, and with a scan rate of 5 mVs^{-1}.

Figure 5.1a presents MSCV on the Pt catalyst. Even though the PO signal rise starts during the anodic cycle as expected, it can only reach to its maximum when the cathodic cycle starts. Furthermore, the signal continues to decay throughout the full potential cycle up to 1.6 V. Despite the relatively slow time response, we can still observe the oxidation of C_3H_6 to PO as the electrode is scanned towards anodic potentials.

In contrast, Pd exhibits a more pronounced mass transport delay in all the MS signals, particularly for PO. Figure 5.2b illustrates that the decay of the propylene signal is minimal during the cathodic cycle due to the sluggish mass transport process, which prevents the signals from returning to baseline values throughout the full potential scan which is also observed in Trimarco's work [71]. This finding is intriguing because the mass transport rate is solely determined by a species' Henry's volatility constant, diffu-

sion constant, and diffusion length, as described by Equations 3.8 and 3.9. Therefore, considering the same EC-MS system with same diffusion length, the mass transport rate for PO should theoretically remain unchanged irrespective of the catalyst material.

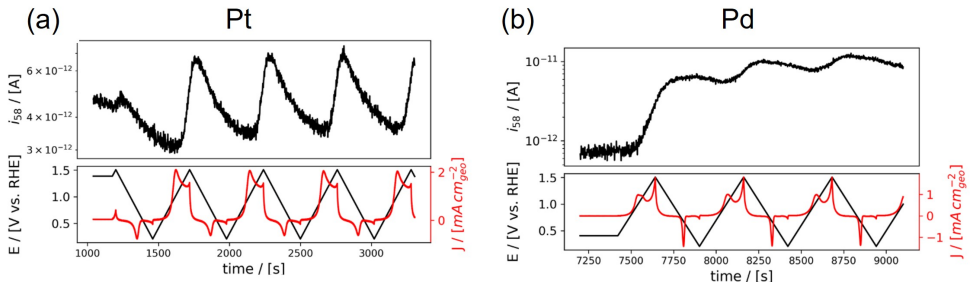

Figure 5.2 MS signal for m/z = 58 assigned to PO is given in the upper panel as a function of time during repeating cyclic voltammetry on (a) Pt and (b) Pd. Potential(black - left axis) and current density (red - right axis) responses given in the bottom panel. The potential range for cyclic voltammetry is 0.2 – 1.5 V vs. RHE, and the scan rate is 5 mVs^{-1}.

One plausible explanation for this behavior could be linked to an increase in the diffusion length specifically for the Pd catalyst. The diffusion length is defined as the distance between the electrode and the membrane chip, which in our experimental setup is 100 μm. During the MSCV experiments, we made an intriguing observation that drop-casted Pd, faces stability issues. Even at relatively slow scan rates, such as 5 $mV\,s^{-1}$, we observed accumulation of catalyst coating (Pd black and Nafion binder) on the membrane chip right underneath the electrode with 5 mm. This could be due the dissolution of Pd at highly anodic potentials and/or mechanical exfoliation due to the gas bubble formation (CO_2 and O_2) during the reaction. This accumulation effectively obstructs the membrane pores at the center, causing an increase in the diffusion length (L) for the species as the direct path is hindered, ultimately leading to slower mass transport and reduced time resolution. This concept is visually depicted in Figure 5.3. Consequently, the observed increase in CO_2 production beyond 1.3 V vs. RHE is likely attributed to the oxidation of the GC substrate, which becomes exposed after the deterioration of the Pd coating. This phenomenon has also been documented in previous EC-MS studies [89].

As depicted in Figure 5.4a, the pores on the membrane chip surface remain open and unobstructed after the experiments involving Pt catalysts. However, in the case of

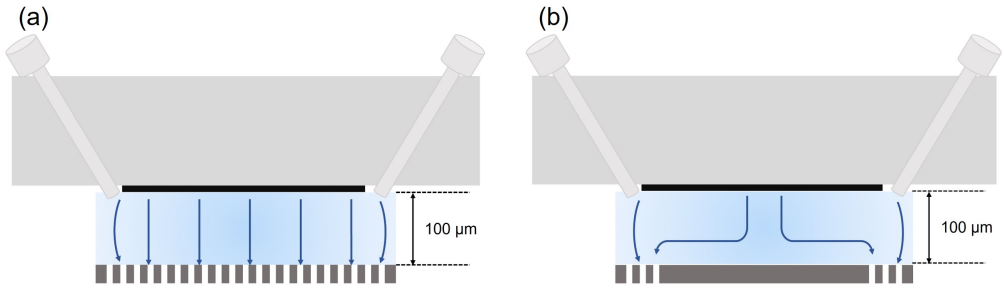

Figure 5.3 Schematic representing the expected transportation of species formed on the WE through the electrolyte and the membrane chip in the case of (a) a clean membrane chip, and (b) a membrane chip with a clogged center.

Pd catalysts, the membrane chip surface is covered with a deposit that contains both Pd and Nafion, serving as a binder. The diameter of this deposit on the membrane matches the electrode's diameter, measuring 5 mm. It's important to note that while this deposit partially covers the 5 mm area, it doesn't completely clog it, as evidenced by the presence of visible heterogeneity in Figure 5.4.

In order to mimic this phenomenon, I conducted experiments with Pt catalysts where I saw no issues regarding clogging. I covered the center of the membrane chip with a 5 mm Kapton tape, as shown in Figure 5.5a. It is worth noting that while the Pd deposit on the membrane chip is not completely impermeable, Kapton tape is. As a result, the effect of mass transport delay becomes more pronounced as there are no species that can utilize the direct 100 μm route for diffusion. Therefore, the outcome of this experiment, presented in Figure 5.5b, reveals a significantly slower time response of species on Pt compared to the results shown in on Pd Figure 5.2b. In the case of Pt with the membrane chip covered by Kapton tape, the mass transfer is sluggish due to the absence of pores right under the electrode. We observe a gradual increase in the PO signal over time, along with a very slow CO_2 formation peak and decay. Moreover, the CO_2 signal fails to reach baseline values during the course of one complete cycle, indicating the presence of slow mass transport.

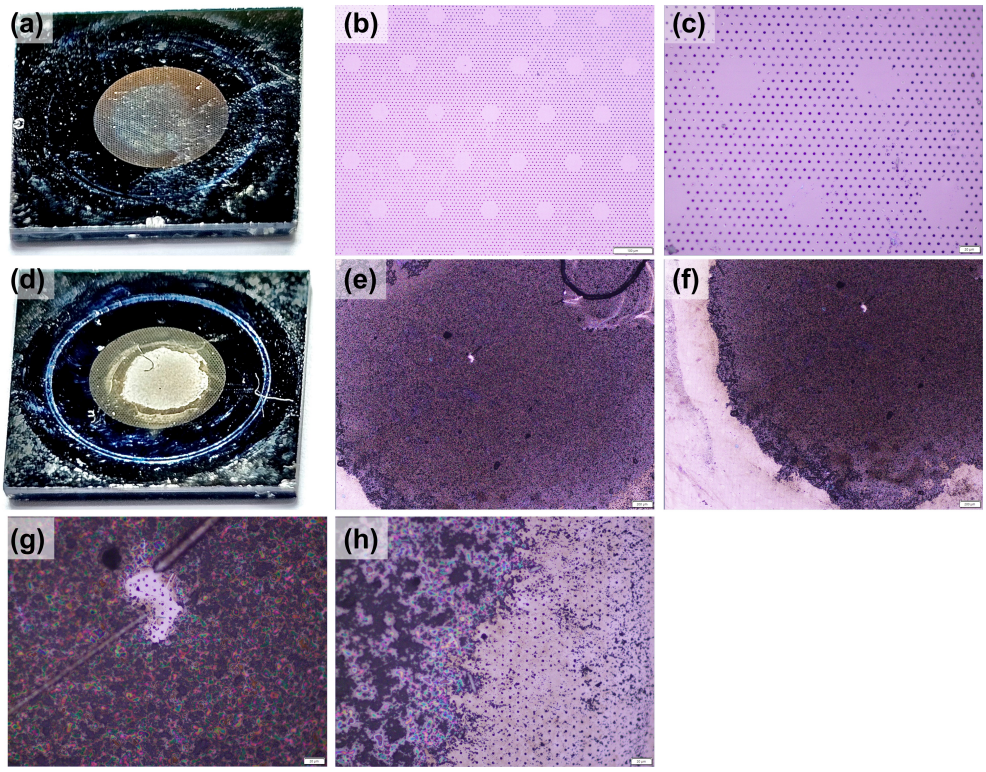

Figure 5.4 Membrane chip coverage with Pd deposit. (a) A photo of clean membrane chip after an experiment with Pt. (b),(c) optical microscopy images of the clean chip after Pt experiments showing that the pores are open. (d) Photo of a membrane chip covered with Pd deposit after an experiment with Pd. (e), (f), (g), (h) optical microscopy images of the membrane chip after the Pd experiment representing the coverage of the membrane chips.

5.2 MS-derived Selectivity and Activity Definitions

Electrocatalytic reactions' selectivity and activity can be effectively evaluated through Faradaic efficiency and partial current density, respectively. The equations for the calculation of Faradaic efficiency (Equation 1.12) and partial current density (Equation 1.13) can be found in Chapter 1. To apply these equations successfully, information regarding the total charge and current imparted during the electrochemical reaction is essential, data that are recorded by the potentiostat.

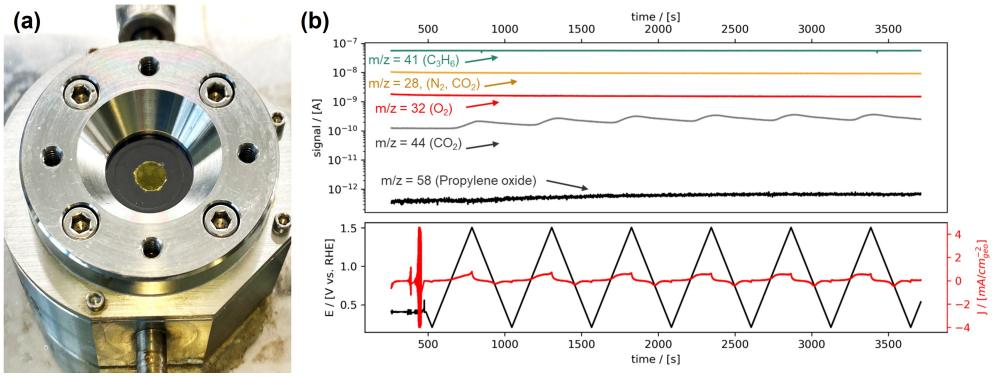

Figure 5.5 Experiment to replicate the clogged membrane effect. (a) Photo of the membrane chip covered with 5 mm diameter kapton tape. (b) MSCV experiment conducted with Pt catalyst between 0.2 - 1.5 V vs. RHE with 5 mVs^{-1} scan rate while purging C_3H_6, representing the retardation in the clear peak formation in the oxidation products with a slight but continuous increase in PO signal, and slight increase in the CO_2 signal with a slower mass transport compared to the case where membrane chip is not covered with a kapton tape.

Furthermore, it is necessary to determine the number of moles of PO (n_{PO}) generated in the reaction. This can be achieved by calibrating the EC-MS. This calibration establishes the relationship between the number of moles of PO and the corresponding EC-MS signal for PO, captured in the following equation:

$$\dot{n_{PO}} = S \times i_{58} \tag{5.3}$$

where, $\dot{n_{PO}}$ is the number of moles flux in mol/second, S is the calibration constant, and i_{58} is the mass ion current obtained at m/z = 58 for PO at EC-MS.

To determine the selectivity and activity trends for electrochemical propylene epoxidation, I employed a methodology based on integrating the mass ion current at m/z = 58 assigned for PO, represented as i_{58}, over the entire duration of the reaction. This integration process yielded the corresponding charge denoted as q_{58}, as indicated in Equation 5.4.

$$q_{58} = \int i_{58} dt \tag{5.4}$$

Therefore the total number of moles could be defined as:

$$n_{PO} = S \times q_{58} \tag{5.5}$$

As a consequence, since the charge q_{58} is always directly proportional to the number of moles of PO n_{PO}, it can be effectively utilized instead of n_{PO} when observing trends in selectivity and activity without the need for calibration and I called these values as MS derived selectivity and activity. As selectivity is defined with Faradaic efficiency, the MS derived selectivity is given in the following equations:

$$FE_{PO} = \frac{n_{PO} \times 2 \times F}{Q} \propto \frac{q_{58}}{Q} \tag{5.6}$$

where FE_{PO} is the Faradaic efficiency towards PO, 2 is the number of electrons need to be transferred to produce PO from propylene, F is Faraday constant, Q is the charge passed during the electrochemical reaction. As the number of electrons transferred and Faraday constant are constants the MS derived selectivity is simplified to $\frac{q_{58}}{Q}$.

Similarly, the activity defined with the partial current density, MS derived activity is given as:

$$J_{PO} = J_{tot} \times FE_{PO} \propto J_{tot} \times \frac{q_{58}}{Q} \tag{5.7}$$

where J_{PO} is the partial current density for PO, J_{tot} is the total current density.

However, it is important to acknowledge that to obtain absolute Faradaic efficiency and partial current density values, calibration of the EC-MS is necessary. In this study, I refrained from calibrating PO due to several challenges. Firstly, calibrating the EC-MS for liquid products is challenging due to continuous evaporation and fluctuations in concentration. Moreover, the time lapse between the preparation of standard solutions and their introduction to the EC-MS led to unstable signals, as PO progressively underwent hydrolysis to propylene glycol, resulting in a decrease in PO concentration over time. This dynamic concentration change is not totally representative at the reaction conditions as PO is continuously generated on the electrode. Additionally, handling carcinogenic chemicals for an extended duration without proper ventilation posed a significant challenge for the calibration of PO in the EC-MS, as the instrument lacked a ventilated fume hood.

5.3 Selectivity and Activity on PtO_x and PdO_x

The utilization of MSCV on Pt and Pd catalysts provided valuable insights into the overall reactions occurring during the propylene purging process in the electrolyte and the associated potential ranges, as illustrated in Figure 5.1. However, another noteworthy observation from Figure 5.2 was the existence of a delay between the MS signal and the electrochemistry signal, which complicated the accurate interpretation of selectivity and activity trends at different potentials. It should be noted that deconvolution of the mass-transport delay is possible, however it would require a complicated post-data analysis [90].

To mitigate this delay and ensure precise monitoring of PO formation without being affected by mass transport issues, we conducted experiments using a constant potential for a duration of 30 minutes. I find this method simpler and more accurate than the deconvolution of the mass-transport effect. This approach allowed us to accurately track PO formation while minimizing any potential time discrepancies in the MS signal. To ensure the reliability of our obtained trends, we set a criterion that the MS signal should be detectable, with a signal intensity higher than three times the standard deviation given in Appendix. To ensure the comparability in between experiments conducted in different times, base peak normalization is employed according to the highest signal m/z=41 belonging to C_3H_6 as it is used as a carrier gas throughout the experiment [91].

As described in Section 5.2, we obtained the selectivity and activity trends. It should be noted that, as the logarithm of partial current density versus potential plots defined as Tafel plots, I named them as MS derived Tafel plots in 5.6a and 5.6b.

Figure 5.6a illustrates that the selectivity towards PO formation continuously increases with higher potentials on PtO_x. While pushing the potential beyond 1.6 V vs. RHE might seem like a straightforward approach to maximize PO selectivity, I encountered a practical limitation. As the potential is further increased, bubble formation leads to a loss of conductivity in the electrochemical cell. This issue commonly occurs in stagnant thin layer cells, preventing me from exploring higher anodic potentials.

On the other hand, in Figure 5.6c, we observe that on the PdO_x catalyst, PO selectivity reaches its peak at 1.3 V vs. RHE, decreasing beyond this point. A study conducted by Li et al. employing DFT calculations revealed that oxygen vacancies are

likely to form on the PdO_x (110) surface above 1.23 V vs. RHE, leading to propylene's reactivity with the lattice oxygen. Additionally, at these potentials, a highly competitive dehydrogenation process of $-CH_3$ through lattice oxygen promotion occurs with a low barrier of 0.07 eV, contributing to the decline in PO selectivity above 1.3 V vs. RHE, coupled with the occurrence of the oxygen evolution reaction at more positive potentials [1].

The MS-derived Tafel plots for PtO_x and PdO_x can be observed in Figure 5.6b and 5.6d, respectively. In the case of PtO_x, the logarithm of the partial current density for PO formation ($log(J_{PO})$) exhibits a linear increase with the potential. Remarkably, this behavior aligns well with previous DFT calculations that proposed PtO_2 (110) to be situated at the top of the volcano curve with maximum activity around 1.6 V vs. RHE [1]. The agreement between our experimental results and the DFT predictions at 1.6 V further supports the notion that the rate-determining step for PO formation remains unchanged within this potential range. The consistency in the MS-derived Tafel slope strengthens this conclusion.

For PdO_x given in Figure 5.6d, the activity also increases with increasing potential, yet two distinct slopes are observed at different potential intervals: 1.0 – 1.3 V vs. RHE and 1.4 – 1.6 V vs. RHE. This change in slope signifies that the rate-determining step of the reaction alters [92]. Prior studies have suggested that the reaction mechanism shifts due to the formation of lattice oxygen on the PdO_2 (110) surface, which reacts with propylene, based on DFT calculations [1].

During this PhD project, I had a chance to collaborate with Christina Susan Abraham. She contributed to this work with DFT calculations. She provided important outcomes that is related to these experiments that would help us understand the mechanism further. I cannot provide the data for the following comments as they are in the preparation processes, however I can provide a glimpse of the findings. First of all, as a result of the DFT calculations it is found that Langmuir-Hinselwood mechanism is prominent over Mars-Van Krevelen at 1.1 -1.3 V vs. RHE range on PdO surface. It is found that propylene epoxidation starts with the vinylic adsorption of propylene to the surface, which subsequently reacts with *OH or *O. Even though the thermodynamic potentials for propanal and acetone formation are lower than the PO formation,

the kinetic barrier calculations revealed that the activation energy for PO (0.3 eV) is significantly lower than for acetone (1.3 eV) and propanal (1.2 eV).

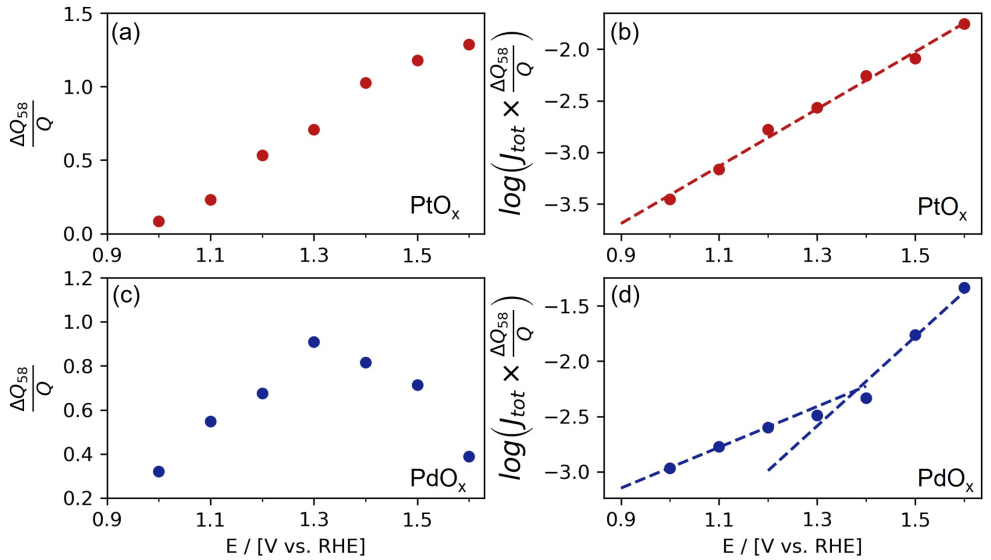

Figure 5.6 The MS-derived selectivity trends for (a) PtO_x and (c) PdO_x for PO, and MS-derived Tafel plots for (b) PtO_x and (d) PdO_x depending on the potential during 30 minutes of chronoamperometry experiments in 0.1 M $HClO_4$ while continuously purging C_3H_6 is given. See the text for details of the derivations.

The MS-derived selectivity trends for PO, along with the MS-derived Tafel plots, were confirmed through 5-minute chronoamperometry experiments. These chronoamperometry experiments showed consistent selectivity trends with a continuous increase in selectivity towards PO (Figure 5.7a) and a linearly increasing activity with higher oxidative potentials (Figure 5.7b) on PtO_x catalysts.

For PdO_x catalysts, the selectivity for PO reached its peak at 1.3 V vs. RHE as given in Figure5.7c, same as the 30-minutes chronoamperometry experiments. While the MS-derived Tafel plot given in Figure5.7d appears to show a change in slope at 1.3 V, it is important to note that I could not explore more anodic potentials beyond 1.5 V vs. RHE due to bubble formation. As such, it is not appropriate to deduce conclusions based on only two data points, so I refrain from making strong assumptions about the slope change.

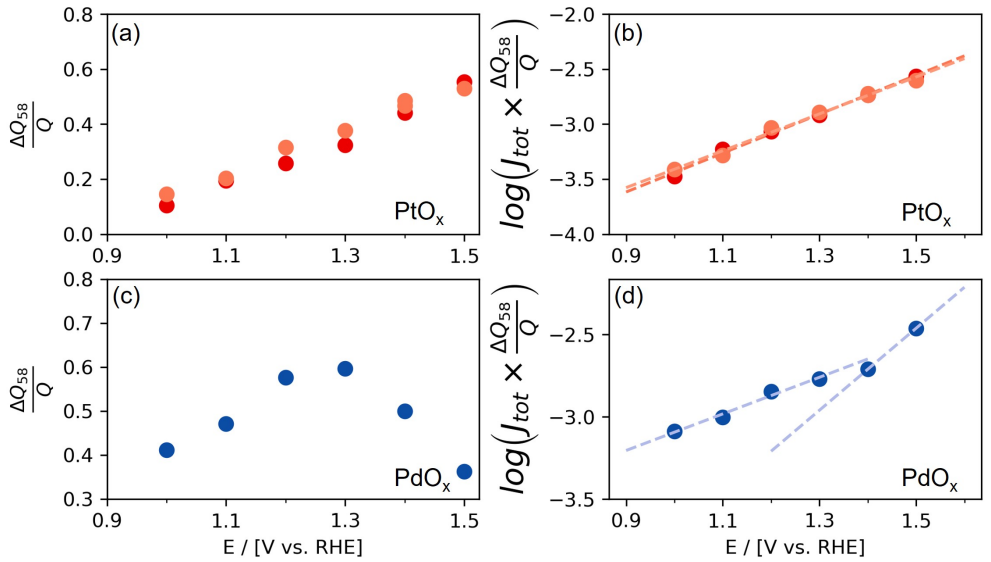

Figure 5.7 (a) MS-derived PO selectivity trends for PtO_x, (b) MS-derived Tafel plot for PtO_x are given. Different shades of data points represents different experiments. (c) MS-derived PO selectivity trend for PdO_x, and (d) MS-derived Tafel plot for PtO_x are shown depending on the potential. All the experiments are conducted for 5 minutes in 0.1 M $HClO_4$ while continuously purging C_3H_6, showing the same trends with 30 minutes experiments.

In conclusion, through the utilization of EC-MS, I successfully determined the selectivity and activity trends for the electrochemical propylene epoxidation reaction. The obtained experimental data revealed the potential regions where peak selectivity occurs and unveiled the variations in activity corresponding to different potentials for both PtO_x and PdO_x. Remarkably, these experimental findings closely match the theoretical predictions made by Li et al. [1], thereby providing strong support for the proposed reaction mechanisms on these catalysts.

5.4 *In-situ* Determination of Surface Oxide

The oxidation state of a catalyst's surface plays a critical role in determining its catalytic activity. Therefore, it is crucial to assess the surface under reaction conditions to gain more accurate insights into the reaction mechanisms. However, performing such assessments presents challenges for several reasons. Firstly, once the catalyst is removed

from the reaction conditions, its oxidation state may change. For instance, catalysts like Pt and Pd exist in a metallic state in the ambient environment. Conducting *ex-situ* surface characterization of these catalysts after the reaction may not provide accurate information about their actual surface oxidation state during the reaction. To address this issue, researchers can employ *operando* characterization techniques, which allow for the assessment of catalyst surfaces under realistic reaction conditions. These techniques provide valuable information about the catalyst's oxidation state and its dynamic changes during the reaction. However, accessing *operando* surface characterization facilities can be limited, as there are only a few such specialized facilities worldwide. Moreover, the demand for *operando* experiments is high, making it challenging for researchers to conduct these experiments at all times.

However, during the experiments I realized an interesting phenomena which could provide information about the surface oxidation state of the catalyst during the reaction conditions. As seen in Figure 5.8 during the chronoamperometry experiments, I applied a constant potential while purging C_3H_6 at a double layer potential to avoid any Faradaic reactions. It should be noted that at double layer potential (0.4 V vs. RHE) both Pt and Pd are in metallic state. Subsequently, I raised the potential to a test potential, which promotes the oxidative process of propylene oxidation. As a result, as depicted in Figure 5.8, CO_2 is generated through the complete oxidation of C_3H_6. Interestingly, when I returned the potential back to the double layer potential, another increase in CO_2 formation was observed, indicated by the red highlight on the gray line in Figure 5.8.

Since the applied potential (double-layer potential) was not oxidative, and only reductive Faradaic reactions are expected at this potential, the presence of this additional CO_2 generation raised questions. In Section 5.1, the simultaneous CO_2 formation during the surface oxide reduction was observed. Therefore, it was deduced that this CO_2 production is a result of the reduction of the surface oxide, as described in Equations 5.8 and 5.9. This finding has significant implications as it provides valuable information about the surface oxidation state of the catalyst during the electrochemical propylene oxidation reaction.

$$PtO_x + C_3H_6 \rightarrow Pt + 3CO_2 + 3H_2O \tag{5.8}$$

$$PdO_x + C_3H_6 \rightarrow Pd + 3CO_2 + 3H_2O \tag{5.9}$$

In Figure 5.8, I omitted the sections between potentials where the electrolyte was exchanged and long waiting times that were not informative, with the aim of ensuring a clear and unambiguous data representation. Notably, the data clearly indicates the presence of surface oxide for both PtO_x (Figure 5.8a) and PdO_x (Figure 5.8b) catalysts within the potential range of 1.0 V to 1.6 V vs. RHE. Furthermore, it is seen that the CO_2 peak due to the surface oxide reduction, highlighted in red, becomes more prominent as the potential increases. This indicates an increase in the amount of surface oxide, suggesting a direct correlation between the potential and the surface oxide formation.

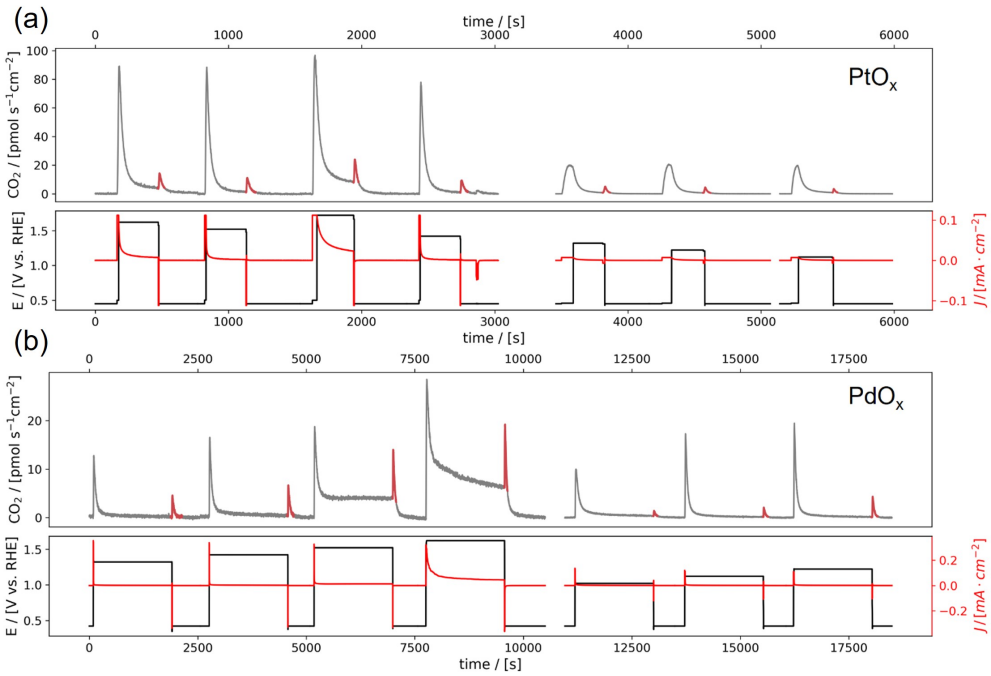

Figure 5.8 Chronoamperometry experiments on (a)PtO_x and (b) PdO_x showing the increase in CO_2 signal (upper panel) due to C_3H_6 oxidation (black) and surface oxide reduction (indicated with red).

Furthermore, another observation is that at 0.9 V vs. RHE, the CO_2 formation resulting from surface oxide reduction during the switch from oxidative potential to double-layer potential is not observed in Figure 5.9a for Pd and Figure 5.9b for Pt

catalysts. This absence of CO_2 production at 0.9 V vs. RHE indicates that the surface of both catalysts remains in the metallic state at this potential.

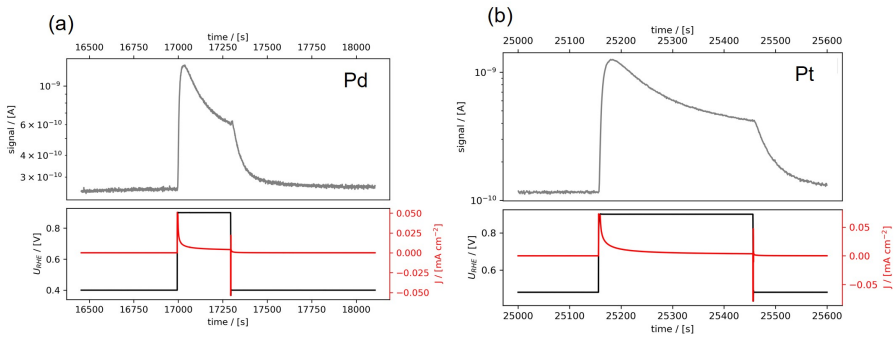

Figure 5.9 On (a)Pd and (b) Pt increase in CO_2 signal (upper panel) due to C_3H_6 oxidation is seen and the absence of increase in the CO_2 signal while switching from 0.9 V vs. RHE to resting potential showing the absence of surface oxide at this potential is given.

In Figure 5.10, we observe the increase in CO_2 formation per catalyst area resulting from the reduction of surface oxide, depending on the applied oxidative potential. Both for PdO_x and PtO_x catalysts, it is evident that the CO_2 production due to surface oxide reduction exhibits a linear relationship with the increasing potential. However, the slope of the line is larger for PdO_x, indicating a more pronounced effect of the potential compared to PtO_x. This can be attributed to the higher oxygen affinity of PdO_x, which is expected to promote more oxidation compared to PtO_x.

Notably, the observed amount of CO_2 is higher on PdO_x than on PtO_x, which might suggest a higher amount of surface oxide. Nevertheless, it is essential to be cautious when directly correlating the oxide amount with the formed CO_2. The amount of CO_2 formed is influenced not only by the quantity of oxide present but also by factors such as the surface coverage of C_3H_6 and the ratio of reduced surface oxide involved in the CO_2 formation reaction, which remain unknown. Therefore, in this study, I refrained from directly comparing the oxide amounts on different catalysts to avoid misinterpretations.

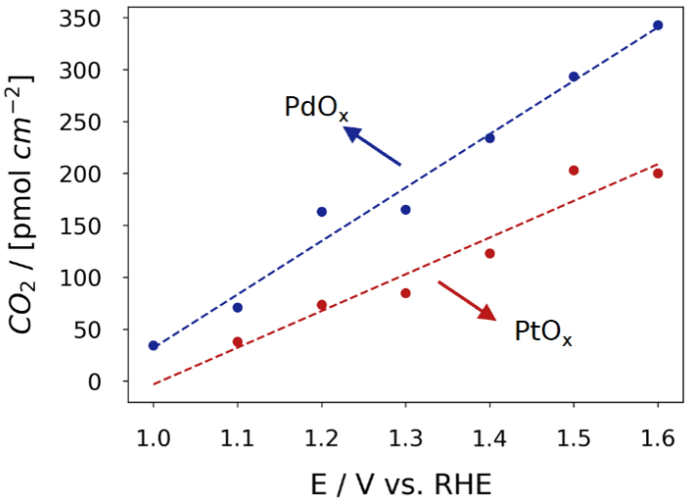

Figure 5.10 CO_2 amount formed due to the surface oxide reduction after each potential is given on PtO_x (red) and PdO_x (blue) showing a linear relationship with the potential increase.

5.5 Summary

Previously, I determined the relevant potential intervals for propylene oxidation in addition to the observation of the overall reactions including the anodic and cathodic potential regime with MSCV method. As a result, the CO_2 formation simultaneous with the oxide surface reduction on both Pt and Pd catalysts is observed, which is used for the *in-situ* surface oxide detection in Section 5.4. However, with this method the accurate information about the selectivity and activity at a certain potential could not get as the MS signal is delayed due to the mass transportation of the reaction products.

Therefore, in this chapter I used chronoamperometry method to obtain the selectivity and activity trends on PtO_x and PdO_x catalysts to avoid the mass transport limitation. Due to the limitations of being able to do the calibration for PO, I used the MS derivations of Faradaic efficiency for the selectivity and partial current density for the activity trends as defined in Section 5.2.

According to the selectivity and activity trends described in 5.3, it is found that the selectivity and activity for PO constantly increasing with an increasing anodic potential on PtO_x catalyst. On the other hand, for the PdO_x catalyst, the selectivity for PO peaks at 1.3 V and the slope of the MS-derived Tafel slope changes at the same potential

showing that the change in reaction mechanism. These results were confirmed the previous theoretical studies.

Finally, with the formation of CO_2 during the surface oxide reduction, I was able to detect if there is an oxide formation at the reaction potentials *in-situ* with EC-MS. The results showed that, the surface oxide formation starting from the 1.0 V vs. RHE on Pt and Pd catalysts.

In conclusion, this chapter has yielded significant findings that shed light on misconceptions in the literature regarding the direct oxidation of propylene to propylene glycol without considering the intermediate formation of PO. By successfully detecting PO and studying the selectivity and activity trends, I have emphasized the importance of thoroughly investigating the PO formation in the electrochemical propylene oxidation reaction.

Furthermore, this study has revealed the significance of considering the oxidation state of the catalyst surface during the reaction. The experimental evidence presented here confirms that the assumption of a metallic surface at highly anodic potentials can lead to errors for the calculations of reaction mechanisms. For instance, a previous study [26] claimed direct propylene oxidation to propylene glycol by using *ex-situ* product analysis method NMR. Also, the propylene oxidation to propylene glycol mechanism is compared on metallic Pd and PdO catalysts at a potential range of 0.7 to 1.4 V vs. RHE with ATR-FTIR and the results are supported with DFT calculations. However, this study overlooked the fact that Pd is oxidized at potentials more anodic than 0.9 V, and metallic Pd was assumed even at 1.4 V vs. RHE. Such oversights can result in misinterpretations of reaction mechanisms.

The results presented in this chapter underscore the importance of considering the surface oxidation state and detecting reaction products accurately, especially in reactions like propylene oxidation, where the products are not stable. This knowledge contributes significantly to the understanding of complex electrochemical reactions and highlights the necessity of comprehensive experimental investigations to support theoretical calculations.

Chapter 6

Chlorine Evolution Reaction: Catalyst screening with EC-MS

This chapter involves the chlorine evolution reaction project that is conducted in Spectro Inlets, ApS during my 3 months of external stay. The initial aim of this project was comparing the overpotentials of different catalysts in the same study with same conditions with a sensitive method being EC-MS. In the literature, there is no volcano plot based on the CER overpotential obtained for different catalysts to the best of our knowledge. The OER overpotential is used to establish the volcano plots [93], as there is a linear scaling relationship between CER and OER as explained in Chapter 2 in detail. However, the linearity between OER and CER becomes invalid if there is a catalyst using a different active site than oxygen. As mentioned in Chapter 2 some studies showed that metallic Pt is exceptional as the reaction mechanism does not follow the path through Pt-OCl but Pt-Cl. Therefore, it is significant to test all the catalysts' overpotential for CER experimentally and being aware of the surface oxidation state.

For this study, EC-MS provides significant advantages for CER investigation. As the collection efficiency is 100%, it enables the detection of very small quantities of Cl_2 and provides great sensitivity for highly volatile molecules. Secondly, it facilitates the track of Cl_2 signal in real-time and observe the changes over time. Thirdly, it allows easy quantification of produced Cl_2 as due to its 100% collection efficiency.

In this chapter, insights about experimental methods and considerations specific to CER with EC-MS are given at the beginning. Thereafter, comparisons of different catalysts' activity is presented. Finally, the lack of clarity about the definition of CER overpotential in the literature is addressed and real-time equilibrium potential determination method with EC-MS is introduced.

6.1 Experimental Methods

6.1.1 Experimental protocol

For all CER experiments in this chapter, the following experimental conditions were applied:

1 **RE:** Hg/Hg_2SO_4

2 **CE:** Pt wire

3 **Electrolyte:** 0.1 M $HClO_4$ + 1 M NaCl prepared and $HClO_4$ dropped until pH<1 is obtained. The final pH was 0.96 which is measured with an electronic pH meter. pH below 1 is aimed to avoid Cl_2 hydrolysis.

4 **WE:** Prepared catalysts in the form of stubs or sputtered on GC substrate or titanium substrate.

The experimental protocol used to assess the performance of the CER catalysts is presented in Figure 6.1a. The procedure involves several steps to gather data about the reactions occurring within a potential range. The first step is to conduct CV, which provides an overall understanding of the reactions happening at various potentials. This helps identify the double-layer potential, where no Faradaic reactions take place on the electrode for the further ohmic resistance measurement. Subsequently, the ohmic resistance is determined using EIS. The obtained resistance value is then compensated by 85% using software. In the third step, CV is performed again to test different potentials. The potential is swept from 1.2 V vs. SHE to the designated test potential at a scan rate of 5 $mV\,s^{-1}$ to prevent double-layer charging caused by abrupt potential changes. The potential is then held at the test potential for 5 minutes. Afterwards,

the potential is swept back to 1.2 V vs. SHE, and the system is allowed to stabilize until all the MS signals return to their baseline values. The resting potential is chosen carefully, considering two main criteria: (i) it should be as anodic as possible to avoid double-layer charging during the scan to more anodic potentials, and (ii) it should be lower than the onset potential of the OER or CER to avoid interference with the MS signals.

The test method is demonstrated on a Pt stub in Figure 6.1b. This experimental approach ensures a systematic and reliable evaluation of the catalyst's performance under controlled conditions.

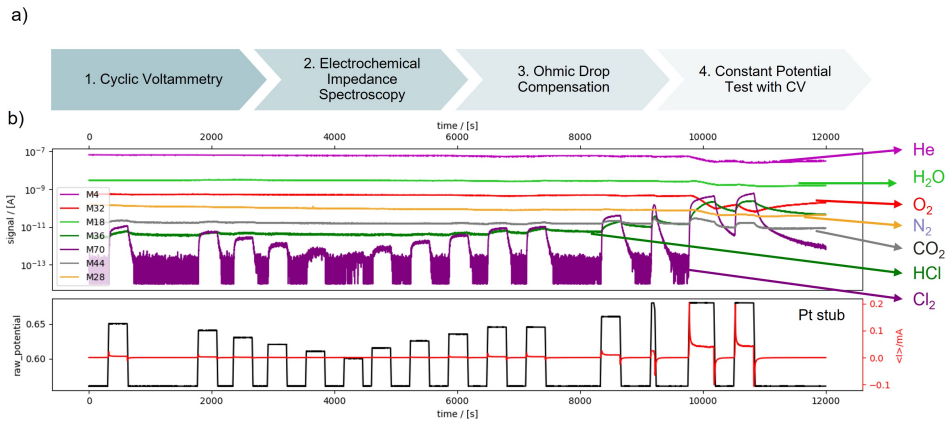

Figure 6.1 (a)Experimental protocol used for CER performance evaluation for different catalysts. (b) Representation of the constant potential test with CV on Pt stub in the mass spectrum.

In this study, various catalysts were evaluated using different electrode configurations as shown in Figure 6.2. All the electrodes are cylindrical with 5 mm diameter to fit the u-cup assembly of EC-MS cell. The stub electrodes are consist of the catalyst material as a bulk (Figure 6.2a). On the other hand, the sputtered samples are catalyst layers coated onto the substrates (Figure 6.2b). Despite being a coating, the thickness of the catalyst layer was always maintained above 20 nm to ensure that the bulk properties of the catalysts were preserved. Additionally, there is a different catalyst prepared using ALD, which involves depositing a 2 nm TiO_2 layer on top of a 20 nm Pt layer and indicated as TiO_2/Pt on GC for the rest of the thesis (Figure 6.2c). GC is used as a substrate, and 5 nm Ti layer served as an adhesion layer. Originally, this sample was

intended for the propylene oxidation project to weaken the binding energy of propylene to the Pt surface through the very thin TiO_2 layer and increasing the activity towards PO. However, due to time constraints, this specific sample was not tested for the propylene oxidation project. Nevertheless, it was decided to evaluate this catalyst for the current CER project as it could show the tuning effect for CER as well as described in Chapter 2 for different catalysts. By employing different electrode configurations, this study aimed to gain insights into the catalytic properties and performance of the various catalysts.

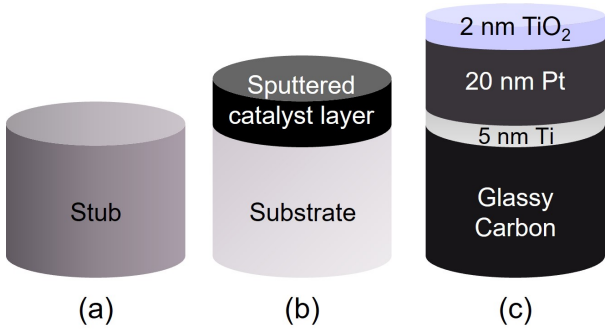

Figure 6.2 Electrode configurations used in the CER study: (a) stub, (b) sputtered film on a substrate, (c) the sample prepared with ALD.

6.1.2 Chlorine Calibration

To quantify the amount of Cl_2 produced by each catalysts at each potential I calibrated the EC-MS for Cl_2. In EC-MS, there are 2 types of calibration methods could be employed defined as internal and external calibration which are described in detail in Daniel Trimarco's thesis [77].

1 **Internal calibration:** This method relies on the assumption of 100% Faradaic efficiency for the reactions. By measuring the amount of charge passed during the electrochemical reaction, the number of moles of the analyte can be back-calculated via Faraday's law given in Equation1.11. Internal calibration is suitable for specific reactions where 100% Faradaic efficiency can be assumed, such as the hydrogen evolution reaction, OER, or carbon monoxide oxidation to carbon

dioxide. In the current study, this method was used for the CER, where there is no OER present. Internal calibration is a straightforward and rapid method for EC-MS calibration. However, it does have its limitations. The assumption of 100% Faradaic efficiency might overlook side reactions that could occur, such as catalyst dissolution, substrate oxidation, or reactions caused by contamination. To minimize these issues, it is crucial to use a stable electrode under the reaction conditions and verify the MS signal for any substrate oxidation products (e.g., CO_2 for GC) to ensure reliable results.

2 **External calibration:** In this method, a standard gas mixture containing known concentrations of the analyte is introduced to the EC-MS system, and the MS signal is monitored. External calibration is more accurate compared to internal calibration as it does not require to make the same assumptions. However, it relies on having access to standard gas mixtures of known concentrations.

For the CER study, I tried to calibrate the EC-MS using the external calibration method. However, the maximum concentration of Cl_2 gas mixture available in the market was limited to 100 ppm due to safety concerns. Unfortunately, when I introduced 100 ppm Cl_2 gas mixture to the EC-MS, it was not detectable. As a result, the I employed the internal calibration method for the CER experiments to obtain reliable data for further analysis. I always used IrO_2 on Ti substrate, as IrO_2 is a relatively stable compound under the reaction conditions and Ti is more stable substrate than GC as GC oxidizes to CO_2 at potentials around 1.3 V vs. RHE as shown in Chapter 5.

For the calibration, I applied at least 3 constant currents in between 1-15 μA and monitor m/z = 70 signal corresponding to Cl_2 until the m/z = 70 signal gets stable. Thereafter, at the stable region I selected a time period usually less than 120 seconds and calculated the charge. As there is a linear relationship between the MS signal (S_{MS}) and the molar flux ($\dot{n}$), the calibration constant (F_{cal}) can be calculated with the following equation:

$$F_{cal} = \frac{\bar{S_{MS}}}{\bar{\dot{n}}} \tag{6.1}$$

where $\bar{S_{MS}}$ is averaged MS signal for m/z = 70 and $\bar{\dot{n}}$ is averaged molar flux for Cl_2.

To ensure the highest precision, the internal calibration is performed on the same day as each experiment. An example for the calibration experiment is given in Figure

6.3. In this experiment, I tried increasing the current without waiting Cl_2 signal to go back to baseline and apply the same currents and waited until the Cl_2 signal goes back to baseline value, and did not observe a difference in the F_{cal} for both cases. As a result of this experiment, the plot depicting the integrated MS signal versus the amount of Cl_2 is plotted in Figure 6.4. Finally, F_{cal} is obtained from the slope of this plot based on Equation 6.1.

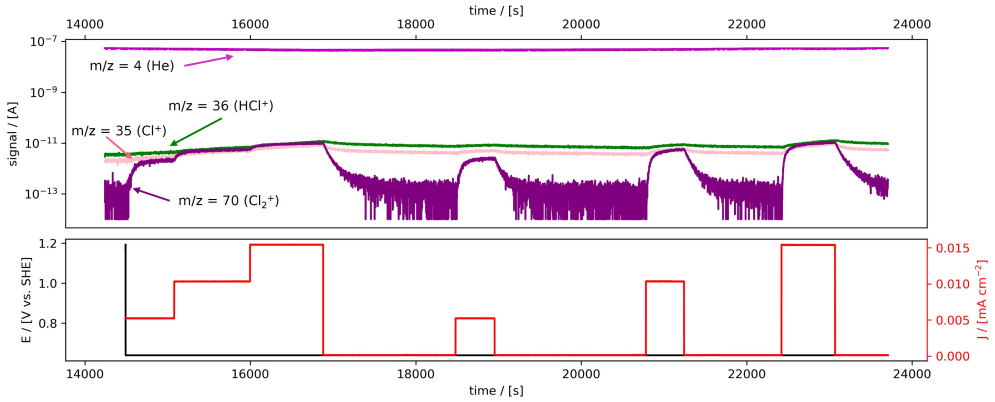

Figure 6.3 Internal calibration of Cl_2 involving the application of constant current and obtaining stable m/z=70.

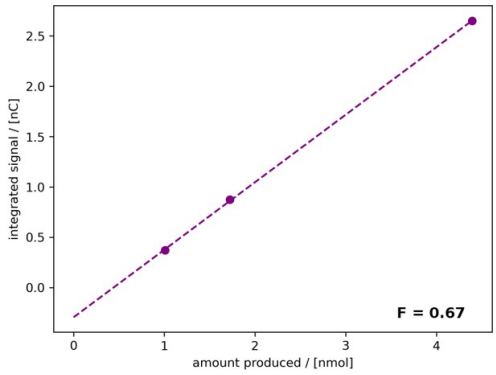

Figure 6.4 Determination of the calibration constant with the slope of the S_{MS}^{-} versus $\bar{n}$.

6.1.3 Detection Potential

Detection potential term is used to define the lowest potential at which Cl_2 is detectable with the EC-MS. I intentionally avoided using the "onset potential" term for the detection potential as there is a lack of universal definition of onset potential. Extensive research on 79 papers published since 2020 reveals that there are three main categories of defining the onset potential: (i) the ones using a threshold current density value, (ii) the ones that are not using a threshold current density value but using the first potential where the reaction product could be detected or extrapolating the current density at higher potentials to zero, and (iii) the others including definition based on thermodynamic, or open circuit potential for membrane electrode assemblies. However, each of these methods has its limitations and disadvantages. For instance, some methods are sensitive to hydrodynamic conditions, while others depend on the data range used or the sensitivity of the product analysis methods [94]. The second onset potential term described is the equivalent of the detection potential in this study.

It is important to note that the surface area of the electrodes are detrimental for this definition. In this research, I have tested electrodes prepared with magnetron sputtering on mirror-polished substrates, ensuring that the surface area of each electrode remained nearly identical. To validate this, I conducted ECSA measurements for Pt on Ti sample using CO stripping. The ECSA closely matched the geometrical surface area, with 0.193 and 0.196 cm^2, respectively. Nonetheless, for a better precision, individual ECSA measurements for each sample would be ideal.

The limit of detection (LOD) of a species with an analytical tool is well-defined statistically [95]. In Equation 6.2 the LOD definition is written for the EC-MS.

$$S_a - S_n \geq 3 \times \sigma_n \tag{6.2}$$

where S_a is the MS signal produced by the analyte, S_n is the background signal when there is no analyte present, σ_n is the standard deviation of the background signals' noise. In conclusion, the potential that can produce a Cl_2 signal which is three times the standard deviation of the Cl_2 noise signal, is called the detection potential.

6.1.4 m/z = 36 Signal Source and Effects

In the initial stages of this study, I referred to the NIST (National Institute of Standards and Technology) database to obtain the mass spectrum of Cl_2 and identify the expected signals at specific m/z ratios [86]. Figure 6.5 displays the anticipated m/z ratios, while Table 6.1 provides information about the ionized species corresponding to these m/z values.

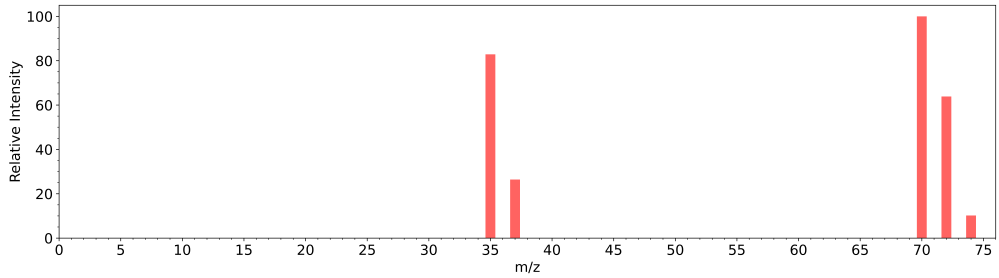

Figure 6.5 Mass spectrum of Cl_2 at 70 eV ionization energy. Data retrieved from [86].

Table 6.1 Ionized species belonging to Cl_2 at 70 eV ionization energy and the corresponding mass-to-charge ratios.

m/z	Ionized Species
35	$[^{35}Cl]^+$
37	$[^{37}Cl]^+$
70	$[^{35}Cl^{35}Cl]^+$
72	$[^{35}Cl^{37}Cl]^+$
74	$[^{37}Cl^{37}Cl]^+$

In the literature there are number of studies reported a signal increase at m/z = 36 during the CER experiments. Even though this is not a fragment of Cl_2 itself, it is attributed to the formation of $[H^{35}Cl]^+$ in the MS due to combination of ^{35}Cl from the fragmentation of Cl_2 and H from the fragmentation of water [50, 51]. On the other hand, another study attributed this increase to the formation of hydrochloric acid due to the reaction of Cl_2 with water in the electrolyte [37]. However, at pH 0.96, formation of HCl is not likely, and Cl_2 being the main species small amount of hypochlorous acid (HOCl) is expected according to Figure 2.2. As HOCl is a highly non-volatile

compound with Henry's law constant for volatility of 0.16 $Pa\,m^3\,mol^{-1}$ [81], it is not expected to be detected by EC-MS.

Initially, during the EC-MS experiments, I did not observe any increase in the m/z = 36 signal. I hypothesized that the formation of $[H^{35}Cl]^+$, which requires water fragmentation in the MS, might be hindered by the limited transport of water to the MS through the membrane chip. This limitation is different from DEMS, where a differential pump allows a greater amount of water to be transported to the MS. Thus, the very low amount of water in the MS could result in an undetectable level of $[H^{35}Cl]^+$ formation. However, this initial idea raised suspicion because, as shown in Figure 6.6, the baseline signal of m/z = 36 was remarkably high being $\approx 10^{-10}$.

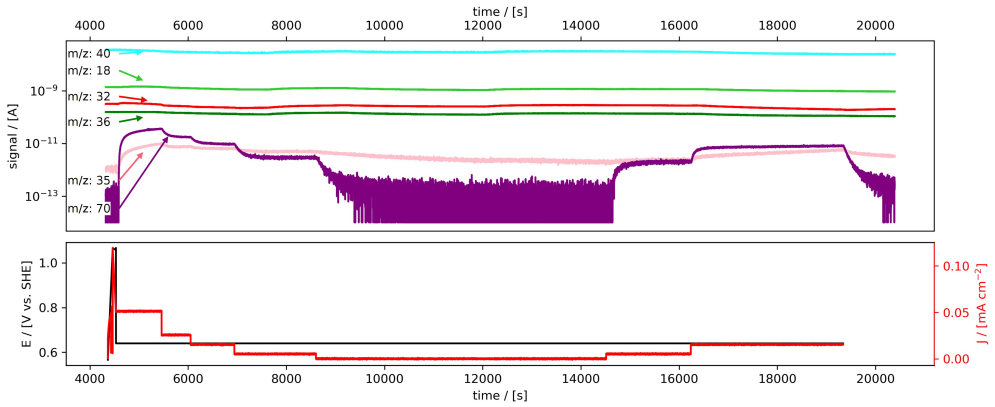

Figure 6.6 Absence of increase in m/z = 36 signal during the production of Cl_2 while using Ar as a carrier gas.

Further investigation revealed that Ar, which I introduced as a carrier gas, has an isotope ^{36}Ar as seen in Figure 6.7. Although its abundance is only 0.334%, it strongly affects the m/z = 36 signal due to the large amount of Ar given to the EC-MS. ^{36}Ar dominates the observed signal. This explains the origin of the high baseline signal and the absence of a distinct signal related to $[H^{35}Cl]^+$ in the EC-MS experiments.

To avoid the formation of $[H^{35}Cl]^+$ we attempted to employ soft ionization. Soft ionization is a technique based on the application of lower ionization energies than 70 eV where most of the molecules have their maximum ionization cross section. By application of lower ionization energies preserving the intact ion and avoiding fragmentation is aimed [96].

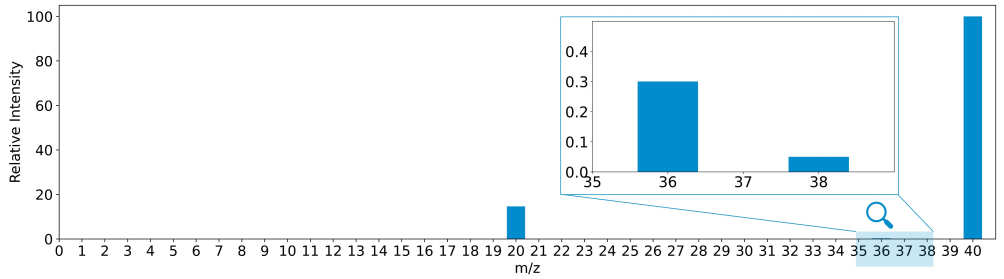

Figure 6.7 Mass spectrum of Argon at 70 eV ionization energy. Data retrieved from [86].

In order to prevent the fragmentation of Cl_2 into Cl, and subsequent recombination of Cl with H to form HCl, we chose to use an ionization energy of 22 eV instead of 70 eV. However, as shown in Figure 6.8, even with the lower ionization energy, there is still enough energy for the fragmentation of Cl_2 and the subsequent formation of HCl. Moreover, decreasing the ionization energy led to a decrease in the MS signal intensity, adversely affecting the sensitivity of the EC-MS. Therefore, after careful consideration, we opted to revert to using 70 eV ionization energy, soft ionization did not effectively prevent HCl formation, but only compromised the sensitivity of the EC-MS. Furthermore, the presence of HCl does not impact the quantification of Cl_2, as the primary formation involves Cl_2 initially, with only a portion of Cl_2 undergoing fragmentation to form Cl and subsequently HCl. As a result, the quantity of HCl formed towards the end of the process does not influence the initial portion of Cl_2 that remains unfragmented.

In conclusion, even though formed HCl does not have a direct effect on Cl_2 signal, as excessive amount of HCl formation can cause other complications we wanted to be able to monitor the changes in m/z = 36 as well. Therefore, we decided to change the carrier gas to He with m/z = 4. As a result, the changes in the m/z = 36 due to Cl_2 production was observable given in Figure 6.9. It should be noted that, the signal decay of the HCl is slower than Cl_2 sourced signals (m/z = 35, 37, 70, 72, 74). As HCl forms in the MS chamber, this issue cannot be a matter of mass transport from the electrode surface to the MS chamber. In my opinion, the issue is that pumping out HCl from the MS chamber is more difficult than pumping out other species.

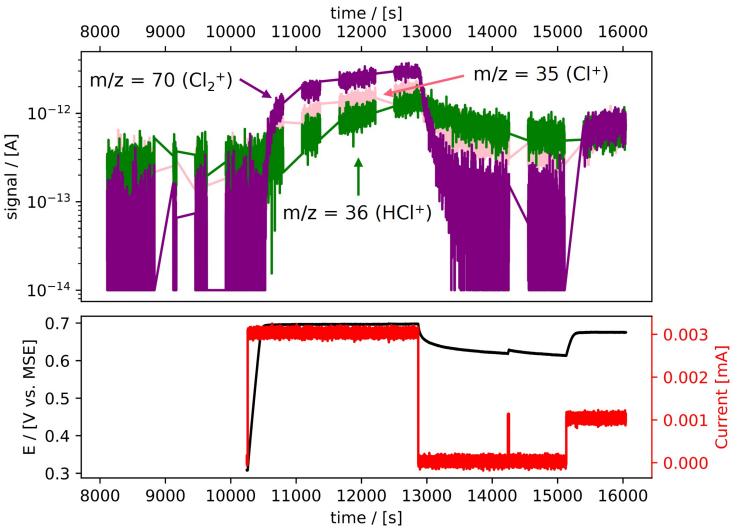

Figure 6.8 Soft ionization trial at 22 eV. Increase in m/z = 36 signal together with increase in m/z = 70 and m/z = 35 signals is seen while using Helium as a carrier gas. The straight lines in the MS signal is because of that at those times I did full mass scan analysis, therefore the data that is not recorded is connected with a straight line.

Furthermore, as shown in Figure 6.9, during the time range of 9500 - 12000 seconds, at more anodic potentials where Cl_2 production is higher, the Cl_2 signal becomes dominant, making it harder to observe changes in the other species. For instance at high Cl_2 production ranges, the decrease in the O_2 signal could hinder the accurate observation of small amounts of O_2. To address this issue, I avoided applying highly anodic potentials where the reliability of other MS signals could be compromised.

Moreover, at even further anodic potentials, potentiostat is overloaded due to bubble formation and consequent conductivity loss which significantly limits the application of highly anodic potentials. Consequently, to ensure reliable and accurate measurements, it was crucial to carefully select the potential range for the experiments and avoid extreme anodic conditions that might compromise the data quality.

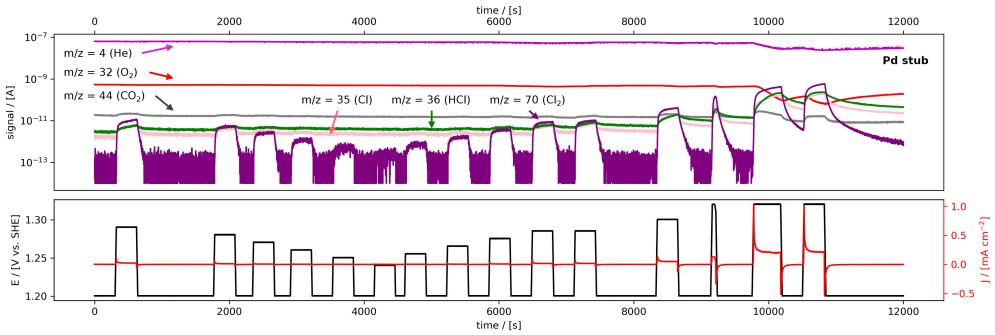

Figure 6.9 Helium as a carrier gas at 70 eV. Increase in m/z = 36 is observed with the increase in Cl_2 formation.

6.2 Activity Evaluations

I aimed to assess the activity of various catalysts by conducting tests to observe their Cl_2 detection potential and overpotential. This section will provide a comprehensive overview of the experimental data for each catalyst, highlighting the specific challenges I encountered during the testing process. Additionally, I will present a comparative analysis of the activity exhibited by all the tested catalysts. The surface characterizations of the catalysts are given in Appendix. In addition to the catalysts listed below I also tested Pd, Au, SnO_x, GeO_2. However, all these catalysts are immediately dissolved in the electrolyte during the anodic scan. As there is no useful data obtained from them they are not included in this thesis.

6.2.1 Detection Potentials for Each Catalyst

RuO_2 on Ti substrate

The RuO_2 catalyst is prepared with the sputtering method on a Ti substrate in the following experiments. In Figure 6.10, the overall experiment for CER performance evaluation on RuO_2 catalyst is given. An increase in the CO_2 signal is observed at potentials starting from 1.30 V vs. SHE. As there is no intentional source of carbon species in the electrode or the electrolyte this increase in CO_2 is attributed to the carbon contamination on the surface.

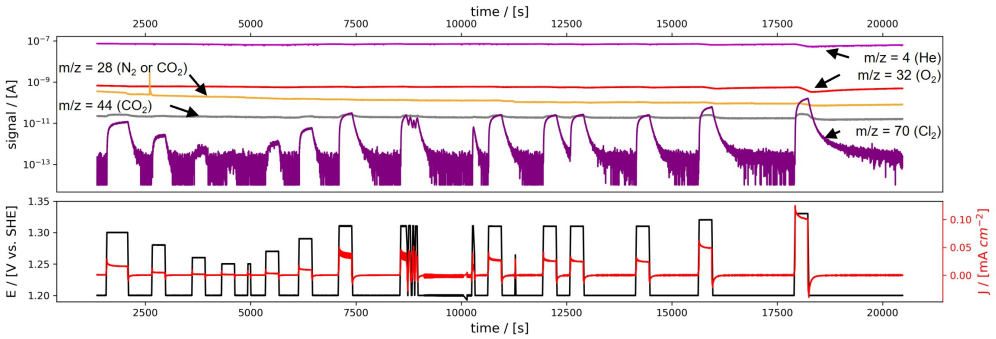

Figure 6.10 Overall look at the signals for He, N_2, O_2, CO_2, and Cl_2 while performing CER at different potentials on RuO_2 on Ti substrate.

In Figure 6.11 all the isotopes and HCl signal is seen. Here, it is seen that the m/z = 70 is the most prominent signal and with Cl_2 formation, an increase in all fragments is observed. Additionally, HCl signal is increasing with Cl_2 formation. The isotopes are recorded for all the catalysts and the same behavior is observed but as it is not giving important information about catalyst's activity I will not give the isotopes for the rest of the catalysts.

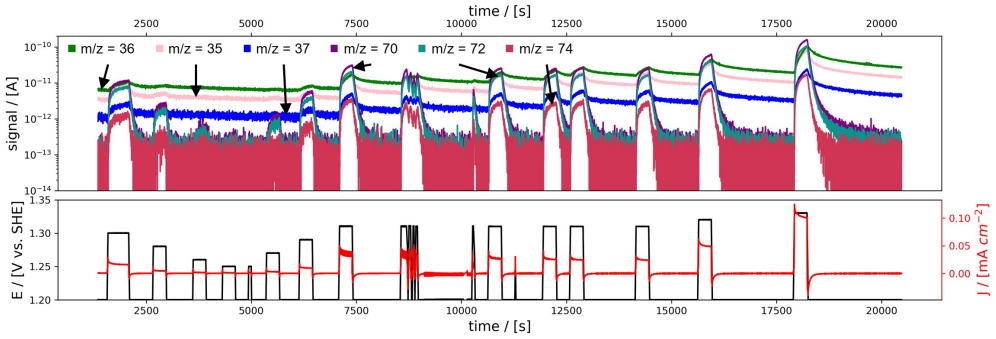

Figure 6.11 MS signals related to Cl_2 isotopes, fragments and derivative (HCl). Test is performed on RuO_2 o Ti.

Another important criteria while assessing the performance of a catalyst is selectivity. As given in Chapter 2, the side reaction for CER is OER. In Figure 6.12, a close look to O_2 signal is given. At anodic potentials where CER is observed, it is seen that there is no increase in O_2 signal, but a decrease observed. This decrement might be

due to two things. First, and most likely is due to the formation of excessive amount of Cl_2, the partial pressure of O_2 in the gas mixture going to MS is lower. Second, but less likely to give this prominent decrement could be to the decreased sensitivity of MS due to HCl formation as mentioned in literature [50]. As no increase is observed in the O_2 signal, the selectivity for CER assumed 100%, neglecting the catalysts dissolution. Initially, analyzing the dissolved catalyst amount with inductively coupled plasma mass spectrometry (ICP-MS) is aimed for this study. However, at that time ICP-MS was broken so analysis could not be conducted. It should be noted that due to the fact that, I do not have a comprehensive information about the selectivity due to lack of catalyst dissolution analysis, I have not compared the selectivity of different catalysts in this study.

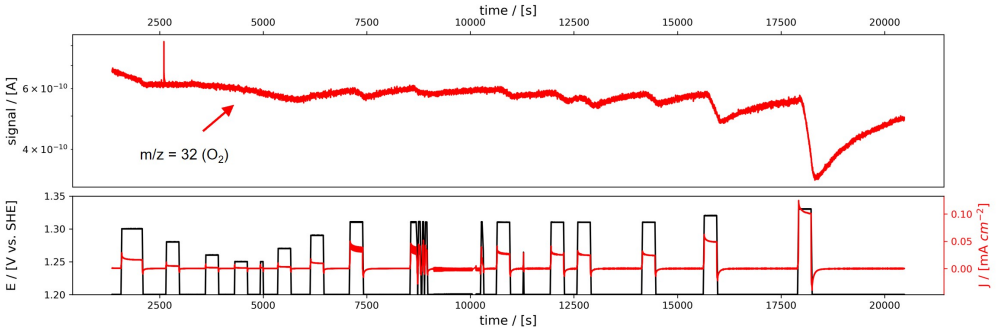

Figure 6.12 Close look to O_2 signal throughout the experiment performed on RuO_2 on Ti.

In Figure 6.13, the lower anodic potential range on RuO_2, and the signal to standard deviation of the noise is given. At 1.25 V vs. SHE, the signal is only 1.8 times of the standard deviation, so it is not assigned as the detection potential. However, at 1.26 V vs. SHE, the ratio is 5.2 σ, so this is the detection potential. Additionally, the lower Cl_2 signals becomes stable easier, however as the Cl_2 signal gets higher, a stable Cl_2 signal is not observed, instead the signal looks like increasing continuously. The reason for this remains unclear, however the issue and possible explanations are addressed at the end of this chapter.

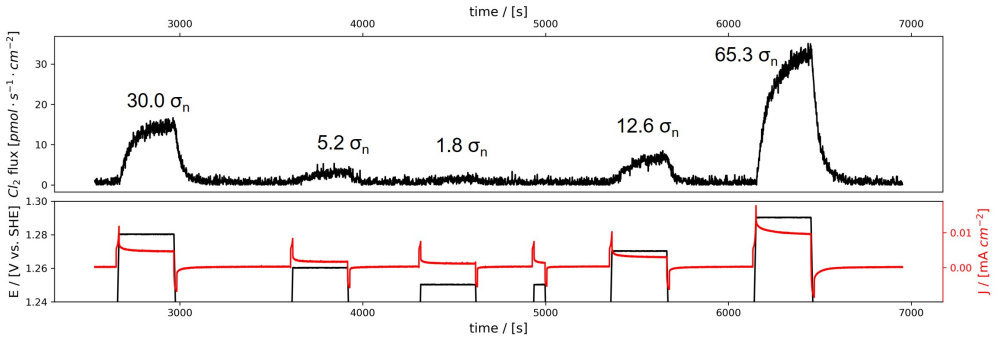

Figure 6.13 Cl_2 flux at varying potentials for the detection potential determination on RuO_2 on Ti. Signal intensity to standard deviation of the noise (σ_n) is given on top of each signal increase.

IrO_2 on GC substrate

The IrO_2 catalyst is prepared with sputtering method as well. IrO_2 sputtered on GC substrate as well as Ti substrate. As they both gave the same results, I have used the IrO_2 on Ti substrate for the calibration experiments as it might posses better stability for the excessive usage as the calibration experiments are repeated many times. Therefore, the following data that I provide for the activity study of IrO_2 belongs to IrO_2 on GC substrate.

In Figure 6.14, the Cl_2 evolution at varying constant potentials on IrO_2 for 5 minutes is given. It is seen that at sufficiently anodic potentials, with CER, Cl_2 signal at m/z = 70 is increasing. During the application of these anodic potentials, CO_2 signal is not increasing, except at 1.30, and 1.31 V vs. SHE a small increase in CO_2 signal is observed, however this increase is very small and also observed at the catalysts coated on Ti substrate showing that it can be caused due to oxidation of any organic contamination. Additionally, the spikes in the m/z = 28 signal is due to the small air bubbles trapped in the system belonging to N_2 and appears simultaneously with O_2 spikes. This does not affect experimental results for the CER performance analysis.

Moreover, at this potential range the closer look to O_2 signal shows increment, showing that there is no OER in Figure 6.15. It is also seen that the O_2 signal constantly dropping during the course of the experiment. The same decrement is seen for all the MS signals, as also can be seen in 6.14. A decrease in the MS signals are always

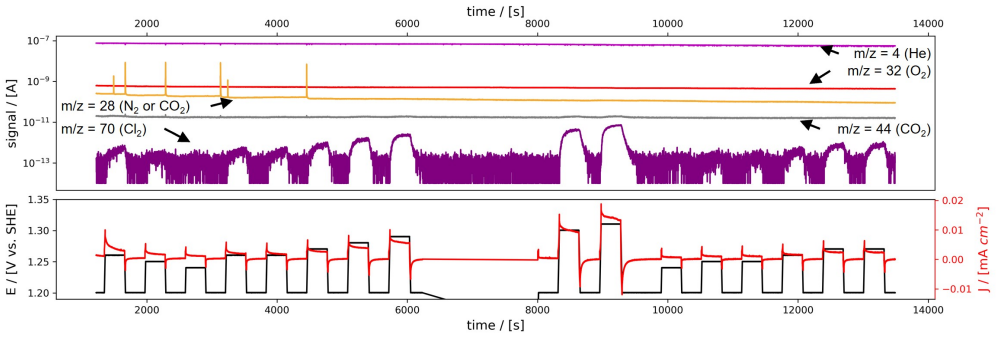

Figure 6.14 Overall look at the signals for He, N_2, O_2, CO_2, and Cl_2 while performing CER at different potentials on IrO_2 on GC.

observed due to the secondary electron multiplier aging, and to avoid this it is tuned before each experiment as mentioned in 3. However, during the CER experiments the decrease in the signals seem to be faster which can be due to enhanced degradation caused by highly reactive Cl_2 species as mentioned in the literature [51].

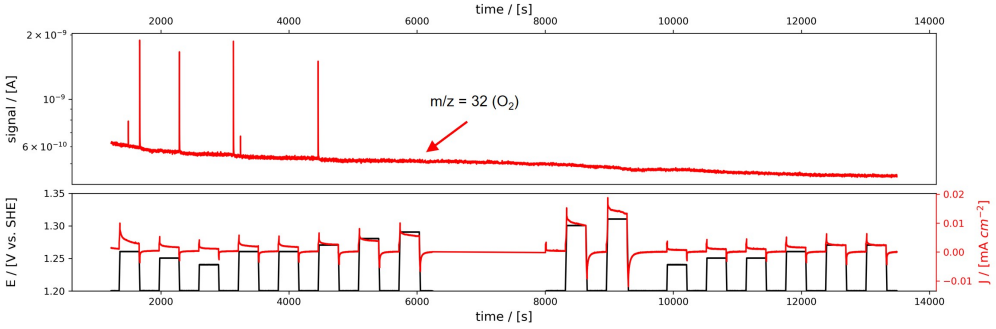

Figure 6.15 Close look to O_2 signal throughout the experiment performed on IrO_2 on GC substrate.

The detection potential on IrO_2 is determined as 1.26 V vs. SHE with given signal to standard deviation of baseline noise ratio being above 2 as shown in Figure 6.16. At 1.25, and 1.24 V vs. SHE the Cl_2 signal is below the detection limit.

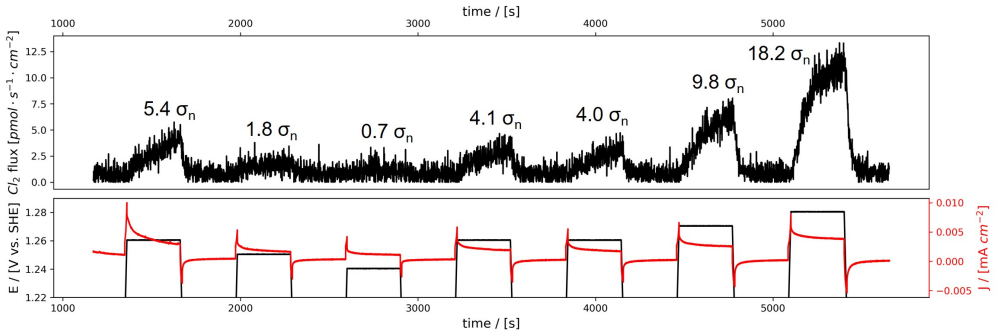

Figure 6.16 Cl_2 flux at varying potentials for the detection potential determination on IrO_2 on GC. Signal intensity to standard deviation of the noise (σ_n) is given on top of each signal increase.

Pt stub

Pt stub with 99.99% purity is tested for CER. The importance of using Pt stub is that it is an "infinite" source of Pt, as it is not a coating when the surface Pt atoms are dissolved there are always more. As Pt is not known as a stable catalyst for CER I wanted to use a stub to avoid the complete dissolution of the catalyst. However, following Pt stub, I have also tested the Pt sputtered on Ti substrate catalyst to see the if there is a severe stability problem and if there is a difference in observed activity.

In Figure 6.17, the overall look for the CER performance evaluation experiment on Pt stub is given. Similar to the previous experiments, it is seen that the Cl_2 signal is increasing, with sufficiently anodic potentials. All the MS signals are decreasing over time. Small increase in CO_2 signal is observed due to surface contamination oxidation at above 1.285 V vs. SHE.

O_2 signal over the experiment did not show any increment, showing that at the potential range applied up to 1.32 V vs. SHE, OER is not observed. Again, considering the excessive Cl_2 formation at 1.32 V could jeopardize the sensitivity of the MS, however as no activity comparison at these highly anodic potential has made, this does not have any importance for this study.

For Pt stub, the detection potential is measured as 1.25 V vs. SHE, which is 10 mV lower than IrO_2 and RuO_2. I refer to catalyst as Pt however, at these potential range which is more anodic than 1.20 V vs. SHE at pH = 0.96, according to Pourbaix diagram,

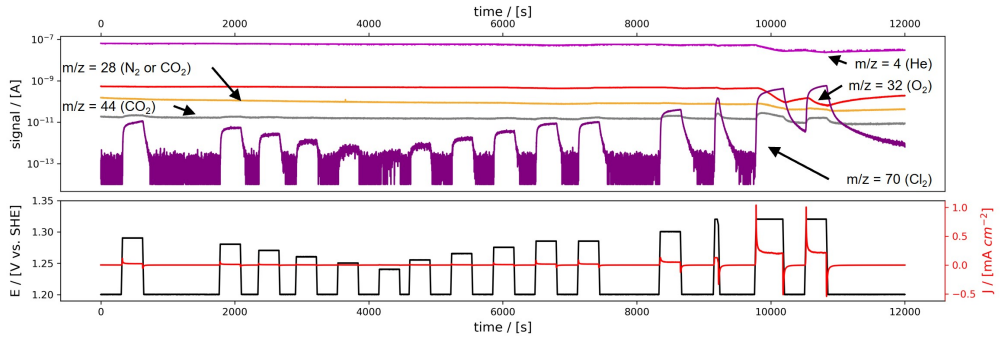

Figure 6.17 Overall look at the signals for He, N_2, O_2, CO_2, and Cl_2 while performing CER at different potentials on Pt stub.

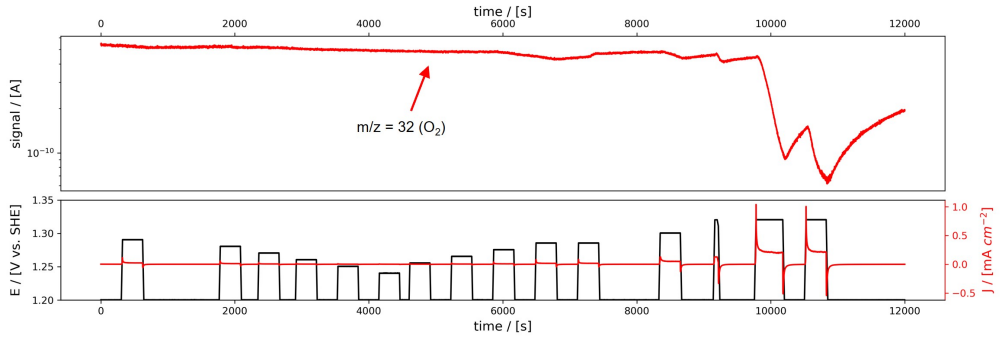

Figure 6.18 Close look to O_2 signal throughout the experiment performed on Pt stub.

Pt should be oxidized to PtO_2 [97]. However, as I do not know the oxidation state of Pt during the reaction conditions, I continue to refer it as Pt stub as its initial state. In the literature, the theoretical studies for Pt are conducted as PtO_2 state, so the activity of PtO_2 is expected to be lower than the RuO_2 and IrO_2 catalysts [38].

My initial idea about this lower detection potential for Pt stub was that RuO_2 and IrO_2 catalysts were coatings on a substrate, so as the reaction proceeds the catalyst film might be dissolved and therefore there are less available active sites for CER, which results in less production rate for Cl_2. However, even the Pt is dissolved, there are still more Pt available to catalyze CER. To investigate, if this superiority over RuO_2 and IrO_2 caused due to the fact that I used a stub instead of a film, I have tested Pt film sputtered on Ti substrate following.

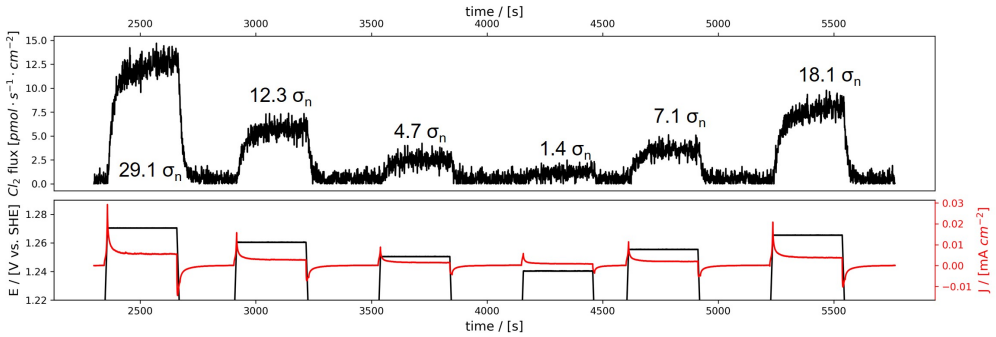

Figure 6.19 Cl_2 flux at varying potentials for the detection potential determination on Pt stub. Signal intensity to standard deviation of the noise (σ_n) is given on top of each signal increase.

Pt on Ti substrate

To test the effect of Pt film instead of stub on the CER activity, I have tested Pt sputtered on Ti substrate, but still bulk as it is 100 nm thickness. In Figure 6.20, the conducted full experiment is given. CO_2 formation starting at 1.28 V vs. SHE is seen due to contamination oxidation.

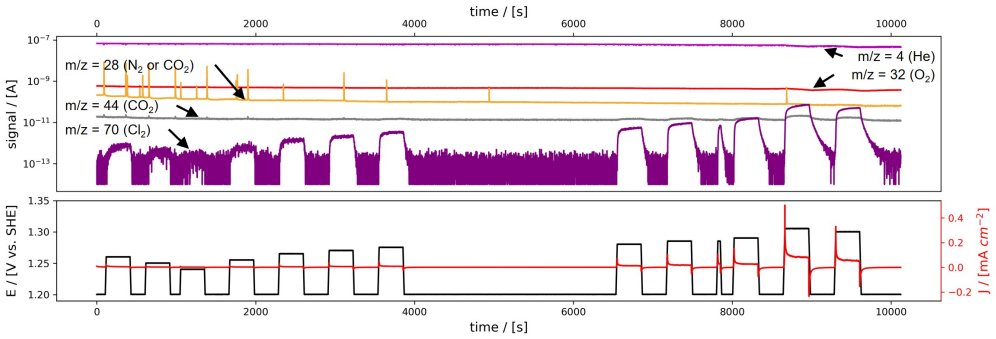

Figure 6.20 Overall look at the signals for He, N_2, O_2, CO_2, and Cl_2 while performing CER at different potentials on Pt on Ti substrate.

In Figure 6.21, O_2 signal is seen on Pt on Ti sample. At the potential range up to 1.31 V vs. SHE, there is no O_2 formation is observed. Therefore, there is no selectivity issue between OER and CER in this experiment.

Finally, the detection potential for Cl_2 on Pt on Ti substrate determined as 1.255 V vs. SHE. Cl_2 was not detected at 1.25 V vs. SHE given in Figure 6.22.

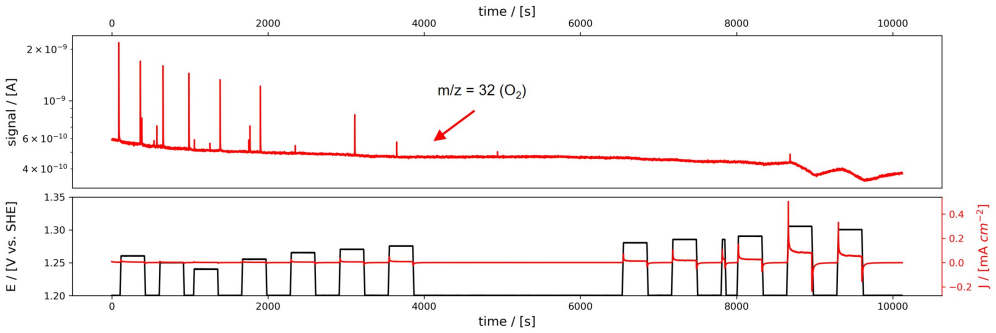

Figure 6.21 Close look to O_2 signal throughout the experiment performed Pt on Ti substrate.

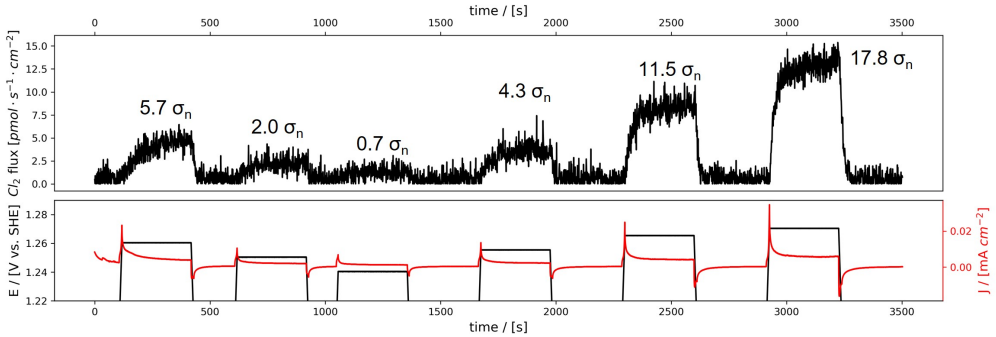

Figure 6.22 Cl_2 flux at varying potentials for the detection potential determination on Pt on Ti substrate. Signal intensity to standard deviation of the noise (σ_n) is given on top of each signal increase.

TiO_2/Pt on GC substrate

This sample is prepared by ALD method on the GC substrate with 2 nm of TiO_2 layer on top of 20 nm of Pt layer given in 6.2c. This very thin TiO_2 layer could have tune the Cl^- and O binding energies, therefore the catalytic activity as previously mentioned [39, 65].

In Figure 6.23, the CER activity evaluation experiment on TiO_2/Pt on GC sample is given. It is seen that, there are many air peaks from the increase of N_2 and O_2 signals which does not affect the performance evaluation.

In Figure 6.24, it is seen that there is no O_2 formed during the anodic potentials for this catalyst too. Finally, in Figure 6.25 the detection potential on TiO_2/Pt on GC

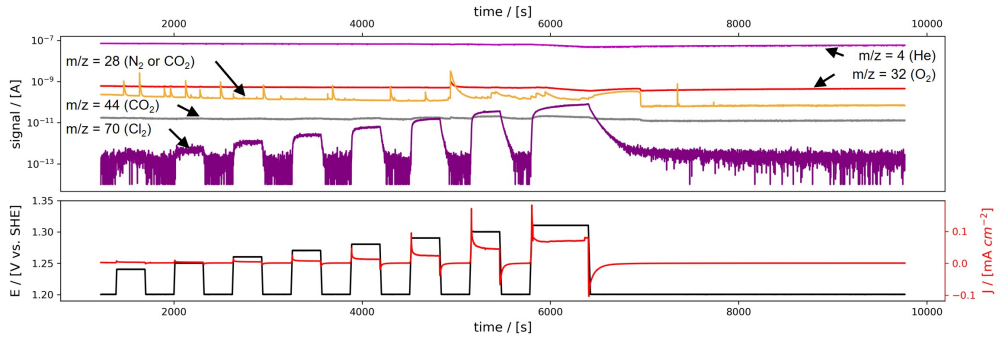

Figure 6.23 Overall look at the signals for He, N_2, O_2, CO_2, and Cl_2 while performing CER at different potentials on TiO_2/Pt on GC.

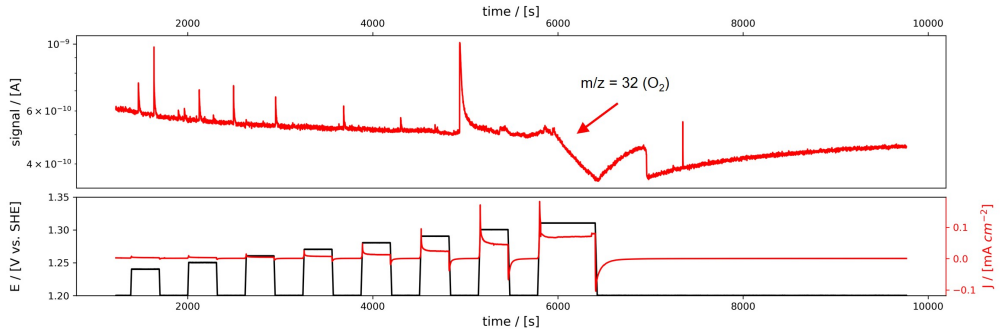

Figure 6.24 Close look to O_2 signal throughout the experiment performed on TiO_2/Pt on GC substrate.

catalyst is measured as 1.25 V vs. SHE, which is the same with Pt stub and only 5 mV lower than Pt on Ti substrate samples. This result, showed that superiority of Pt stub is not stemmed from the fact that it is a stub, as Pt on Ti and TiO_2/Pt on GC samples have lower detection potential for Cl_2 than RuO_2 and IrO_2 as well. The TiO_2/Pt on GC sample before and after experiment is characterized with XPS and ISS methods given in the Appendix Figure A.17, A.18, and A.19. As a result, it is seen that even though thin layer of TiO_2 exist on the surface before the experiment, after the experiment it disappears. Therefore, these activity results simply could be belong to Pt layer on a GC substrate.

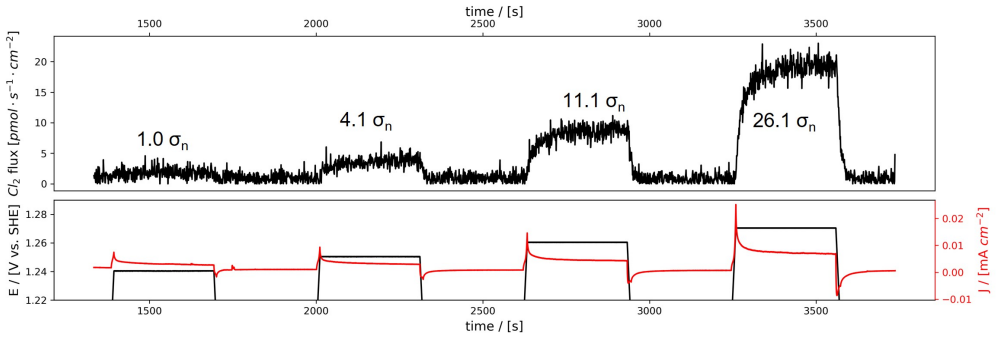

Figure 6.25 Cl_2 flux at varying potentials for the detection potential determination on TiO_2/Pt on GC. Signal intensity to standard deviation of the noise (σ_n) is given on top of each signal increase.

TiO_2 (Ti stub)

Additionally, I have done a blank experiment with Ti stub. It should be noted that, Ti stub at the operation conditions should be TiO_2 [97]. Unfortunately, I could not employ XPS to analyze the surface contamination after experiment for this sample. It is because, after I have tested Ti stub for this experiment, I have used it for other purposes as a substrate without realizing that I forgot to do post-experiment XPS. As this was at the very end of my PhD, I could not repeat the test. Therefore, the results for CER activity on Ti stub should be critically interpreting by considering the possible contamination.

In Figure 6.26, the CER performance test on TiO_2 is given. The decrease in the Cl_2 signal when the potential is changed from the test potential to the resting potential (1.23 V vs. SHE) is seems to be slower, which could be due to the slower chlorine reduction reaction kinetics on Ti stub. Throughout the experiment, no CO_2 formation is observed.

In Figure 6.27, there is no OER observed in the applied potential range, showing that at the potential range of 1.28 - 1.32 V vs. SHE, OER is not a side reaction.

Finally, the detection potential on TiO_2 is measured at 1.29 V vs. SHE. Even though this potential is 30 mV higher than on RuO_2, IrO_2, and Pt, it is still a low anodic potential than expected on TiO_2 as it is known as inactive for CER [34]. As mentioned previously, this could be due to a potential contamination or due to the high sensitivity of EC-MS and very low Cl_2 concentration resulting in very low equilibrium potential.

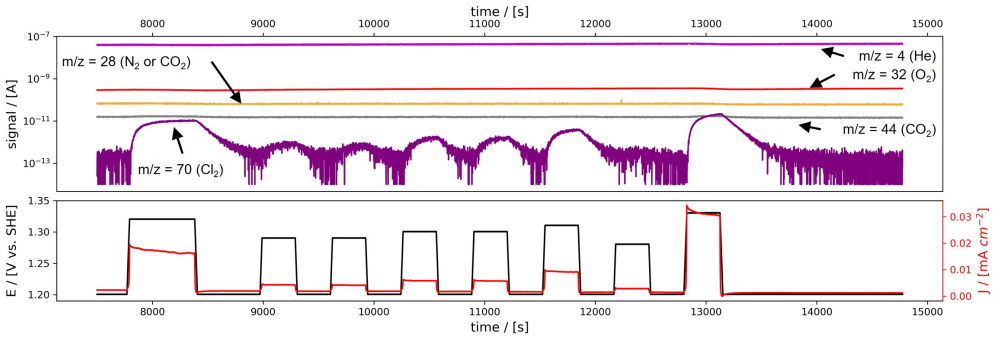

Figure 6.26 Overall look at the signals for He, N_2, O_2, CO_2, and Cl_2 while performing CER at different potentials on Ti stub.

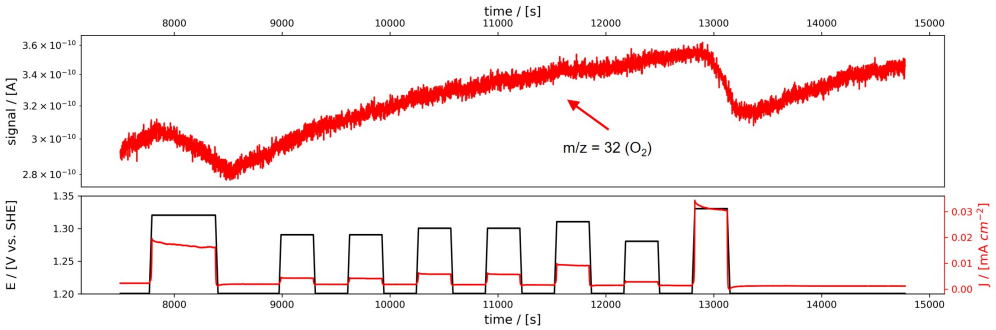

Figure 6.27 Close look to O_2 signal throughout the experiment performed on Ti stub.

Additionally, TiO_2 is a wide band gap semiconductor being non-conductive, however at these low anodic potentials and with the suppression of oxygen species binding to surface via Cl^-, the oxide growth might be limited to couple of monolayers.

In conclusion, comparing the detection potentials for all these catalysts the difference was no more than 10 mV, which might not represent an important difference. Finally, as the detection potentials were very close to each other, I compared the Cl_2 production rate at 1.30 V vs. SHE, where it is at highest without compromising from the sensitivity of other signals. In Figure 6.29, as highlighted with red, the Cl_2 flux at the last 60 seconds of the potential test at 1.30 V vs. SHE for each catalyst is averaged for CER activity comparison.

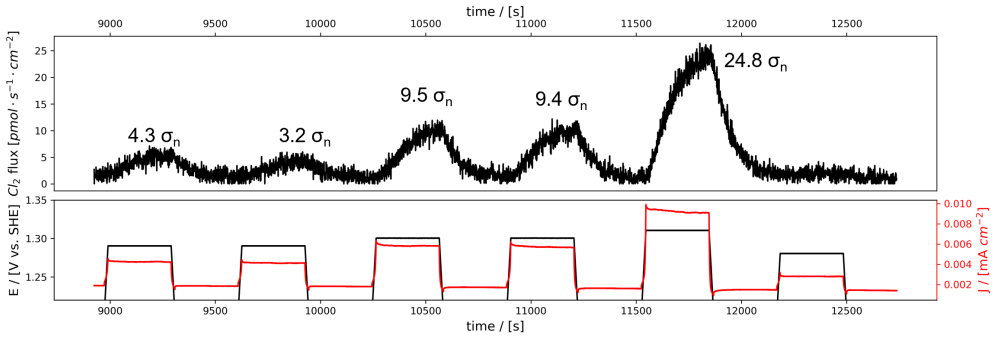

Figure 6.28 Cl_2 flux at varying potentials for the detection potential determination on Ti stub. Signal intensity to standard deviation of the noise (σ_n) is given on top of each signal increase.

As a result, in Figure 6.30 it is seen that the activity at 1.30 V vs. SHE from highest to lowest is Pt on Ti, TiO_2/Pt on GC, Pt stub, RuO_2 on Ti, IrO_2 on GC, and TiO_2 with Cl_2 production rates of 306, 268, 193, 66, 32, 10 pmol s^{-1} cm^{-2}. According to DFT calculations, higher activity on RuO_2 than IrO_2 is expected, same as the experimental results reported in this study [43]. However, the superior activity of Pt-based catalysts over RuO_2 was unexpected both based on theoretical studies [38, 42]. Finally, substantially low CER activity on TiO_2 is consistent with the existing literature [63].

6.2.2 High CER Activity of Pt-based Catalysts

As a result of the activity comparison at 1.30 V vs. SHE, it is seen that all the Pt-based catalyst have higher activity than RuO_2 and IrO_2. Although, we could not explain this to this day, in this section I will present some possible explanations which could guide future studies.

Initially, I thought that this could be due to the increase in the surface roughness of Pt-based catalysts as they are less stable. However, post-experiment ECSA calculation with CO stripping showed that the surface area remained almost the same as $\approx$ 0.194 cm^2. Therefore, I concluded that the increased surface area during the reaction conditions for Pt cannot be the reason for higher Cl_2 production rate.

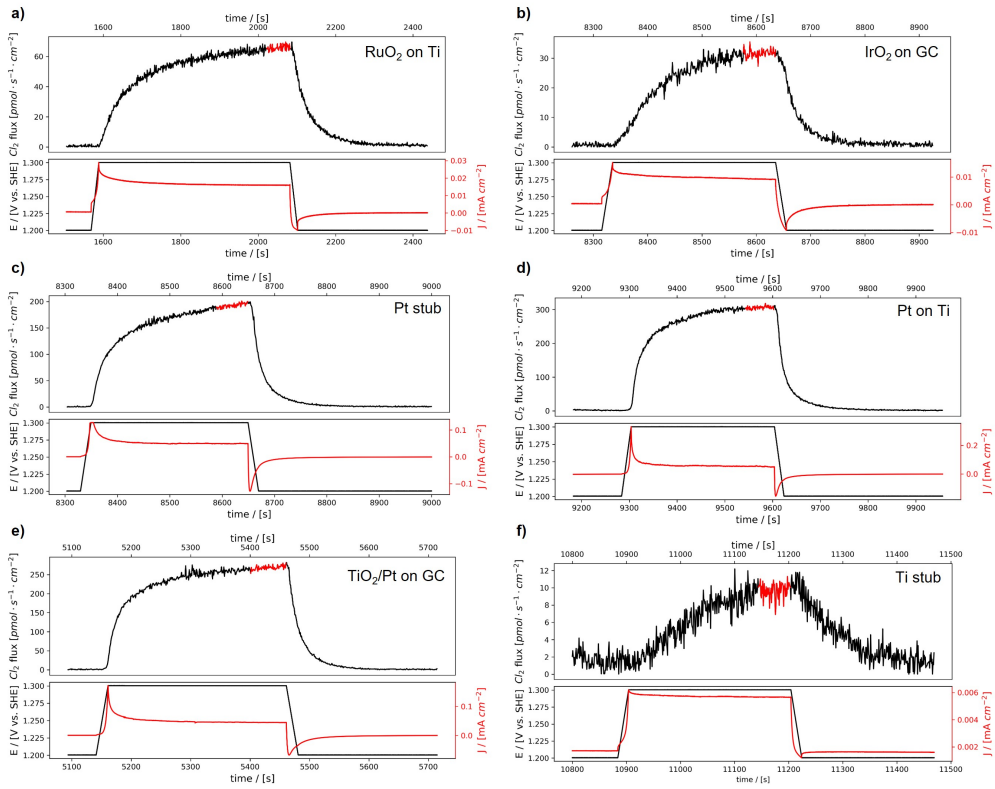

Figure 6.29 Cl_2 flux at 1.30 V vs. SHE for (a) RuO_2 on Ti, (b) IrO_2 on GC, (c) Pt stub, (d) Pt on Ti, (e)TiO_2/Pt on GC, and (f) Ti stub. The Cl_2 flux indicated with red region is averaged for the final comparison of the catalysts.

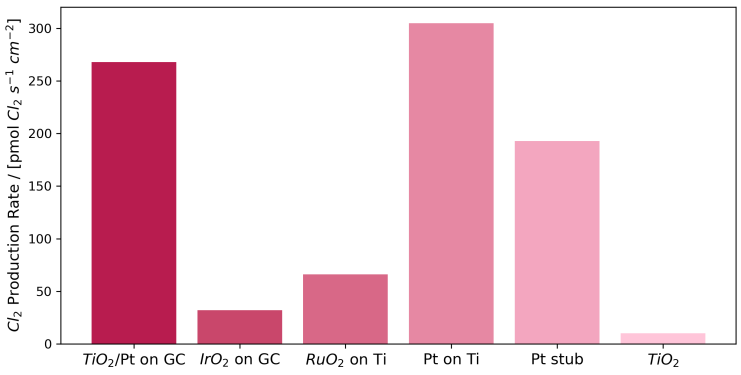

Figure 6.30 Comparison of CER activities on different catalysts based on Cl_2 production rate at 1.30 V vs. SHE.

Secondly, I thought that presence of Cl^- in the electrolyte might suppress PtO_2 formation as Cl^- competes with oxygen species for adsorption. As a result, the catalyst might remain in metallic state. It proposed that CER on metallic Pt starts with Pt-Cl formation, whereas on PtO_2 the ClO^c sites are required for CER, and higher activity for CER on metallic Pt than PtO_2 reported [61]. Additionally, it is known that in the presence of Cl^-, the adsorption of oxygen species to surface becomes harder [62]. Furthermore, Vos et al. showed that the presence of Cl^- more than 10 mM prevents the PtO_x formation on the surface. I designed two experiments to test the effect of Cl^- on PtO_2 formation [48].

First, I aimed to quantify the available sites by employing CO stripping in the presence and absence of Cl^- to see what portion of active sites are blocked by Cl^- and adsorption of oxygen species (OH or O^{2-}) are prevented. However, as seen in Figure 6.31, in the presence of Cl^- due to excessive Cl_2 formation, aimed potential could not be applied even though the scan rate was as small as 5 $mV\,s^{-1}$. Even though, I could not quantify the available sites in the presence and absence of Cl^-, this experiment revealed the shift towards more anodic potentials for CO oxidation to CO_2 in the presence of Cl^-. When the CO stripping employed in 0.1 M $HClO_4$, the CO oxidation potential is $\approx$ 0.5 V vs. SHE, but in the presence of 1 M NaCl it is shifted to $\approx$ 1.10 V vs. SHE. This shows the retardation of oxygen species' adsorption to surface in the presence of Cl^- as the reaction cannot be limited by the CO adsorption as CO is already adsorbed on the surface before the potential scan starts.

The second experiment I designed was aiming to answer following question: Could I retard CER activity if I oxidize Pt to PtO_2 intentionally? This could be done by applying highly anodic potentials to fully oxidize Pt, and then test the CER activity without removing the potential control as PtO_2 would reduce in the ambient conditions once the sufficient anodic potential is removed. First, I tried this experiment in 0.1 M $HClO_4$ + 1 M NaCl electrolyte, however application of highly anodic potentials was impossible due to bubble formation. Then, I thought about oxidizing Pt in 1 M $HClO_4$, and then flushing the electrolyte with 0.1 M $HClO_4$ + 1 M NaCl without removing the potential control. As with the current electrochemical cell design this was not possible I did a modification in the setup by using T-type valve for electrolyte inlet to achieve electrolyte change during the reaction. I inserted a syringe containing Cl^--free

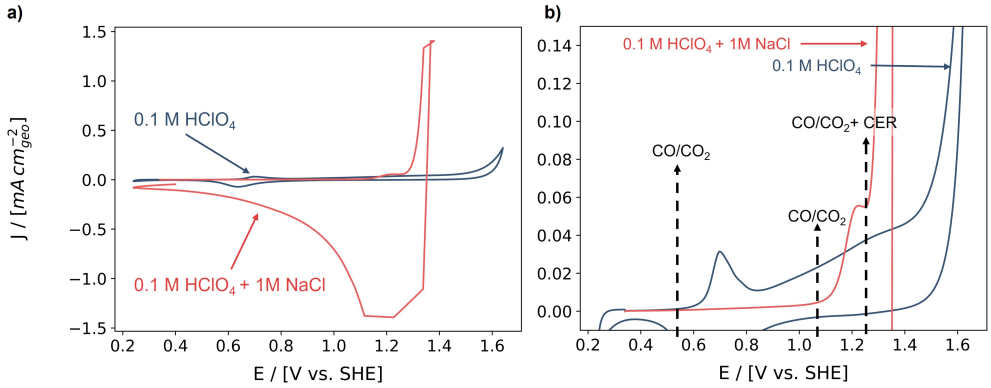

Figure 6.31 Cyclic voltammetry for CO stripping on Pt with in 0.1 M $HClO_4$ + 1 M NaCl (red), and 0.1 M $HClO_4$ (blue). (a) Overall look to CV. (b) Close look to oxidation peaks, and onset of each reaction is indicated on the CV.

electrolyte to one inlet and another syringe containing Cl^- electrolyte to another inlet (Figure 6.32).

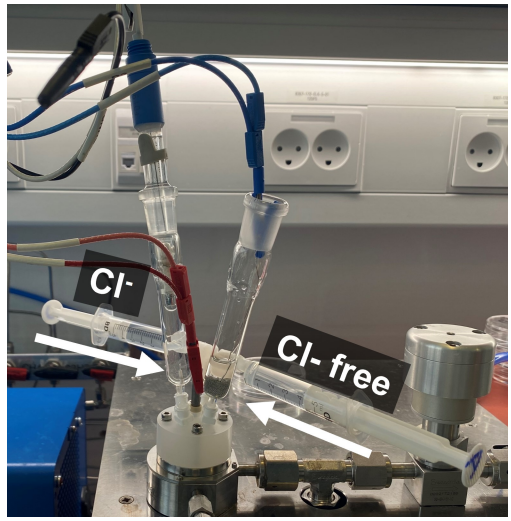

Figure 6.32 Setup consist of t-type valve to enable electrolyte change during the experiment to enable pre-oxidation of Pt before conducting CER.

In Figure 6.33, this experiment is given and it is separated to regions based on the electrolyte content which are labeled with numbers on the Figure. The electrolyte

changes can be observed by looking at air peaks (O_2 and N_2) as during the electrolyte change air insertion to cell happens at the same time. In region 1, 3, 4, the electrolyte is $HClO_4$, and in region 2 and 5 the it is switched with NaCl containing electrolyte.

However, application of this experiment is very hard due to several reasons. First of all, I have started the experiment without Cl^- and I increased the potential from 1.2 to 1.64 V vs. SHE. After this high potential, I aimed to go to 1.3 V and change the electrolyte simultaneously to start CER. However, as I was scanning the potential down to 1.3 V with 5 $mV\,s^{-1}$, CER have already started at highly anodic potentials as it is seen in region 2. Then, in region 3, I have changed the electrolyte back to Cl^--free and waited until the MS signals go back to baseline. I have tested if the electrolyte is Cl^--free by applying 1.3 V vs. SHE at t = 3200 s and no Cl_2 formation is observed. Afterwards, I started to scan the potential towards 1.64 V for oxidation, however a high Cl_2 peak is observed at t = 3555 s showing that the electrolyte is not completely Cl^--free. In region 4, the cell is flushed one more time with Cl^--free electrolyte and oxidation continued. Finally, in region 5, potential is dropped from 1.64 to 1.30 V directly without scanning and the electrolyte is changed back to Cl^- containing at the same time. As a result, Cl_2 signal at $\approx 2.8\ 10^{-12}$ A is observed. Subsequently, the application of potential is stopped and electrode waited under open circuit potential in between t = 4350 - 6000 s, in which PtO_2 reduction to metallic Pt is expected. Afterwards, 1.20 V is applied and potential is scanned to 1.30 V to see if after the reduction of PtO_2 Cl_2 formation improved. On contrary, a decrease in Cl_2 signal is observed compared to right after the surface oxidation CER test. It should be noted that right after the oxidation current density is at least 2 times higher, indicating this observation could be due to increased current density due to improved mass transport during the dynamic electrolyte move.

In conclusion, this experiment could not provide useful information due to many uncertainties in the experimental setup, including changing mass transport due to dynamic electrolyte movement, MS signals not reaching to baseline due to the need for fast potential change, Cl^- contaminated electrolyte as the cell could not be disassembled and cleaned thoroughly.

In conclusion, although there I could not fully explain the higher activity on Pt-based catalysts towards CER, I presented the hypothesis of Cl^- might prevent fully

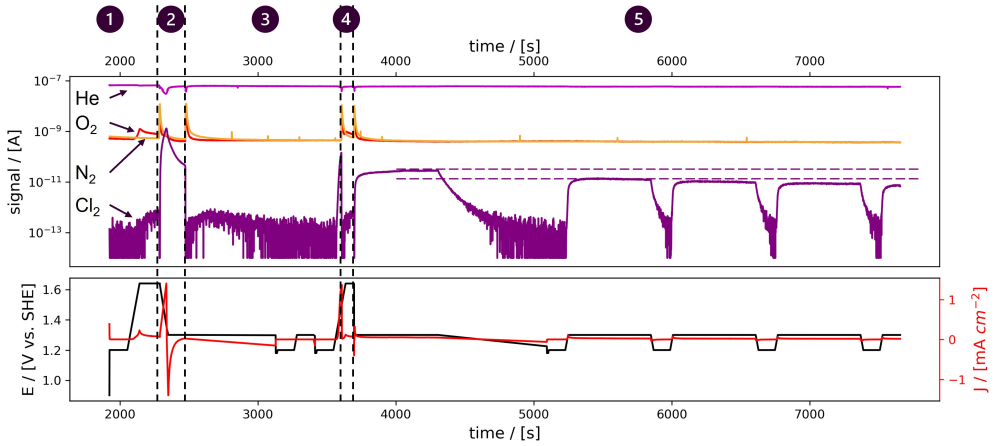

Figure 6.33 Mass spectrum for the pre-oxidation trial on Pt. Mass spectrum is divided into 5 regions to ease the description of events through out the experiments. Details about the events are given in the text.

oxidation of Pt to PtO_2, therefore there might be still metallic Pt available on the surface which is known to have higher activity towards CER than RuO_2 and IrO_2 [61].

6.3 Definition of the Equilibrium Potential in the Literature

An important note is that detection potentials as low as these have not been reported before with any instrument according to best of my knowledge. Being able to detect Cl_2 at these low overpotentials is significant when it comes to defining fundamental concepts such as equilibrium potential and overpotential. Overpotential is defined as the difference between the equilibrium potential and applied potential according to the Equation 1.7. Therefore, to declare the overpotential, it is necessary to know the equilibrium potential.

In this study, the equilibrium potential calculated with Nernst equation (Equation 1.6) based on the assumptions made in the literature was always higher than the detection potential. I conducted an extensive research about the equilibrium potential definitions reported, and realized that there is no universal definition of the equilibrium potential for CER. Many different approaches are followed by the researchers, and in most cases the equilibrium potential is not even mentioned while reporting an overpotential. In

CER, the activity of Cl_2 changes over the course of the experiment if the electrolyte is not purged with Cl_2. As chlorine reduction reaction is a fast reaction as well, the equilibrium potential is affected by the changing Cl_2 activity.

The main problem caused by this is the catalysts tested in different studies becomes incomparable. As the overpotential for CER is already low due to fast kinetics of the reaction, the differences in overpotentials reported in the literature are in 10 mV range, thus the comparison between studies becomes meaningless. In the following paragraphs, I will present a summary of equilibrium potentials in the literature.

First and most straightforward definition is based on the Nernst equation. For Cl_2 evolution the Nernst equation can be written as:

$$E_{CER} = E^0_{CER} + \frac{RT}{2F} ln \frac{a(Cl_2)}{a(Cl^-)^2} \tag{6.3}$$

where, E^0_{CER} is standard potential of CER, R is the gas constant, T is temperature, F is Faraday constant, α is chemical activity, and E_{CER} is the equilibrium potential.

Under the standard conditions E_{CER} is calculated as 1.358 V vs. SHE, in which the $a(Cl_2)$ and $a(Cl^-)$ is 1. However, this reaction is rarely conducted under standard conditions in the fundamental studies due to the difficulty of having 1 bar Cl_2 as it is highly toxic. As Cl_2 is formed throughout the experiment, the activity of Cl_2 is constantly changing. Additionally, if highly concentrated Cl^- is used, activity of Cl^- can be assumed constant, however it would deviate from 1 depending on the concentration. Even though this is the case, some studies assumes the equilibrium potential as 1.358 V vs. SHE [48, 51, 52].

Another group of researchers [50, 58, 98, 99], assume $a(Cl_2) = 0.01$ based on Guerrini and co-workers [100], in which it is clearly mentioned that this only provides qualitative comparison as the electrolyte is constantly purged by an inert gas. However, with the following studies, this disclaimer seems to disappear. The reasoning for the assumption of $a(Cl_2) = 0.01$ is not explained in any study, and we could not understand it to this day.

The other way of determining equilibrium potential in the literature involves the linear extrapolation of the polarization curve to the zero current based on the Butler-Volmer equation's low overpotential regime (Equation 1.9). In the study of Sohrabnejad-

Eskan et al. this method is employed and the potential range is chosen at where CER is observed but OER is not started yet as given in the Figure 6.34 [50]. This method is sensitive to chosen potential range and the amount of data points selected.

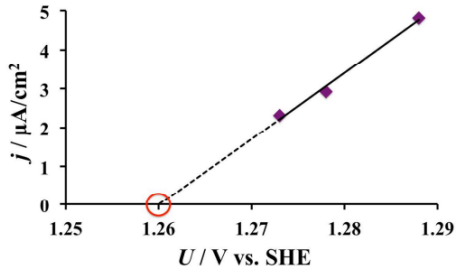

Figure 6.34 The polarization curve is extrapolated to zero current density in the CER range and the equilibrium potential is determined as 1.26 V vs. SHE at 25°C with 10^{-5} M HCl in 5 M NaCl electrolyte. Reprinted with permission from [50]. Copyright 2017 American Chemical Society.

The ideal way of defining the equilibrium potential is purging the electrolyte with Cl_2 gas to have high enough Cl_2 at all times, therefore the activity of Cl_2 remains the same. The main challenge with this method is purchasing Cl_2 gas, as it is highly reactive and toxic. During my PhD, I contacted many suppliers and the highest concentration of Cl_2 gas that I could find was 100 ppm. However, in the literature, some studies reported that they purged the electrolyte with Cl_2 [57, 65]. In another study, prior to CER activity evaluation electrolyte is saturated with Cl_2 by producing Cl_2 at 10 V at least for 30 minutes [45]. In my opinion this method could be a good alternative but one should be careful about deterioration of the catalyst prior to experiment as rigorous potentials were applied for a long time. However, either purging the electrolyte with 1 bar Cl_2 or pre-saturation of electrolyte with Cl_2 by applying anodic potential might not be applicable in the case of *in-situ* MS studies as Cl_2 is highly corrosive for the MS components.

6.4 Determination of the Equilibrium Potential

Assumption of $a\mathrm{Cl}_2 = 0.01$

Firstly, I calculated the equilibrium potential according to Equation 6.3 by assuming the $a\mathrm{Cl}_2 = 0.01$ as indicated in the literature [50, 58, 98–100]. As I used 1 M NaCl, the $a\mathrm{Cl}^-$ is taken as 0.657 [101]. Finally, the resulting equilibrium potential for CER is calculated as 1.31 V vs. SHE, which is 60 mV higher than the detection potential on Pt stub. As it is impossible to have an equilibrium potential higher than the applied potential if Cl_2 is produced, $a\mathrm{Cl}_2 = 0.01$ assumption could not be applied.

Linear Extrapolation of the Low Overpotential Regime of the Polarization Curve

Firstly, I have decided to use the linear extrapolation of the polarization curve method at the very low potential range where I could detect Cl_2 and see a linear trend in the polarization curve. In my opinion, this method has certain advantages such as:

(i) Using the same experimental setup as the CER performance test with the same electrolyte composition and volume enables to avoid calculation mistakes that can be cause from the uncertainties while preparing the electrolyte, i.e. varying Cl^- concentration, varying Cl_2 saturation due to different electrolyte volume.

(ii) As the same reference electrode is used during the CER performance test and equilibrium potential measurement the variation due to reference electrode potential would be avoided. It should be noted that one can avoid this by calibrating the reference electrode at all times, which was done in this study. Nevertheless, I believe this method provides simplicity.

For this study, I have used Pt stub and at the lower overpotential regime I changed the potential with 5 mV steps. The experiment is given in 6.17. Then, I plotted the polarization curve, but I used the partial current density for Cl_2 (J_{Cl_2}) instead of the total current density. Even though there was no OER at this potential range, as there might be dissolution of the Pt as a side reaction, I believe it is important to consider J_{Cl_2} instead of the total current density.

In Figure 6.35, when the linear region of the potential is fitted with least squares fitting. Here, the importance of the potential regime chosen for the extrapolation

becomes appearent. If the extrapolation is applied in 1.255 - 1.270 V vs. SHE the equilibrium potential is 1.245 V, if it is applied in 1.270 - 1.285 V the equilibrium potential is 1.265 V vs. SHE. As Cl_2 is detected at lower anodic potentials 1.265 V vs. SHE, it is not applicable, so accepting 1.245 V vs. SHE as an equilibrium potential is more reasonable. In conclusion, the biggest limitation of this method us that it is highly sensitive to potential range selection.

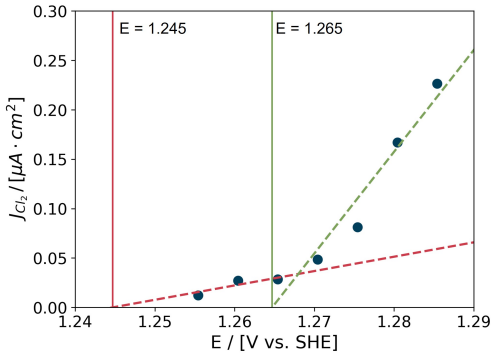

Figure 6.35 Extrapolation of the low overpotential regime of the polarization curve to zero current for Pt stub. Extrapolation of points at 1.255 - 1.270 V vs. SHE is indicated with red line and resulted in E_{CER} = 1.245. Extrapolation of points at 1.270 - 1.285 V vs. SHE is indicated with red line and resulted in E_{CER} = 1.265.

Real-time Equilibrium Potential via EC-MS

Revisiting the initial challenge in establishing an equilibrium potential for CER, we recall that the fluctuating activity of Cl_2 during the experiment hinders researchers from determining a stable and consistent equilibrium potential. Therefore, in this section I addressed the question: "Is it possible to measure the equilibrium potential in real-time using EC-MS?".

To answer this question, initially I take a look at all the variables that should be defined to calculate the equilibrium potential according to Equation 6.3. Temperature and activity of Cl^- does not change significantly as the reaction is ran at room temperature and the Cl^- concentration is high enough to shift the equilibrium. Therefore, the way of determining the real-time equilibrium potential is being able to track the changes in the activity of Cl_2.

The activity is defined as the partial pressure, however as non-ideal gases would interact with the solute there would be deviations from the partial pressure. Considering the interactions of the non-ideal gas with the solute, effective partial pressure is used for defining the activity for gases which is called fugacity. However, for simplicity, I assumed that Cl_2 is an ideal gas in this study. The ideal gas law is given in Equation 6.4:

$$P_i V = n_i RT \tag{6.4}$$

where P_i is the partial pressure of a gas i, V is the volume, n_i is the number of i mols, R is the gas constant, and T is the temperature. Therefore, the partial pressure of Cl_2 can be calculated with the Equation 6.5:

$$\frac{P_{Cl_2}}{P_{tot}} = \frac{n_{Cl_2}}{n_{tot}} \tag{6.5}$$

where, P_{tot} and n_{tot} are the total pressure and total number of moles.

As I have the information of real-time n_{Cl_2} from EC-MS, only variable missing in the equation is n_{tot}. As introduced in Chapter 3, the membrane chip in the EC-MS enables a well defined flux of molecules to the mass spectrometer. Most importantly, the partial pressure above and below the membrane chip remains the same as it provides 100% collection efficiency. Trimarco et al. described the total flux of the molecules going to MS with the Equation 3.7. They have calculated the total molecular flux as $(1.6 \pm 0.3) \times 10^{15}$ molecules/s by considering turbomolecular pump speed as 50 l/s and the pressure in the MS as 10^{-6} mbar [71]. However, very small changes in the MS pressure and therefore in the calculation of the partial pressure of Cl_2, makes great difference in the equilibrium potential. Initially, when I calculated the partial pressure of Cl_2 by assuming the MS pressure as 10^{-6} mbar, the calculated real-time equilibrium potential was higher than the applied potential. However, the pressure in the MS is measured in real-time with the ion gauge pressure sensor, so instead of assuming $P_{Cl_2} = 10^{-6}$ mbar, I used the real time pressure in the MS chamber. One important note is that, as mentioned in Chapter 3, the ion gauge pressure sensor is calibrated according to N_2. As in these experiments He is used as a carrier gas, the correction of the pressure is necessary by applying Equation 3.10. The correction factors for He and Cl_2 are 0.18 and 0.68 respectively [84]. Additionally, even though it does not make a

significant change, I consider the turbomolecular pump speed as 58 $l\,s^{-1}$ based on the specifications provided from the supplier company.

Finally, real-time P_{Cl_2} is calculated with the n_{Cl_2} measured by MS, and n_{tot} is calculated via the implementation of real-time MS pressure. Thereafter, I implemented real-time P_{Cl_2} value to the Nernst equation for CER (Equation 6.3) and obtained the real-time equilibrium potential value.

In Figure 6.36, the calculation results of real-time equilibrium potential are given for Pt stub. First of all, in Figure 6.36a, the Cl_2 flux as a function of time, and with the MS pressure information from Figure 6.36c, the equilibrium potential for CER (E_{CER}) is calculated and plotted together with the applied potential to WE (E_{ap}) in Figure 6.36d. Finally, the difference between the E_{ap} and E_{CER} is highlighted in Figure 6.36d describing the overpotential (η) according to the Equation 1.7.

It is seen that the ion gauge pressure seems like dropping slightly when Cl_2 is produced. This is due to the fact that the high concentration of Cl_2 in the gas mixture arriving to MS changing the gas correction factor that should be applied to a higher value, as gas correction factor for Cl_2 is higher than for He. The gas correction factor can be calculated with if the partial pressure of the each gas in the mixture is known, however as in this study I use the pressure to calculate the partial pressure, it is not possible to back-calculate the correct pressure [82]. I have also tried to use a constant MS pressure corrected for He when there is no Cl_2 production. As a result, there was no significant difference in the calculated real-time E_{CER}.

In Figure 6.36d, the E_{CER} at low Cl_2 concentrations is very noisy. It is because of the combination of two things. First, when the P_{Cl2} is very low, small changes makes big differences in the E_{CER} as in the Equation 6.3 $a\mathrm{Cl}_2$ is in natural logarithm. Secondly, due to the very low concentrations of Cl_2, accuracy of the EC-MS is substantially lower, so the variation in the measured n_{Cl_2} is way higher than at high concentrations of Cl_2. The increase in the E_{CER} with increasing Cl_2 is observed in real-time as well as the η related to this. Additionally, it is seen for the each potential applied after approximately a minute, the E_{CER} becomes more stable, showing that pre-saturation of the electrolyte with Cl_2 helps to obtain stable equilibrium potential. However, the equilibrium potential detected at each potential varies, but in the experimental setups in which higher Cl_2 production rate can be achieved as P_{Cl_2} can be higher, the variation in the E_{CER} would

be lower. The real-time equilibrium potential for the rest of the catalysts are given in the appendix as similar results are obtained.

Limitations of real-time E_{CER} calculation with EC-MS can be summarized as:

(1) At low concentrations of Cl_2, the MS signal is very noisy as the detection ability of the instrument is lower for the lower concentrations. Additionally, the variation in E_{CER} is higher at low P_{Cl_2} regime, and EC-MS does not allow a production of high concentration of Cl_2 due to bubble formation. Therefore, at low Cl_2 concentrations, E_{CER} has high variation.

(2) The effect of P_{Cl_2} in resulting E_{CER} is significant. Thus, E_{CER} is highly dependent on n_{Cl_2} which is obtained by the calibration of the MS. As a result, the correction of the calibration of Cl_2 becomes substantial. However, as mentioned previously the Cl_2 calibration in EC-MS is cumbersome due to the availability of Cl_2 gas mixture and internal calibration comes with inaccuracies due to presence of possible side reactions.

(3) As mentioned in the propylene oxidation chapter (Chapter 5), the mass transfer delay of the species compared to electrochemical signal is also relevant in this case. While the E_{ap} is measured via potentiostat, E_{CER} is calculated via MS signal for Cl_2, Therefore, there is a small time delay between these two potential.

In my opinion, the best way of comparing different catalysts' CER overpotential would be applying a constant current and waiting until the overpotential becomes stable. Thereafter, the overpotential measured by EC-MS could be compared at the same current density for each catalyst. I did not have time to do these experiments in this study.

Concluding this discussion, it is important to highlight another interesting observation: the Cl_2 signal increases over time at a constant potential. This finding is contrary to the expected behavior, as the overpotential for CER should decrease over time due to the rising Cl_2 concentration, resulting in a increase in E_{CER}. Furthermore, the total current density is decreasing with time. While the exact cause behind this phenomenon remains unclear, a potential explanation could be related to the saturation of the EC-MS system's stainless steel walls by Cl_2. Given that Cl_2 has a corrosive effect on stainless

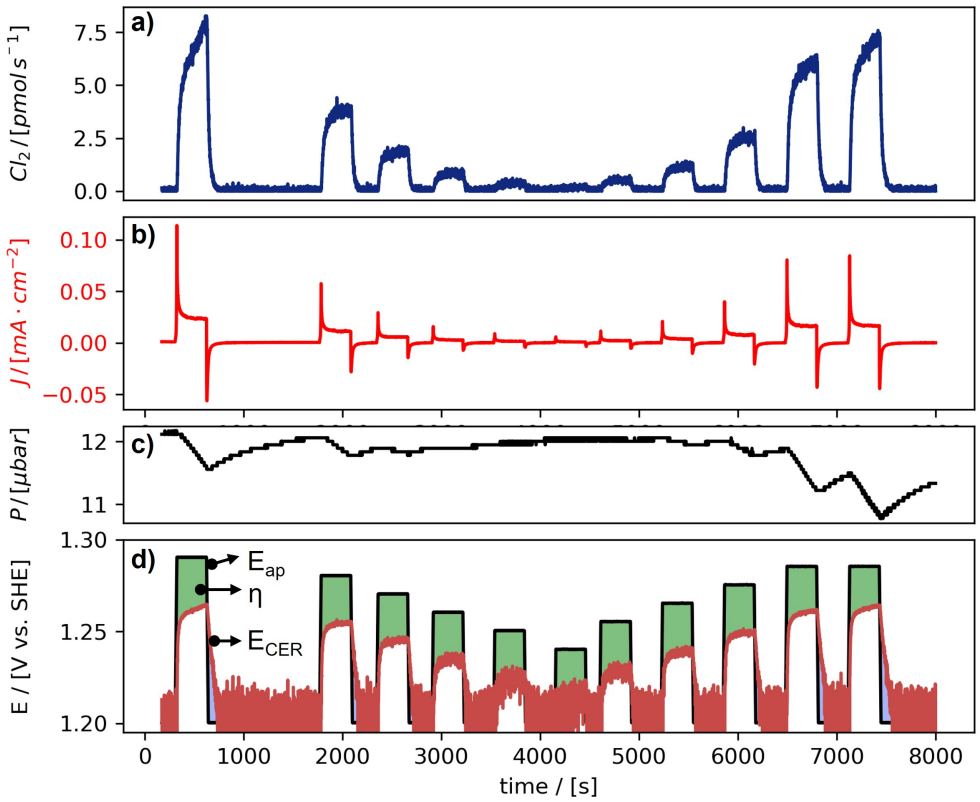

Figure 6.36 Calculation of real-time E_{CER} on Pt stub. (a) Cl_2 flux, (b) recorded current density, (c) MS pressure measured by ion gauge and corrected for He, (d) Applied potential recorded by potentiostat (black), E_{CER} calculated in real-time (red), real-time overpotential highlighted with green in between the E_{ap} and E_{CER}.

steel in the presence of water, it is possible that a portion of the Cl_2 continually reacts with the stainless steel components situated between the electrochemical cell and the MS. As more stainless steel surfaces become engaged with Cl_2, a reduced amount of Cl_2 reacts with the walls, leading to an observable and continuous increase in the Cl_2 signal. Notably, a similar increase in the Cl_2 signal has been reported in the literature for DEMS experiments lasting up to an hour [49].

6.5 Summary

In this chapter, I focused on assessing the catalytic activity of various catalysts for CER with high sensitivity using EC-MS. I covered experimental considerations specific to CER in EC-MS, evaluate the performance of different catalysts, and study the determination of overpotential concerning the dynamic equilibrium potential.

To summarize the conclusions regarding the experimental conditions, using Argon as a carrier gas resulted in overlooking in HCl (m/z =36) signal, as ^{36}Ar dominated the signal. Additionally, the attempt for preventing fragmentation of Cl_2 with soft ionization by reducing the ionization energy from 70 eV to 22 eV did not work resulted in reduced MS sensitivity. Thereby, this route is not pursued, and I suggest to use Helium as a carrier gas in CER studies with EC-MS. At the anodic potentials where excessive Cl_2 formation observed the MS signal of other masses decreased significantly compromising the sensitivity. Additionally, bubble formation due to Cl_2 generation lead to conductivity problems. Cl_2 calibration could not achieved with external calibration method due to the unavailability of sufficiently concentrated Cl_2 gas mixture in the market. Thereby, internal calibration is applied. Finally, detection potential is described and used as a criteria in the EC-MS system.

Secondly, activity evaluations on the RuO_2 on Ti, IrO_2 on GC, Pt stub, Pt on Ti, TiO_2/Pt on GC, and TiO_2 electrodes are successfully done. On the other hand, Pd stub, Au on GC, SnO_x on Ti, GeO_2 on GC samples are immediately dissolved during the anodic cycle of the CV. As a result, the detection potentials on all the electrodes were as close as 10 mV to each other making the comparison difficult. Therefore, the activity in terms of Cl_2 flux per cm^2 is compared at 1.30 V vs. SHE. Following activity trend for CER is observed: Pt on Ti > TiO_2/Pt on GC > Pt stub > RuO_2 > IrO_2 > TiO_2. Higher activity on Pt-based catalyst compared to RuO_2 and IrO_2 is investigated by comparing the CO stripping with and without Cl^- electrolytes. As a result, the CO oxidation potential is increased $\approx$ 600 mV when Cl^- exist in the electrolyte showing that Cl^- hinders adsorption of oxygen species to the surface. Therefore, the hypothesis for higher activity on Pt-based catalysts is established as surface might not be fully oxidized to PtO_2 as the we are in the low anodic potential range with EC-MS.Thereby,

the presence of Pt^0 species provides a faster route for CER which is supported by the literature.

Finally, different approaches for the equilibrium potential definition is given and the ambiguity in the field is addressed. Subsequently, the method based on the linear extrapolation of the polarization curve to zero current is applied. It is shown that this methods has limitations as depending on the selected potential range for extrapolation there is a great significant variation in the equilibrium potential.In conclusion, EC-MS is employed to continuously calculate the equilibrium potential in real-time by monitoring P_{Cl_2}. The increase in the equilibrium potential and the decrease in the overpotential over time is observed. The limitations of this method is clarified as following: it's less sensitive at lower Cl_2 concentrations, relies on precise calibration, and introduces a delay in calculating the equilibrium potential compared to the potential applied by the potentiostat, due to mass transport in the MS. As a final note, increase in Cl_2 signal over time is addressed. Although the reason remains unclear, a potential explanation due to the reaction of Cl_2 with stainless steel parts in the EC-MS is provided.

Chapter 7

General Conclusions & Outlook

Conclusions

In this chapter, I will provide the most important conclusions obtained from this thesis. The detailed conclusions are provided at the end of each chapter in the summary section. This thesis provided insights for two different reactions: (i) electrochemical propylene oxidation, (ii) CER by utilizing the advantages of EC-MS.

The significant outcomes of this study for the propylene oxidation can be summarized as:

- Especially in the organic synthesis reactions it is significant to detect products in real-time due to the unstable nature of many organic compounds. Overlooking at these compounds might result establishing the reaction mechanisms incorrectly. In Chapter 4, EC-MS is employed to detect PO for the first time, taking advantage of its increased sensitivity to volatile compounds, specifically identifying m/z = 58 as PO. Importantly, the study found that other potential compounds like acetone, propanal, and allyl alcohol could not be detected under the experimental conditions outlined. The presence of m/z = 31 during the reactions further confirmed this observation by distinguishing it from acetone and propanal.

- In Chapter 5, PO formation both on PtO_x and PdO_x is observed starting from 1.0 V to 1.6 V vs. RHE. On PtO_x, PO selectivity and activity continuously increased up to 1.6 V vs. RHE. On the other hand, on PdO_x the selectivity peaked

at 1.3 V, and the slope is changed in the MS-derived Tafel plot at 1.3 V. This results, supports the theoretical study on electrocatalytic propylene epoxidation suggesting the Langmuir-Hinselwood mechanism on PtO_2(110), and a change in the reaction mechanism from Langmuir-Hinselwood to Mars-Van Krevelen mechanism due to the oxygen vacancy formation at 1.23 V vs. RHE in PdO(110) [1].

- CO_2 formation during the switch from the anodic potential to the resting potential at the double-layer is attributed to the reduction of the surface oxide. This is utilized for *in-situ* surface oxide detection. Formation potential of the surface oxide on both catalysts coincides with the PO formation potential. Additionally, in the presence of C_3H_6 the oxidation potential for both catalysts shifted to more anodic potentials. This shows the importance of *in-situ* surface oxidation state measurement as it is a significant criterion while describing the reaction mechanism.

Conclusions for the CER study can be summarized as:

- EC-MS is used for the investigation of CER for the first time. The great sensitivity of EC-MS due to its 100% collection efficiency resulted in Cl_2 detection at anodic potentials as low as 1.25 V vs. SHE. This low detection potentials brought the questions about the equilibrium potential as all the defined equilibrium potentials in the literature were higher than the detection potential.

- Various catalysts are tested for CER, and it is shown that the activity for Pt-based catalysts is higher than for RuO_2 and IrO_2. This result contradicts the DFT calculations based on PtO_2. It is hypothesized that the presence of Cl^- prevents oxygen adsorption to surface and hinders the complete oxidation of Pt to PtO_2. As a result, the active site for CER changes from surface oxygen to Pt resulting in faster pathway for CER. The retardation of the adsorption of oxygen species is shown by the increase in the CO oxidation potential by $\approx$ 600 mV when Cl^- is present in the electrolyte.

- The ambiguity in the equilibrium potential definition in the literature is addressed. A new method for real-time equilibrium potential determination is introduced

based on *in-situ* measurement of the P_{Cl_2}. Therefore, the increase in the equilibrium potential and the decrease in the overpotential is observed. Finally, the limitations of this method is identified clearly.

Outlook

As a result of this study insights about two reactions are obtained. However, there are many questions remained unanswered. Additionally, new findings opened up new questions to be answered.

I would like to suggest some research ideas that I developed during my PhD for the future studies.

- First of all, electrochemical propylene epoxidation reaction should be investigated by considering all the reaction products to gain better understanding the overall reaction and the limitations. During the final stages of my PhD, I contemplated conducting the reaction at high current densities using a membrane-electrode-assembly cell. This approach could reduce water exposure since membrane-electrode-assemblies do not require flowing electrolyte. Additionally, inspired by a study on PO detection in cigarettes, I considered the possibility of trapping evaporated PO in an alternative organic solution, such as toluene, and quantifying it using *ex-situ* product analysis methods [102].

- Change in the reaction mechanism on PdO_x is observed during the experiments. With EC-MS, isotope labeling of oxygen can provide insights about the Mars-Van Krevelen mechanism and changes in the reaction mechanism depending on the potential can be presented clearly.

- As the surface oxidation coincides with the PO formation potentials the surface oxidation state might have a significant effect on propylene epoxidation. Therefore, *in-operando* surface characterization methods could be employed to describe the effect of surface oxidation state on propylene epoxidation.

- As a result of the chronoamperometry experiments, it is seen over time PO production rate decreases. This might be due to the conductivity loss as the oxide layer thickness increases, loss of active sites because of the catalyst dissolution, or

surface could be poisoned which is less likely as the operating potentials are fairly anodic. In the future studies, the deactivation mechanism could be understood, and new catalysts can be design depending on the reason. For example, RuO_2 or IrO_2 can be used as they are conductive oxides and more stable than Pt or Pd. These catalysts can be applied as a very thin layer on a catalyst known as having an optimal binding energy for propylene such as Pt. By this way, while optimizing the binding energy for high catalytic activity, catalyst stability and conductivity can be achieved.

- In CER studies, stability is as important as activity. Therefore, ICP-MS should be employed to the experiments to track dissolved metal amounts.

- In this thesis, superior activity of Pt-based catalyst is shown. Pt-based catalysts can be designed to prevent the oxygen binding to the surface to facilitate direct Cl adsorption to Pt as in [58]. Additionally, effect of covalent bond between the Pt and non-metallic element on catalyst stability can be investigated.

- The real-time equilibrium potential determination method could be performed with HER to minimize the limitations mentioned in Chapter 6. As it is also a reaction where the reversible reaction is fast enough change in the equilibrium potential due to H_2 concentration variation is expected. With HER, more accurate calibration with external calibration could be done. Additionally, the time response of H_2 is faster than Cl_2 with 1.7, and 72 respectively as calculated in Chapter 3 helping to minimize the mass transport delay between the equilibrium potential and applied potential.

References

[1] H. Li, C. S. Abraham, M. Anand, A. Cao, and J. K. Nørskov. "Opportunities and Challenges in Electrolytic Propylene Epoxidation". In: *Journal of Physical Chemistry Letters* 13 (9 2022), pp. 2057–2063. DOI: 10.1021/acs.jpclett.2c00257.

[2] *Maintaining a clear intention to keep 1.5C within reach UNFCCC*. URL: https://unfccc.int/maintaining-a-clear-intention-to-keep-15degc-within-reach.

[3] Z. Liu, Z. Deng, S. Davis, and P. Ciais. "Monitoring global carbon emissions in 2022". In: *Nature Reviews Earth & Environment 2023 4:4* 4 (4 2023), pp. 205–206. DOI: 10.1038/s43017-023-00406-z.

[4] R. Xia, S. Overa, and F. Jiao. "Emerging Electrochemical Processes to Decarbonize the Chemical Industry". In: (2022). DOI: 10.1021/jacsau.2c00138.

[5] *Renewables - Energy System - IEA*. URL: https://www.iea.org/energy-system/renewables.

[6] *Energy Statistics 2021*. 2022.

[7] *Renewable energy in the Danish energy system*. URL: https://en.energinet.dk/green-transition/renewable-energy-in-the-energy-system/.

[8] I. Chorkendorff and J. W. Niemantsverdriet. *Concepts of Modern Catalysis and Kinetics*. 2003. DOI: 10.1002/3527602658.

[9] M. Durovic, J. Hnat, and K. Bouzek. "Electrocatalysts for the hydrogen evolution reaction in alkaline and neutral media. A comparative review". In: *Journal of Power Sources* 493 (2021), p. 229708. DOI: 10.1016/j.jpowsour.2021.229708.

[10] A. J. Bard and L. R. Faulkner. *Electrochemical Methods: Fundamentals and Applications, 2nd Edition*. 2001.

[11] J. A. Z. Zeledón, A. Jackson, M. B. Stevens, G. A. Kamat, and T. F. Jaramillo. "Methods—A Practical Approach to the Reversible Hydrogen Electrode Scale". In: *Journal of The Electrochemical Society* 169 (6 2022), p. 066505. DOI: 10.1149/1945-7111/AC71D1.

[12] W. R. Leow, Y. Lum, A. Ozden, Y. Wang, D. H. Nam, B. Chen, J. Wicks, T. T. Zhuang, F. Li, D. Sinton, and E. H. Sargent. "Chloride-mediated selective electrosynthesis of ethylene and propylene oxides at high current density". In: *Science* 368 (6496 2020), pp. 1228–1233. DOI: 10.1126/science.aaz8459.

[13] *Petrochemicals Europe - European Market Overview*. 2020. URL: https://www.petrochemistry.eu/about-petrochemistry/petrochemicals-facts-and-figures/european-market-overview/.

[14] H. Baer, M. Bergamo, A. Forlin, L. H. Pottenger, and J. Lindner. "Propylene Oxide". In: *Ullmann's Encyclopedia of Industrial Chemistry* (2012). DOI: 10.1002/14356007.A22_239.PUB3.

[15] T. A. Nijhuis, M. Makkee, J. A. Moulijn, and B. M. Weckhuysen. "The production of propene oxide: Catalytic processes and recent developments". In: *Industrial and Engineering Chemistry Research* 45 (10 2006), pp. 3447–3459. DOI: 10.1021/ie0513090.

[16] A. Winiwarter, L. Silvioli, S. B. Scott, K. Enemark-Rasmussen, M. Sariç, D. B. Trimarco, P. C. Vesborg, P. G. Moses, I. E. Stephens, B. Seger, J. Rossmeisl, and I. Chorkendorff. "Towards an atomistic understanding of electrocatalytic partial hydrocarbon oxidation: Propene on palladium". In: *Energy and Environmental Science* 12 (3 2019), pp. 1055–1067. DOI: 10.1039/c8ee03426e.

[17] J. O. Bockris, H. Wroblowa, E. Gileadi, and B. J. Piersma. "Anodic oxidation of unsaturated hydrocarbons on platinized electrodes". In: *Transactions of the Faraday Society* 61 (1965), pp. 2531–2545. DOI: 10.1039/tf9656102531.

[18] H. Wise and L. Holbrook. "Electrooxidation of Olefins at a Silver Electrode". In: *Journal of Catalysis* 298 (38 1975), pp. 294–298.

[19] T. C. CHOU and J. C. CHANG. "Anodic-Oxidation of Propylene on a Screen Electrode". In: *Chemical Engineering Science* 35 (7 1980), pp. 1581–1590.

[20] K. Scott, C. Odouza, and W. Hui. "Pilot scale electrosynthesis of alkene oxides by direct and indirect oxidation in a sieve plate electrochemical reactor". In: *Chemical Engineering Science* 47 (9-11 1992), pp. 2957–2962. DOI: 10.1016/0009-2509(92)87158-M.

[21] G. R. Stafford. "The electrogenerative partial oxidation of propylene". In: *Electrochimica Acta* 32 (8 1987), pp. 1137–1143. DOI: 10.1016/0013-4686(87)80024-5.

[22] K. Otsuka, Y. Shimizu, I. Yamanaka, and T. Komatsu. "Wacker Type and Pi-Allyl Type Oxidations Of Propylene Controlled By Fuel Cell System In The Gas Phase". In: *Catalysis Letters* 3 (1989), pp. 365–370.

[23] K. Otsuka, T. Ushiyama, I. Yamanaka, and K. Ebitani. "Electrocatalytic synthesis of propylene oxide during water electrolysis". In: *Journal of Catalysis* 157 (2 1995), pp. 450–460. DOI: 10.1006/jcat.1995.1310.

[24] L. Silvioli, A. Winiwarter, S. B. Scott, I. E. Castelli, P. G. Moses, I. Chorkendorff, B. Seger, and J. Rossmeisl. "Rational Catalyst Design for Higher Propene Partial Electro-oxidation Activity by Alloying Pd with Au". In: *J. Phys. Chem. C* 2022 (2022), pp. 126–14487. DOI: 10.1021/acs.jpcc.1c10095.

[25] S. Koroidov, A. Winiwarter, O. Diaz-Morales, M. Görlin, J. H. Stenlid, H.-Y. Wang, M. Börner, C. M. Goodwin, M. Soldemo, L. G. M. Pettersson, J. Rossmeisl, T. Hansson, I. Chorkendorff, and A. Nilsson. "Chemisorbed oxygen or surface oxides steer the selectivity in Pd electrocatalytic propene oxidation observed by operando Pd L-edge X-ray absorption spectroscopy". In: *Catalysis Science & Technology* (2021). DOI: 10.1039/d0cy02134b.

[26] X.-C. Liu, T. Wang, Z.-M. Zhang, C.-H. Yang, L.-Y. Li, S. Wu, S. Xie, G. Fu, Z.-Y. Zhou, and S.-G. Sun. "Reaction Mechanism and Selectivity Tuning of Propene Oxidation at the Electrochemical Interface". In: *Journal of the American Chemical Society* (2022). DOI: 10.1021/jacs.2c09105.

[27] R. P. H. Jong, E Dubbelman, and G Mul. "Electro-oxidation of propylene by palladium functionalized titanium hollow fibre electrodes". In: (2022). DOI: 10.1016/j.jcat.2022.10.007.

[28] S. Iguchi, M. Kataoka, R. Hoshino, and I. Yamanaka. "Direct epoxidation of propylene with water at a PtOx anode using a solid-polymer-electrolyte electrolysis cell". In: *Catalysis Science & Technology* 12 (2 2022), pp. 469–473. DOI: 10.1039/D1CY01888D.

[29] J. A. M. Leduc. *Electrochemical process for the production of organic oxides*. 1966.

[30] V. M. Schmidt and E. Pastor. "Electro-oxidation of propene on gold in acid solution studied by DEMS and FTIRS". In: *Journal of Electroanalytical Chemistry* 401 (1-2 1996), pp. 155–161. DOI: 10.1016/0022-0728(95)04299-7.

[31] J. S. Jirkovský, M. Busch, E. Ahlberg, I. Panas, and P. Krtil. "Switching on the electrocatalytic ethene epoxidation on nanocrystalline RuO2". In: *Journal of the American Chemical Society* 133 (15 2011), pp. 5882–5892. DOI: 10.1021/ja109955w.

[32] K. Otsuka, lchiro Yamanaka, K. Hosokawa, A Clegg, M Blaskiewicz, J. N. Cuzzi, J. D. Scargle, J. P. for discussions, L Dones, C. D. Murray, P. D. Nicholson, and C. C. P. for comments. "7. Terrile, R. J. in /AU Colloq". In: *16. Kolvoord, R. A. & Burns, J. A. Bull. Am. Astr. Soc* 2 (12 1981), pp. 207–218.

[33] Y. Wang, Y. Liu, D. Wiley, S. Zhao, and Z. Tang. "Recent advances in electrocatalytic chloride oxidation for chlorine gas production". In: *Journal of Materials Chemistry A* 9 (35 2021), pp. 18974–18993. DOI: 10.1039/d1ta02745j.

[34] H. Dong, W. Yu, and M. R. Hoffmann. “Published as part of The Journal of Physical Chemistry virtual special issue "125 Years of The Journal of Physical Chemistry". Cite This”. In: *J. Phys. Chem. C* 125 (2021). DOI: 10.1021/acs.jpcc.1c05671.

[35] R. K. B. Karlsson and A. Cornell. “Selectivity between Oxygen and Chlorine Evolution in the Chlor-Alkali and Chlorate Processes”. In: (2016). DOI: 10.1021/acs.chemrev.5b00389.

[36] D. Wintrich, D. Öhl, S. Barwe, A. Ganassin, S. Möller, T. Tarnev, A. Botz, A. Ruff, J. Clausmeyer, J. Masa, and W. Schuhmann. “Enhancing the Selectivity between Oxygen and Chlorine towards Chlorine during the Anodic Chlorine Evolution Reaction on a Dimensionally Stable Anode”. In: *ChemElectroChem* 6 (12 2019), pp. 3108–3112. DOI: 10.1002/celc.201900784.

[37] M. Deborde and U. von Gunten. “Reactions of chlorine with inorganic and organic compounds during water treatment—Kinetics and mechanisms: A critical review”. In: *Water Research* 42 (1-2 2008), pp. 13–51. DOI: 10.1016/J.WATRES.2007.07.025.

[38] H. A. Hansen, I. C. Man, F. Studt, F. Abild-Pedersen, T. Bligaard, and J. Rossmeisl. “Electrochemical chlorine evolution at rutile oxide (110) surfaces”. In: *Physical Chemistry Chemical Physics* 12 (1 2010), pp. 283–290. DOI: 10.1039/b917459a.

[39] K. S. Exner, J. Anton, T. Jacob, H. Over, K. S. Exner, H Over, J Anton, and T Jacob. “Controlling Selectivity in the Chlorine Evolution Reaction over RuO2-Based Catalysts”. In: *Angewandte Chemie International Edition* 53 (41 2014), pp. 11032–11035. DOI: 10.1002/ANIE.201406112.

[40] K. S. Exner and H. Over. “Beyond the Rate-Determining Step in the Oxygen Evolution Reaction over a Single-Crystalline IrO 2 (110) Model Electrode: Kinetic Scaling Relations”. In: (2019). DOI: 10.1021/acscatal.9b01564.

[41] K. S. Exner. “Beyond thermodynamic-based material-screening concepts: Kinetic scaling relations exemplified by the chlorine evolution reaction over transition-metal oxides”. In: *Electrochimica Acta* 334 (2020). DOI: 10.1016/j.electacta.2019.135555.

[42] K. S. Exner. “Design criteria for the competing chlorine and oxygen evolution reactions: avoid the OCl adsorbate to enhance chlorine selectivity”. In: *Physical Chemistry Chemical Physics* 22 (39 2020), pp. 22451–22458. DOI: 10.1039/d0cp03667f.

[43] K. S. Exner. “Overpotential-Dependent Volcano Plots to Assess Activity Trends in the Competing Chlorine and Oxygen Evolution Reactions”. In: *CHEMELECTROCHEM* 7 (6 2020), pp. 1448–1455. DOI: 10.1002/celc.202000120.

[44] Y. Yang, J. Shin, J. T. Jasper, and M. R. Hoffmann. "Multilayer Heterojunction Anodes for Saline Wastewater Treatment: Design Strategies and Reactive Species Generation Mechanisms". In: (2016). DOI: 10.1021/acs.est.6b00688.

[45] I. A. Moreno-Hernandez, B. S. Brunschwig, and N. S. Lewis. "Crystalline nickel, cobalt, and manganese antimonates as electrocatalysts for the chlorine evolution reaction". In: *Energy & Environmental Science* 12 (4 2019), pp. 1241–1248. DOI: 10.1039/c8ee03676d.

[46] K. M. Macounová, R. K. Pittkowski, R. Nebel, A. Zitolo, and P. Krtil. "Selectivity of Ru-rich Ru-Ti-O oxide surfaces in parallel oxygen and chlorine evolution reactions". In: *Electrochimica Acta* 427 (2022), p. 140878. DOI: 10.1016/J.ELECTACTA.2022.140878.

[47] E. Kuznetsova, V. Petrykin, S. Sunde, and P. Krtil. "Selectivity of Nanocrystalline IrO2-Based Catalysts in Parallel Chlorine and Oxygen Evolution". In: *Electrocatalysis* 6 (2 2015), pp. 198–210. DOI: 10.1007/s12678-014-0233-y.

[48] J. G. Vos and M. T. Koper. "Measurement of competition between oxygen evolution and chlorine evolution using rotating ring-disk electrode voltammetry". In: *Journal of Electroanalytical Chemistry* (2018). DOI: 10.1016/j.jelechem.2017.10.058.

[49] A. R. Zeradjanin, N. Menzel, W. Schuhmann, and P. Strasser. "On the faradaic selectivity and the role of surface inhomogeneity during the chlorine evolution reaction on ternary Ti-Ru-Ir mixed metal oxide electrocatalysts". In: *Phys. Chem. Chem. Phys* 16 (2014), p. 13741. DOI: 10.1039/c4cp00896k.

[50] I. Sohrabnejad-Eskan, A. Goryachev, K. S., L. A. Kibler, E. J. Hensen, J. P. Hofmann, and H. Over. "Temperature-Dependent Kinetic Studies of the Chlorine Evolution Reaction over RuO2(110) Model Electrodes". In: *ACS Catalysis* 7 (4 2017), pp. 2403–2411. DOI: 10.1021/acscatal.6b03415.

[51] J. G. Vos, T. A. Wezendonk, A. W. Jeremiasse, and M. T. M. Koper. "MnO x /IrO x as Selective Oxygen Evolution Electrocatalyst in Acidic Chloride Solution". In: (2018). DOI: 10.1021/jacs.8b05382.

[52] J. G. Vos, A Venugopal, W. A. Smith, and M. T. M. Koper. "Competition and selectivity during parallel evolution of bromine, chlorine and oxygen on IrOx electrodes". In: *Journal of Catalysis* 389 (2020), pp. 99–110. DOI: 10.1016/j.jcat.2020.05.024.

[53] J. G. Vos, Z. Liu, F. D. Speck, N. Perini, W. Fu, S. Cherevko, and M. T. Koper. "Selectivity Trends between Oxygen Evolution and Chlorine Evolution on Iridium-Based Double Perovskites in Acidic Media". In: *ACS Catalysis* 9 (9 2019), pp. 8561–8574. DOI: 10.1021/acscatal.9b01159.

[54] Y. Liu, C. Li, C. Tan, Z. Pei, T. Yang, S. Zhang, Q. Huang, Y. Wang, Z. Zhou, X. Liao, J. Dong, H. Tan, W. Yan, H. Yin, Z. Q. Liu, J. Huang, and S. Zhao. "Electrosynthesis of chlorine from seawater-like solution through single-atom catalysts". In: *Nature Communications 2023 14:1* 14 (1 2023), pp. 1–13. DOI: 10.1038/s41467-023-38129-w.

[55] J. Cho, T. Lim, H. Kim, L. Meng, J. Kim, S. Lee, J. H. Lee, G. Y. Jung, K. S. Lee, F. Viñes, F. Illas, K. S. Exner, S. H. Joo, and C. H. Choi. "Importance of broken geometric symmetry of single-atom Pt sites for efficient electrocatalysis". In: *Nature Communications 2023 14:1* 14 (1 2023), pp. 1–10. DOI: 10.1038/s41467-023-38964-x.

[56] Y. Yao, L. Zhao, J. Dai, J. Wang, C. Fang, G. Zhan, Q. Zheng, W. Hou, L. Zhang, Y Yao, L Zhao, J Dai, J Wang, Q Zheng, W Hou, L Zhang, C Fang, and G Zhan. "Single Atom Ru Monolithic Electrode for Efficient Chlorine Evolution and Nitrate Reduction". In: *Angewandte Chemie International Edition* 61 (41 2022), e202208215. DOI: 10.1002/ANIE.202208215.

[57] J. Yang, W.-H. Li, K. Xu, S. Tan, D. Wang, Y. Li, J Yang, W h Li, K Xu, D Wang, Y Li, and S Tan. "Regulating the Tip Effect on Single-Atom and Cluster Catalysts: Forming Reversible Oxygen Species with High Efficiency in Chlorine Evolution Reaction Zuschriften". In: 134 (2022), pp. 202200366–202200367. DOI: 10.1002/anie.202200366.

[58] T Lim, G. Y. Jung, J. H. Kim, S. O. Park, J Park, Y. T. Kim, S. J. Kang, H. Y. Jeong, S. K. Kwak, and S. H. Joo. "Atomically dispersed Pt-N-4 sites as efficient and selective electrocatalysts for the chlorine evolution reaction". In: *Nature Communications* 11 (1 2020). DOI: 10.1038/s41467-019-14272-1.

[59] X. L. Zhu, P Wang, Z. Y. Wang, Y. Y. Liu, Z. K. Zheng, Q. Q. Zhang, X. Y. Zhang, Y Dai, M. H. Whangbo, and B. B. Huang. "Co3O4 nanobelt arrays assembled with ultrathin nanosheets as highly efficient and stable electrocatalysts for the chlorine evolution reaction". In: *Journal of Materials Chemistry A* 6 (26 2018), pp. 12718–12723. DOI: 10.1039/c8ta03689f.

[60] J. Yang, W.-H. Li, H.-T. Tang, Y.-M. Pan, D. Wang, and Y. Li. "CO 2-mediated organocatalytic chlorine evolution under industrial conditions". In: *Nature* | 617 (2023). DOI: 10.1038/s41586-023-05886-z.

[61] W. Lee, T. Lee, S. Kim, S. Bae, J. Yoon, and K. Cho. "Descriptive Role of Pt/PtOxRatio on the Selective Chlorine Evolution Reaction under Polarity Reversal as Studied by Scanning Electrochemical Microscopy". In: *ACS Applied Materials and Interfaces* 13 (29 2021), pp. 34093–34101. DOI: 10.1021/acsami.1c06187.

[62] B. Conway and D. Novak. "Electrocatalytic effect of the oxide film at Pt anodes on Cl• recombination kinetics in chlorine evolution". In: *Journal of Electroanalytical Chemistry and Interfacial Electrochemistry* 99.2 (1979), pp. 133–156. DOI: https://doi.org/10.1016/S0022-0728(79)80243-0.

[63] A. T. Kuhn and C. J. Mortimer. “The Kinetics of Chlorine Evolution and Reduction on Titanium-Supported Metal Oxides Especially RuO2 and IrO2”. In: *Journal of The Electrochemical Society* 120 (2 1973), p. 231. DOI: 10.1149/1.2403425/META.

[64] R. S. Patil, V. A. Juvekar, and V. M. Naik. “Oxidation of chloride ion on platinum electrode: Dynamics of electrode passivation and its effect on oxidation kinetics”. In: *Industrial and Engineering Chemistry Research* 50 (23 2011), pp. 12946–12959.

[65] C. E. Finke, S. T. Omelchenko, J. T. Jasper, M. F. Lichterman, C. G. Read, N. S. Lewis, and M. R. Hoffmann. “Enhancing the activity of oxygen-evolution and chlorine-evolution electrocatalysts by atomic layer deposition of TiO2”. In: *Energy & Environmental Science* 12 (1 2019), pp. 358–365. DOI: 10.1039/c8ee02351d.

[66] A. Winiwarter. “The Catalysis of the Selective Electrooxidation of Hydrocarbons”. 2019.

[67] R. Li, H. Mao, J. Zhang, T. Huang, and A. Yu. “Rapid synthesis of porous Pd and PdNi catalysts using hydrogen bubble dynamic template and their enhanced catalytic performance for methanol electrooxidation”. In: *Journal of Power Sources* 241 (2013), pp. 660–667. DOI: 10.1016/j.jpowsour.2013.05.032.

[68] G. M. McCracken. “The behaviour of surfaces under ion bombardment”. In: *Reports on Progress in Physics* 38 (2 1975). DOI: 10.1088/0034-4885/38/2/002.

[69] N. Erdman, D. C. Bell, and R. Reichelt. *Scanning electron microscopy*. 2019. DOI: 10.1007/978-3-030-00069-1_5.

[70] E. Taglauer. “Ion scattering spectroscopy”. In: *Surface Characterization: A User’s Sourcebook* (2007), pp. 190–204. DOI: 10.1002/9783527612451.CH12.

[71] D. B. Trimarco, S. B. Scott, A. H. Thilsted, J. Y. Pan, T. Pedersen, O. Hansen, I. Chorkendorff, and P. C. Vesborg. “Enabling real-time detection of electrochemical desorption phenomena with sub-monolayer sensitivity”. In: *Electrochimica Acta* 268 (2018), pp. 520–530. DOI: 10.1016/j.electacta.2018.02.060.

[72] F. Scholz. *Electroanalytical methods: Guide to experiments and applications*. 2010. DOI: 10.1007/978-3-642-02915-8.

[73] *Basics of EIS: Electrochemical Research-Impedance Gamry Instruments*. URL: https://www.gamry.com/application-notes/EIS/basics-of-electrochemical-impedance-spectroscopy/.

[74] N. Elgrishi, K. J. Rountree, B. D. McCarthy, E. S. Rountree, T. T. Eisenhart, and J. L. Dempsey. “A Practical Beginner’s Guide to Cyclic Voltammetry”. In: *Journal of Chemical Education* 95 (2 2018). DOI: 10.1021/acs.jchemed.7b00361.

[75] S. Anantharaj, P. E. Karthik, and S. Noda. “The Significance of Properly Reporting Turnover Frequency in Electrocatalysis Research”. In: *Angewandte Chemie - International Edition* 60 (43 2021), pp. 23051–23067. DOI: 10.1002/ANIE.202110352.

[76] M Łukaszewski, M Soszko, and A Czerwiński. “ELECTROCHEMICAL SCIENCE Electrochemical Methods of Real Surface Area Determination of Noble Metal Electrodes-an Overview”. In: *Int. J. Electrochem. Sci* 11 (2016), pp. 4442–4469. DOI: 10.20964/2016.06.71.

[77] D. B. Trimarco. “Real-time detection of sub-monolayer desorption phenomena during electrochemical reactions: Instrument development and applications”. In: (2017).

[78] J. H. Gross. *Mass Spectrometry/ A Textbook Third Edition*. Vol. 1040. 2017.

[79] C. L. Yaws. “Diffusion Coefficient in Water – Organic Compounds”. In: *Transport Properties of Chemicals and Hydrocarbons* (2009), pp. 502–593. DOI: 10.1016/B978-0-8155-2039-9.50017-X.

[80] E. L. Cussler. *Diffusion: Mass Transfer in Fluid Systems, 2nd edition*. 1997.

[81] R. Sander. *Henry’s Law Constants*. Ed. by P. Linstrom and W. Mallard. DOI: https://doi.org/10.18434/T4D303.

[82] R. Grinham and A. Chew. “Gas Correction Factors for Vacuum Pressure Gauges: Factors Affecting the Sensitivity of Ionisation and Thermal Type Vacuum Gauges with Different Gases”. In: *Vakuum in Forschung und Praxis* 29 (2 2017), pp. 25–30. DOI: 10.1002/VIPR.201700640.

[83] J. F. O’Hanlon. *A Users Guide to Vacuum Technology*. 2003, pp. 94–97. DOI: 10.1002/0471467162.

[84] *Gas Correction Factors for Ionization Vacuum Gauges*. URL: https://www.mks.com/n/gas-correction-factors-for-ionization-vacuum-gauges.

[85] M. Ko, Y. Kim, J. Woo, B. Lee, R. Mehrotra, P. Sharma, J. Kim, S. W. Hwang, H. Y. Jeong, H. Lim, S. H. Joo, J.-W. Jang, and J. H. Kwak. “Direct propylene epoxidation with oxygen using a photo-electro-heterogeneous catalytic system”. In: *Nature Catalysis* 5 (2022), pp. 37–44. DOI: 10.1038/s41929-021-00724-9.

[86] W. E. Wallace. *NIST Mass Spectrometry Data Center "Mass Spectra"*. Ed. by P. Linstrom and W. Mallard. DOI: https://doi.org/10.18434/T4D303.

[87] A. Arvajová, P. Kočí, V. Schmeißer, and M. Weibel. “The impact of CO and C 3 H 6 pulses on PtO x reduction and NO oxidation in a diesel oxidation catalyst”. In: *Applied Catalysis B: Environmental* 181 (2016), pp. 644–650. DOI: 10.1016/j.apcatb.2015.08.004.

[88] S. B. Scott, J. Kibsgaard, P. C. Vesborg, and I. Chorkendorff. "Tracking oxygen atoms in electrochemical CO oxidation - Part II: Lattice oxygen reactivity in oxides of Pt and Ir". In: *Electrochimica Acta* 374 (2021), p. 137844. DOI: 10.1016/J.ELECTACTA.2021.137844.

[89] Y.-R. Zheng, J. Vernieres, Z. Wang, K. Zhang, D. Hochfilzer, K. Krempl, T.-W. Liao, F. Presel, T. Altantzis, J. Fatermans, S. B. Scott, N. M. Secher, C. Moon, P. Liu, S. Bals, S. V. Aert, A. Cao, M. Anand, J. K. Nørskov, J. Kibsgaard, and I. Chorkendorff. "Monitoring oxygen production on mass-selected iridium-tantalum oxide electrocatalysts". In: (). DOI: 10.1038/s41560-021-00948-w.

[90] K. Krempl, D. Hochfilzer, S. B. Scott, J. Kibsgaard, P. C. Vesborg, O. Hansen, and I. Chorkendorff. "Dynamic Interfacial Reaction Rates from Electrochemistry-Mass Spectrometry". In: *Analytical Chemistry* 93 (18 2021), pp. 7022–7028. DOI: 10.1021/acs.analchem.1c00110.

[91] Z. B. Alfassi. "On the Normalization of a Mass Spectrum for Comparison of Two Spectra". In: (2004). DOI: 10.1016/j.jasms.2003.11.008.

[92] S Díaz-Coello, G García, M. C. Ar, and E Pastor. "Precise determination of Tafel slopes by DEMS. Hydrogen evolution on tungsten-based catalysts in alkaline solution". In: (2019). DOI: 10.1016/j.ijhydene.2019.02.151.

[93] A. R. Zeradjanin, N. Menzel, P. Strasser, and W. Schuhmann. "Role of Water in the Chlorine Evolution Reaction at RuO2-Based Electrodesa-Understanding Electrocatalysis as a Resonance Phenomenon". In: *ChemSusChem* 5 (10 2012), pp. 1897–1904. DOI: 10.1002/cssc.201200193.

[94] C. Batchelor-Mcauley. "Defining the onset potential". In: (2022). DOI: 10.1016/j.coelec.2022.101176.

[95] D. Macdougall, D. P.-C. Francis, J Amore, G. V. Cox, D. G. Crosby, F. L. Estes, D. H. Freeman, W. E. Gibbs, G. E. Gordon, L. H. K. Manager, J. Lai, D. Chemical, U. S. A. Nina, I Mcclelland, W. F. Phillips, R. B. Pojasek, R. E. Sievers, D. C. Wimert, and R. Libby. "Guidelines for Data Acquisition and Data Quality Evaluation in Environmental Chemistry". In: *Anal. Chem* 52 (1980), pp. 2242–2249.

[96] V. Lopez-Avila, P. J. Roach, and R. Urdahl. "Environmental Applications of Soft Ionization with GC–TOFMS and GC–QTOFMS". In: *Comprehensive Analytical Chemistry* 61 (2013), pp. 325–346. DOI: 10.1016/B978-0-444-62623-3.00014-9.

[97] M. Pourbaix and J. Burbank. "Atlas D-Equilibres Electrochimiques". In: *Journal of The Electrochemical Society* (1964). DOI: 10.1149/1.2426051.

[98] J. H. Huang, M. J. Hou, J. Y. Wang, X Teng, Y. L. Niu, M. Z. Xu, and Z. F. Chen. "RuO2 nanoparticles decorate belt-like anatase TiO2 for highly efficient chlorine evolution". In: *ELECTROCHIMICA ACTA* 339 (2020). DOI: 10.1016/j.electacta.2020.135878.

[99] N. Menzel, E. Ortel, K. Mette, R. Kraehnert, and P. Strasser. “Dimensionally stable Ru/Ir/TiO2-anodes with tailored mesoporosity for efficient electrochemical chlorine evolution”. In: *ACS Catalysis* 3 (6 2013), pp. 1324–1333. DOI: 10.1021/CS4000238.

[100] E. Guerrini, A. E. Valerio, C. Ae, and S. Trasatti. “Surface and electrocatalytic properties of well-defined and vicinal RuO2 single crystal faces”. In: (). DOI: 10.1007/s10008-004-0602-1.

[101] W. M. Haynes, ed. *CRC Handbook of Chemistry and Physics*. 95th ed. Boca Raton, Fla.: CRC Press/Taylor and Francis, 2014.

[102] J. Diekmann, M. Douda, and K. Rustemeier. “Rapid and Sensitive Method for the Determination of Propylene Oxide in Cigarette Mainstream Smoke by Gas Chromatography–Mass Spectrometry*”. In: *Journal of Chromatographic Science* 44 (2006).

Appendix A

Supporting Information

A.1 Materials

In Chapter 4 and 5, the electrolyte for propylene epoxidation, 0.1 M $HClO_4$ is prepared with 70% $HClO_4$ (Suprapur, Merck KG) and ultrapure water (Millipore, Synergy UV system). The electrolyte was purged with Ar(5.0, AGA), propene (4.0, BOC), and CO (5.0, AGA). The catalyst inks for Pd and Pt drop-casting are prepared by mixing 20 mg of Pt black (HiSPECTM 1000, Thermo Scientific TM) or Pd black (99.9%, Thermo ScientificTM), 2 ml isopropyl alcohol ($\geq$ 99.8%, EMSURE, Supelco), 2 ml ultrapure water (Millipore, Synergy UV system), and 80 µl perfluorinated resin solution containing NafionTM 1100W (5wt.% in lower aliphatic alcohols and water, Sigma Aldrich). The ink is dropped on a clean glassy carbon substrate with a heating plate at 80°C.

In Chapter 6, the electrolyte for CER, 0.1 M $HClO_4$ + 1 M NaCl is prepared with 70% $HClO_4$ (Suprapur, Merck KG) and ultrapure water (Millipore, Synergy UV system), and NaCl (> 99.5% (AT) BioXtra, Sigma Aldrich).

A.2 Mass Spectrometer Settings

Both for electrochemical propylene oxidation and chlorine evolution EC-MS instrument (SpectroInlets, ApS) is used. However, for the propylene oxidation experiments EC-MS

in DTU, for CER EC-MS in Spectro Inlets, ApS is used. Both reactions are conducted with 70 eV ionization energy and 80 V anode voltage. Secondary electron multiplier tuned in air to obtain m/z = 28 (N_2) signal to be at 10^{-7} A. For propylene oxidation dwell time 128 ms is used for increased sensitivity. For CER, dwell time 32 ms is used.

A.3 Electrochemical Propylene Epoxidation

In the following section additional figures for the electrochemical propylene epoxidation project is provided.

The following SEM images are taken with FEI Quanta 200 cryo ESEM. Everhart-Thornley detector is used. 15 kV electron beam acceleration voltage is set for all the images.

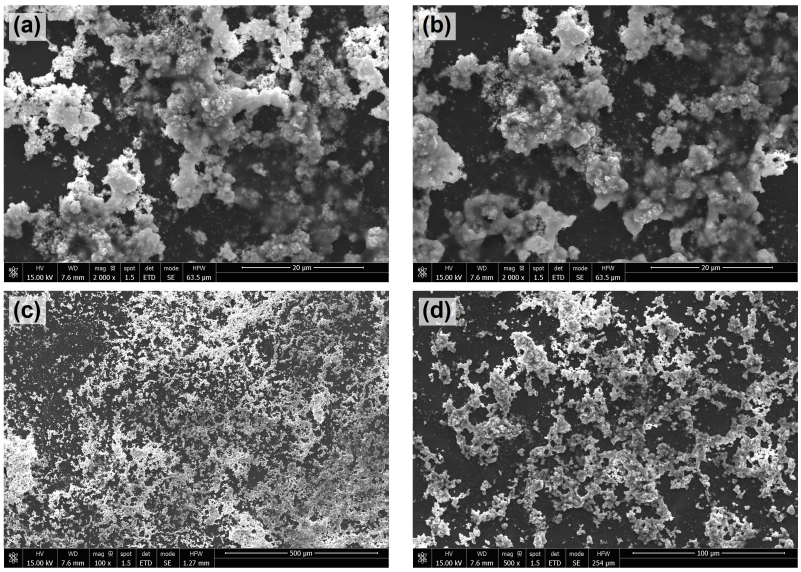

Figure A.1 SEM images on drop casted Pd catalyst on GC substrate showing the the coating is not homogeneously distributed and GC is exposed.

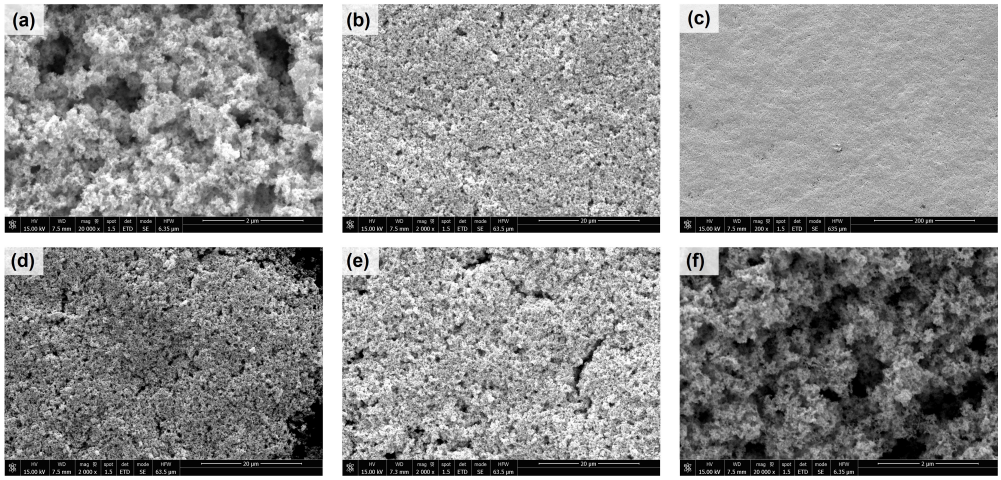

Figure A.2 SEM images for drop-casted Pt catalyst on GC substrate showing that coating has a good coverage on the surface. Morphology presents that the surface is rough to provide high surface area.

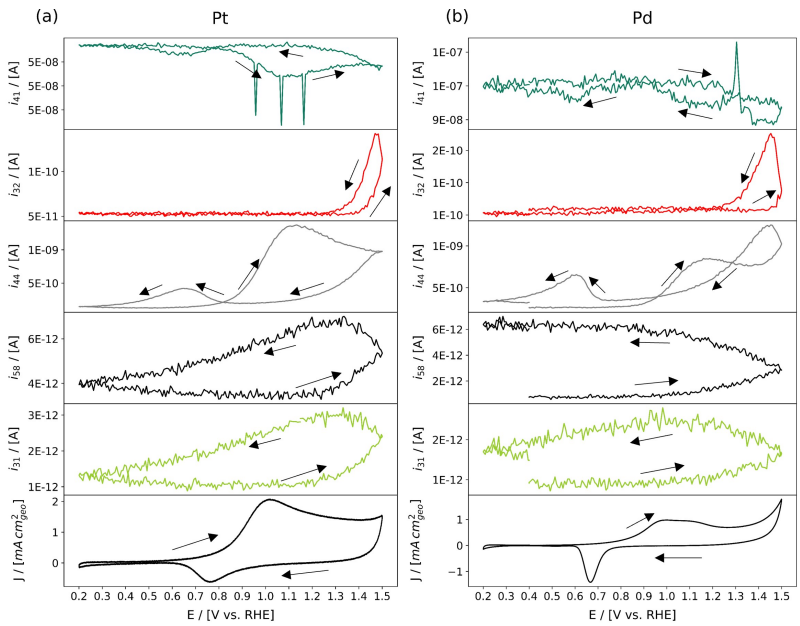

Figure A.3 Extended MSCV previously given in Figure 5.1 including m/z=58, and m/z=31 while purging C_3H_6 representing the increase in PO related mass ion currents with anodic scan on (a) Pt and (b) Pd.

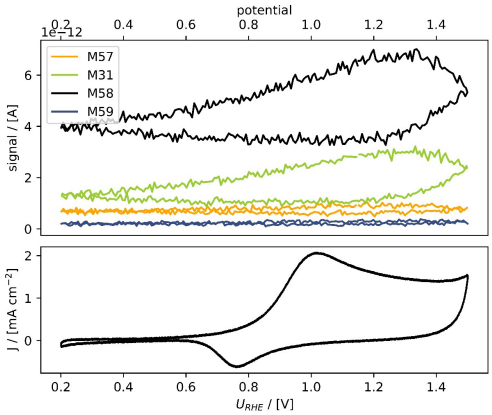

Figure A.4 PO isotopes (m/z = 58, 57, 59) and fragments (m/z=31) while scanning the potential in between 0.2 V - 1.5 V vs. RHE on Pt.

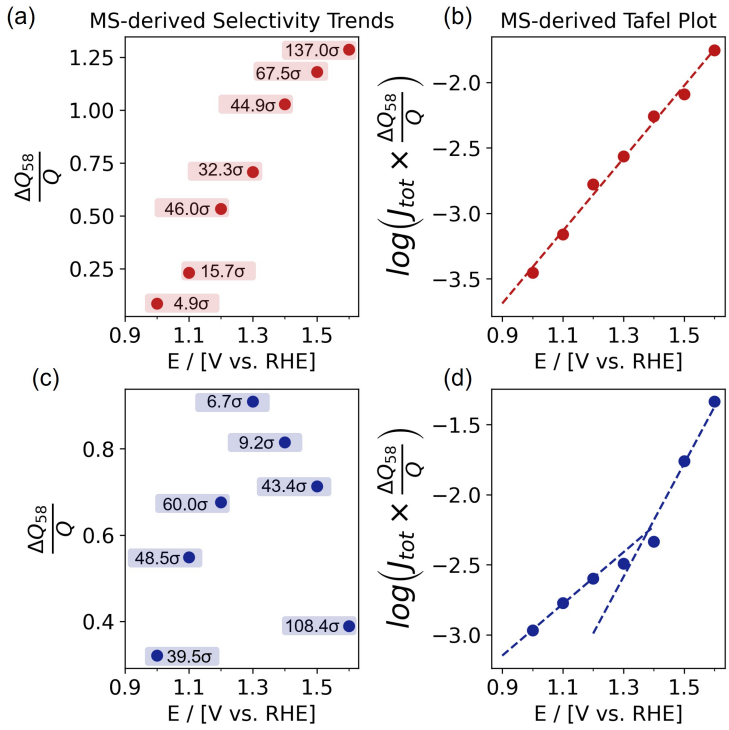

Figure A.5 MS derived selectivity trends (a) for Pt and (c) for Pd, and activity trends (b) for Pt and (d) for Pd including the signal to noise ratio for each data point.

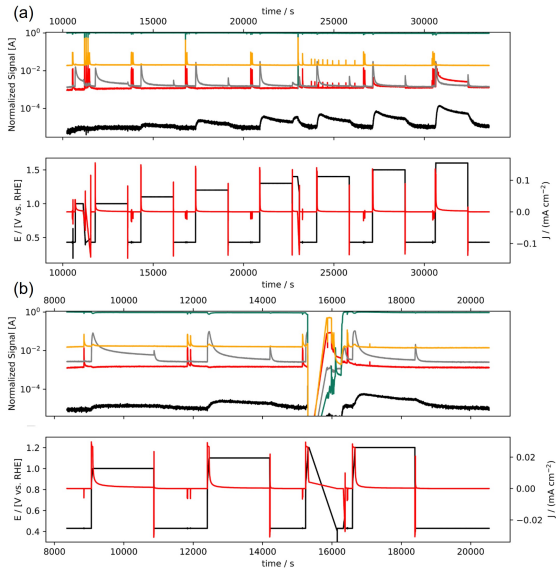

Figure A.6 30 minutes CA experiments conducted on PtO_x. (a) Potentials tested from 1.0 to 1.6 V vs. RHE, (b) potentials tested from 1.0 to 1.2 V vs. RHE. The disruption of the MS signal is due to the sudden shut down of the filament.

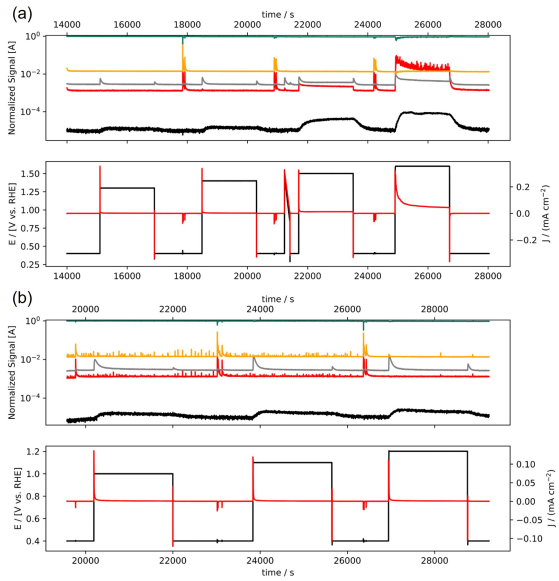

Figure A.7 30 minutes CA experiments conducted on PdO_x. (a) Potentials tested from 1.3 to 1.6 V vs. RHE, (b) potentials tested from 1.0 to 1.2 V vs. RHE.

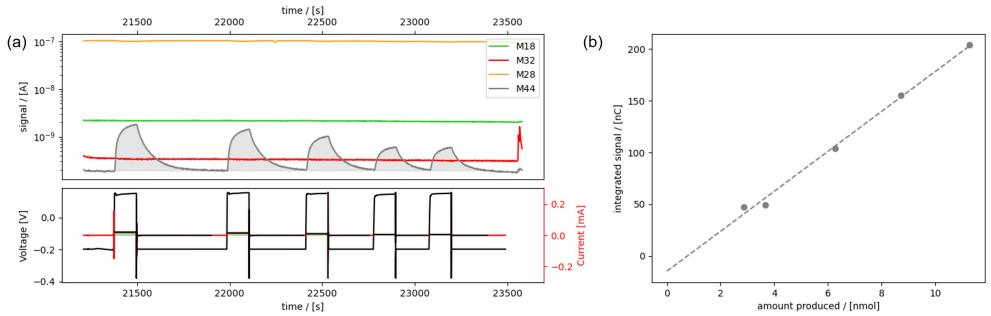

Figure A.8 Example CO_2 calibration curve obtained with internal calibration used for the quantification of CO_2 formed during the reduction of surface oxide with EC-MS. (a) CO oxidation to CO_2 at constant currents. The whole CO_2 signal obtained as a result of CP is integrated to obtain integrated signal which is highlighted. (b) The calibration curve is obtained via plotting the integrated signal vs. amount produced which is calculated by assuming 100% Faradaic efficiency. Slope of this plot gives the calibration constant.

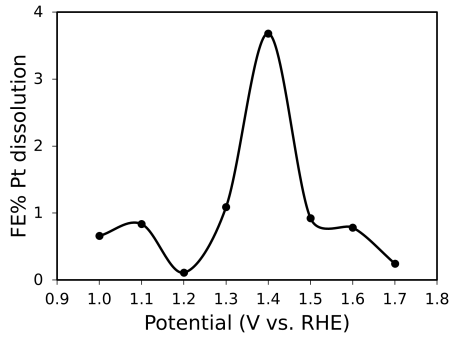

Figure A.9 Faradaic efficiency for Pt dissolution during the electrochemical propylene oxidation reaction with EC-MS on a drop-casted Pt sample. After the application of each potential 1 mL sample has taken from the EC-MS and dissolved Pt rate is determined with ICP-MS analysis. Initially, it is aimed to conduct this for each experiment, and samples were Pd tests are also taken. However, due to the disfunction of ICP-MS at that time, analysis could not be conducted for Pd.

A.4 Chlorine Evolution Reaction

In this section additional figures for chlorine evolution project is provided.

A.4.1 Characterization of the Catalysts

Catalyst prepared for CER is characterized in this section with XPS and ISS with ThermoScientific Thetaprobe instrument with Al Kα X-ray source. The operating pressure is below 1.0 $\times 10^{-10}$ mbar. 200 eV pass energy and 50 ms dwell time is applied for all times. Step size is set to 1.0 eV for surveys, and 0.1 eV for high-resolution elemental scans. ISS experiments are conducted with the same instrument as well with He ion gun with 1keV, step size of 1.0 eV, and at 2.0 $\times 10^{-7}$ mbar.

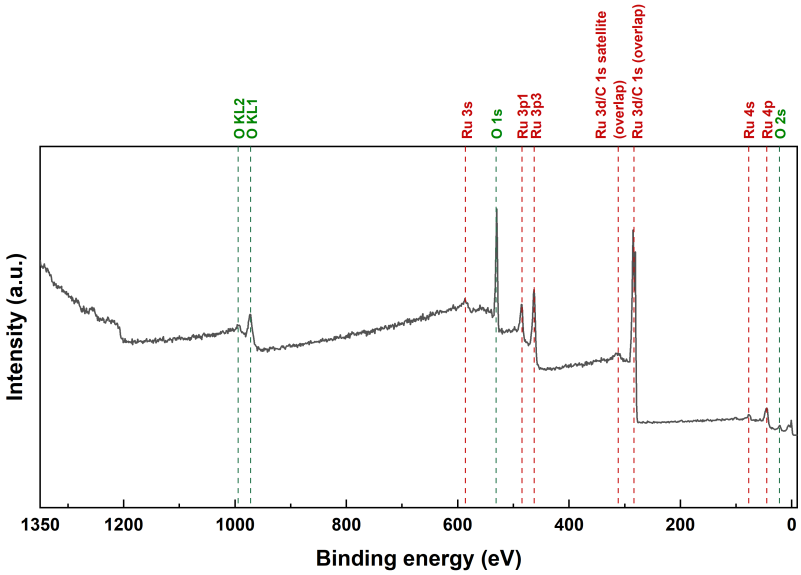

Figure A.10 XPS survey scan for RuO_2 on Ti substrate before the CER experiment. This spectra shows that the surface is covered with RuO_2 as the Ti peak is absent. There is no contamination elements present.

A.4.2 Real-time Equilibrium Potentials of the Catalysts

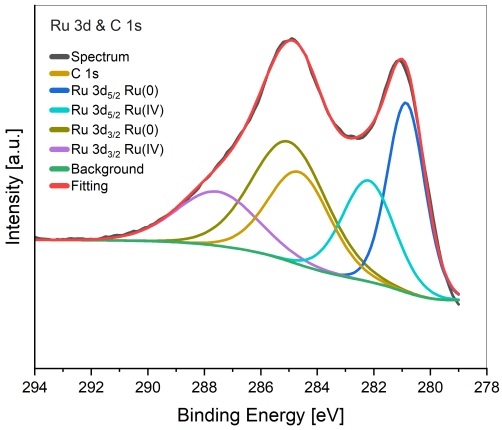

Figure A.11 XPS high resolution elemental scan of Ru 3d (overlapped with C 1s orbital scan) of the RuO_2 on Ti substrate before the CER experiment. This deconvoluted spectrum shows that Ru is at least partially oxidized within the detection depth.

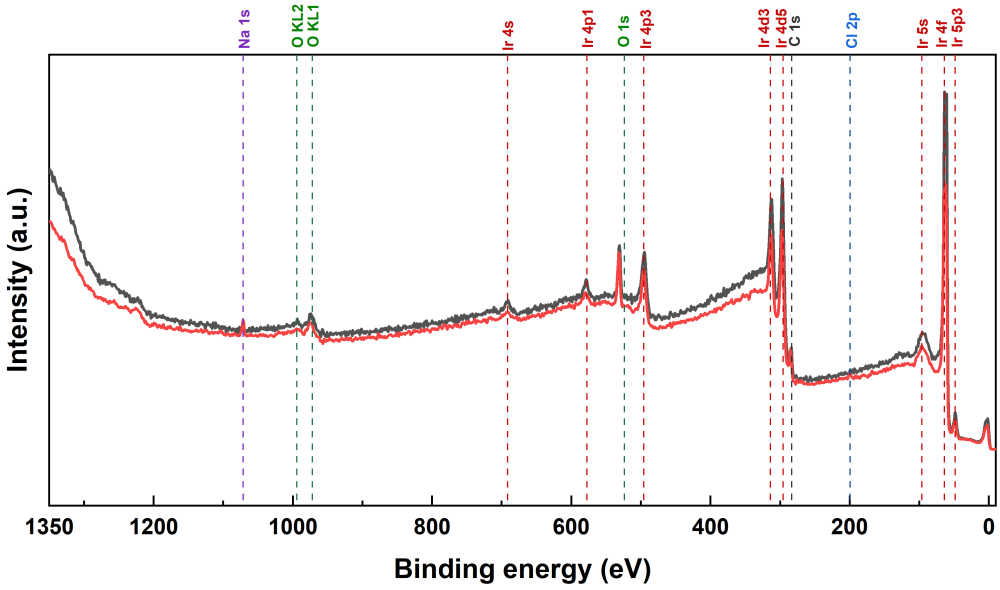

Figure A.12 XPS survey scan for IrO_2 on GC substrate before (black) and after (red) the CER experiment. These spectra show that there is no elemental contamination before the experiment. After the experiment Na and Cl peaks appear that comes from the electrolyte consist of NaCl.

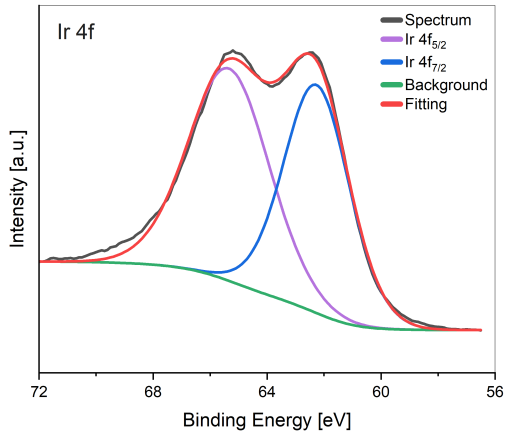

Figure A.13 XPS high resolution elemental scan of Ir 4f of IrO_2 on Ti substrate before the CER experiment showing that Ir exist on the surface. Determination of the oxidation of the oxidation state is cumbersome as the two spin orbit peaks are wide and overlapped substantially. Therefore, the obtained spectrum could be a convolution of different spectra belonging to different oxidation states of Ir contributing together.

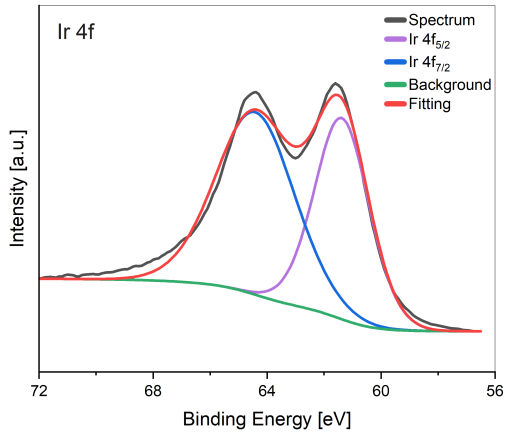

Figure A.14 XPS high resolution elemental scan of Ir 4f of IrO_2 on Ti substrate after the CER experiment showing that Ir exist on the surface. Determination of the oxidation of the oxidation state is cumbersome as the two spin orbit peaks are wide and overlapped substantially. Therefore, the obtained spectrum could be a convolution of different spectra belonging to different oxidation states of Ir contributing together.

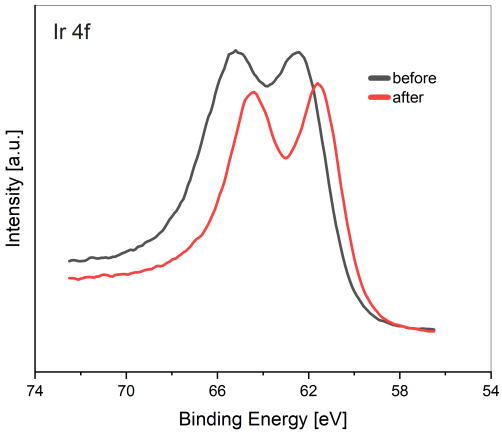

Figure A.15 XPS high resolution elemental scan of Ir 4f for the IrO_2 on GC before (black) and after (red) the experiment. These spectra shows a shift in the Ir 4f spectrum to a lower binding energy after the experiment indicating a decrease in the oxidation state of Ir.

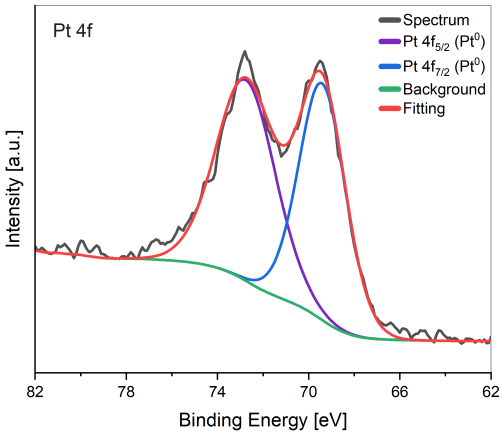

Figure A.16 XPS high resolution elemental scan of Pt 4f for Pt on Ti sample showing the presence of the metallic Pt.

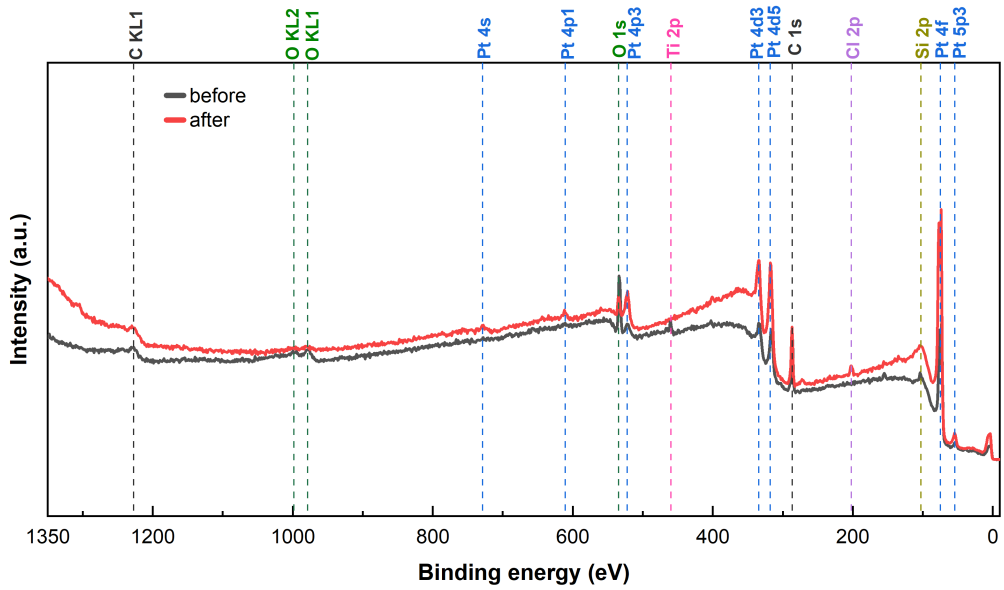

Figure A.17 XPS survey scan for TiO_2/Pt on GC substrate before (black) and after (red) the CER experiment. After the experiment Cl peak appear that comes from the electrolyte consist of NaCl. It is seen that Ti 2p peak after the experiment is absent as the top TiO_2 layer is disappeared during the CER experiment. Additionally, Si 2p peak is present for both before and after samples, which could come from the ALD chamber where Si substrates are used commonly.

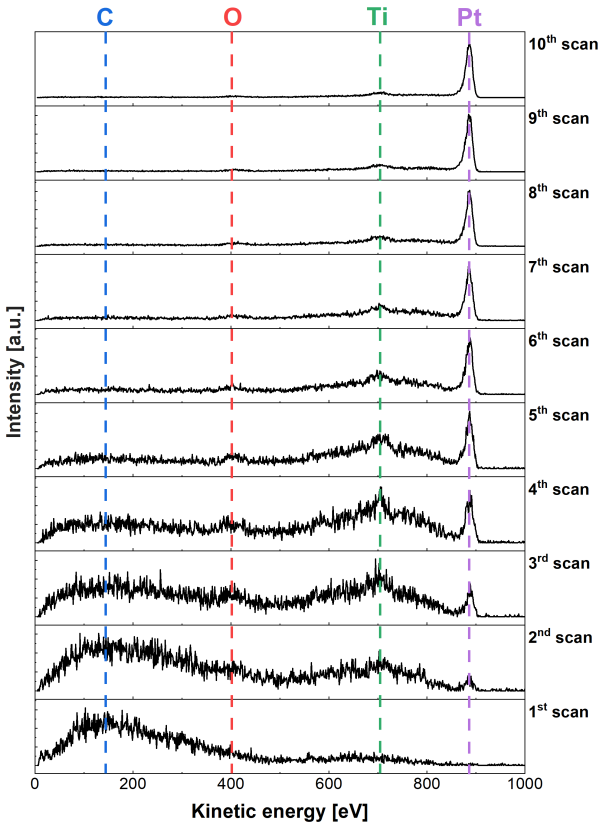

Figure A.18 ISS survey of TiO_2/Pt on GC substrate before the CER experiment. 10 scans are conducted consecutively. In the initial scan, a prominent carbon peak was observed, primarily caused by surface contamination during storage of the sample. However, as subsequent scans were conducted, this carbon peak gradually diminished, indicating the removal of contaminants from the topmost layers. In parallel, as the scan number increases, Ti and O peak intensity relative to Pt peak decreased indicating that there is thin TiO_2 layer on top of Pt layer.

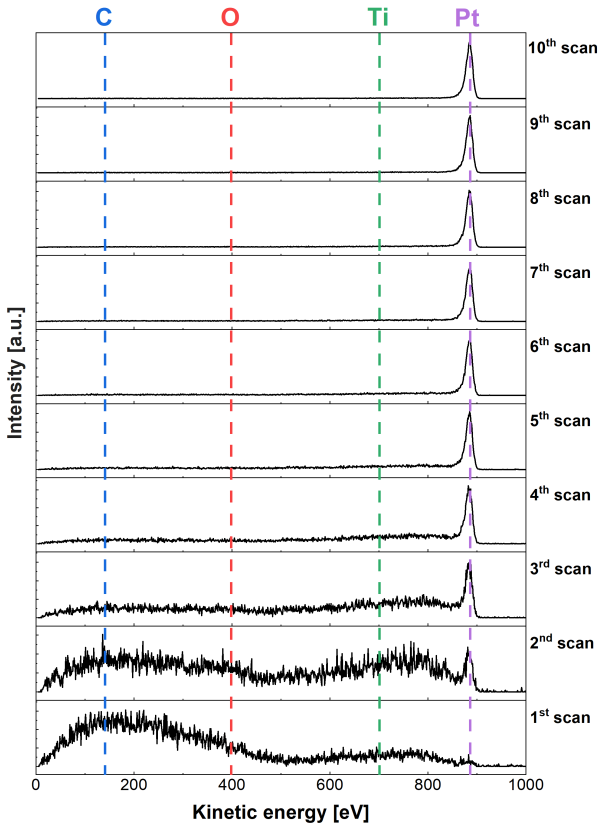

Figure A.19 ISS survey of TiO_2/Pt on GC substrate after the CER experiment. 10 scans are conducted consecutively. In the initial scan, a prominent carbon peak was observed, primarily caused by surface contamination during storage of the sample. However, as subsequent scans were conducted, this carbon peak gradually diminished, indicating the removal of contaminants from the topmost layers. In this sample, there was no Ti or O peak observed indicating the removal of thin TiO_2 from the surface. However, it is seen that Pt layer was stable throughout the experiment.

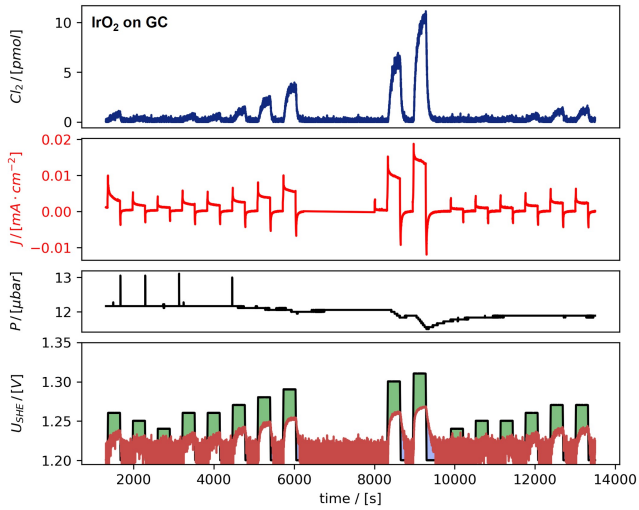

Figure A.20 Calculation of real-time E_{CER} on IrO_2 on GC. (a) Cl_2 flux, (b) recorded current density, (c) MS pressure measured by ion gauge and corrected for He, (d) Applied potential recorded by potentiostat (black), E_{CER} calculated in real-time (red), real-time overpotential highlighted with green in between the E_{ap} and E_{CER}.

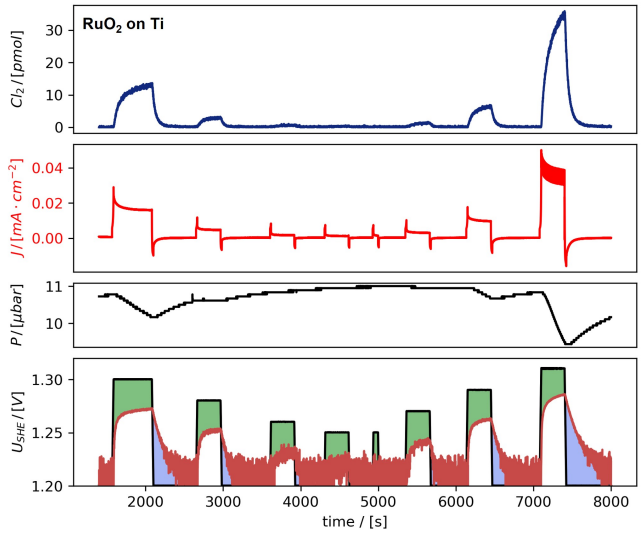

Figure A.21 Calculation of real-time E_{CER} on RuO_2 on Ti. (a) Cl_2 flux, (b) recorded current density, (c) MS pressure measured by ion gauge and corrected for He, (d) Applied potential recorded by potentiostat (black), E_{CER} calculated in real-time (red), real-time overpotential highlighted with green in between the E_{ap} and E_{CER}.

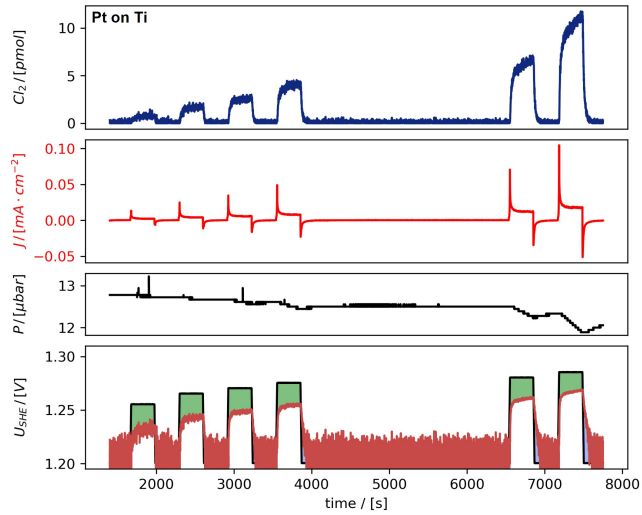

Figure A.22 Calculation of real-time E_{CER} on Pt on Ti. (a) Cl_2 flux, (b) recorded current density, (c) MS pressure measured by ion gauge and corrected for He, (d) Applied potential recorded by potentiostat (black), E_{CER} calculated in real-time (red), real-time overpotential highlighted with green in between the E_{ap} and E_{CER}.

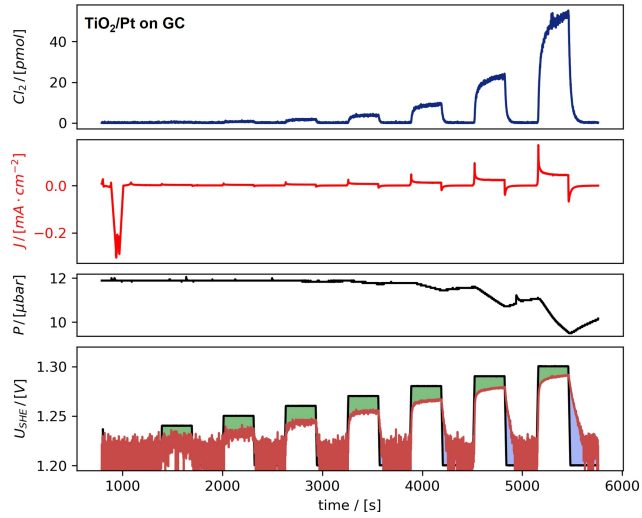

Figure A.23 Calculation of real-time E_{CER} on TiO_2/Pt on GC. (a) Cl_2 flux, (b) recorded current density, (c) MS pressure measured by ion gauge and corrected for He, (d) Applied potential recorded by potentiostat (black), E_{CER} calculated in real-time (red), real-time overpotential highlighted with green in between the E_{ap} and E_{CER}.

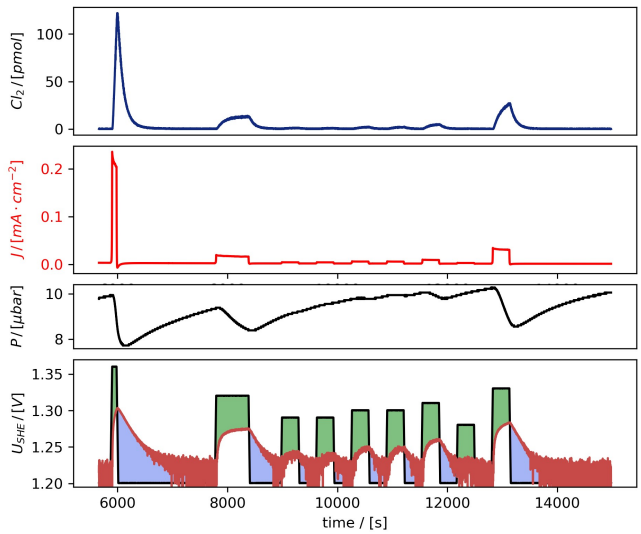

Figure A.24 Calculation of real-time E_{CER} on Ti stub. (a) Cl_2 flux, (b) recorded current density, (c) MS pressure measured by ion gauge and corrected for He, (d) Applied potential recorded by potentiostat (black), E_{CER} calculated in real-time (red), real-time overpotential highlighted with green in between the E_{ap} and E_{CER}.